UAB
Universitat Autònoma de Barcelona

UAB

Universitat Autònoma
de Barcelona

Soft Plasmomechanical Metamaterials for Sensing and Actuation

Pau Güell Grau

Directors:

Dra. Mar Álvarez

Dr. Borja Sepúlveda

Tutor:

Dra. Eva Pellicer

Universitat Autònoma de Barcelona

Departament de Física

Programa de Doctorat en Ciència de Materials

Bellaterra (Barcelona), novembre 2020

The present work entitled "Soft plasmomechanical metamaterials for sensing and actuation", presented by Pau Güell i Grau to obtain the degree of Doctor in Materials Science by Universitat Autònoma de Barcelona, was performed at the Biomedical Applications Group at the Instituto de Microelectrónica de Barcelona (IMB-CNM) and the Magnetic Nanostructures Group at the Institut Català de Nanociència i Nanotecnologia (ICN2), under the supervision of Dra. Mar Álvarez and Dr. Borja Sepúlveda.

The present thesis was also performed under the doctoral program studies "Doctorat en Ciència de Materials" at the Physics Department, Science Faculty, Universitat Autònoma de Barcelona, under the tutorship of Dra. Eva Pellicer.

Pau Güell i Grau
(Author)

Dra. Mar Alvarez
(Director)

Dr. Borja Sepúlveda
(Director)

Dra. Eva Pellicer
(Tutor)

PREFACE

I. Acknowledgments

Primer de tot vull agrair a els meus directors de tesi, Mar i Borja, per tota la feina feta durant aquests anys, per estar sempre disponibles a resoldre'm dubtes, ajudar-me amb els experiments, discussions científiques, etc. i sobretot pel bon tracte que sempre m'heu donat. Heu sabut complementar-vos a la perfecció per guiar-me durant aquests anys. També vull agrair als caps de grup, Rosa i Josep, per haver fet possible que hagi pogut treballar sota el paraigües del GAB i del MNG, respectivament.

Del Grup d'Aplicacions Biomèdiques guardaré un especial record de tots amb els qui he pogut compartir part d'aquest temps: de l'Edu: *nano* original com jo, amic, company de pis, de despatx i més...; del Jose i el seu peculiar humor, de l'Ana i el seu caràcter, del Miguel Zea i el seu carisma, del meu company de línia Fernando... i del Xavi, Anton, Eli, Gemma, Javi, Daniel, Ferran, Miguel Aller, Javier del Campo... en resum, de tots els *GABianos*.

Del *Magnetic Nanostructures Group* tres quarts del mateix, amb especials mencions pel Javi Muro, amb qui hem passat molts bons i mals moments al despatx, però sempre amb molt d'optimisme i humor absurd. I pel Li, sempre amb una bona paraula i obert a ajudar-te amb el que sigui. I a la resta de companys amb qui he tingut el plaer de coincidir: Yue, Guba, Nour, Filippos, Alex, Elvira, Patxi i Mª José. I no sent del grup, però que ha estat també molt present, Jose Fran, gràcies pel bon rotllo i les converses entre coffee breaks que hem tingut.

També crec que és bon moment per recordar-me'n dels anys previs al doctorat, els companys *nanos* amb qui he compartit els 4 anys de carrera i que alguns s'han convertit o es convertiran també en doctors. Especialment per l'Arnau i l'Àlex, els qui he vist defensar les seves tesis i ara jo segueixo el mateix camí.

I deixo pel final (però no per això menys importants) els meus agraïments per a la gent fora de l'àmbit acadèmic. Primer de tot, gràcies als meus pares per sempre recolzar-me amb els meus estudis i per creure cegament en mi. També a la resta de família per estar sempre acompanyant-me. I al Pep, que espero que li agradi llegir-se aquesta tesi.

Finalment, no puc tancar els agraïments sense recordar-me'n de les persones amb qui he conviscut durant aquests últims 4 anys, les quals m'han vist passar-les de tots colors. En especial a la *Zipotilla* i a la *Bananita*, que m'han sofert de primeríssima mà, i amb poc temps s'han convertit en la meva segona família. També un record especial a la meva colla gironina, que finalment em podran dir "*Dr. Güell*" amb totes les de la llei; i als meus companys rugbiers, tant als Centaures com al BUC, que tot i que estic segur que molts encara no entenen a què em dedico, han sigut vitals per evadir-me en moments d'estrès.

Amb aquesta tesi es tanca una etapa i inevitablement en començarà una altra, la qual no sé on em portarà, però que afronto amb moltes ganes i il·lusió per endavant.

Pau Güell i Grau

II. Resum

Durant l'última dècada, els materials intel·ligents han emergit com a una tendència fascinant en la ciència de materials. El seu concepte principal consisteix en l'auto-resposta reversible a estimulació externa (com per exemple temperatura, llum o camps elèctrics) produint un canvi en les seves pròpies propietats fisicoquímiques (p. ex. forma, color o rigidesa), i es basen normalment en materials tous en combinació amb altres materials amb funcionalitats extra. En aquest àmbit, els materials optomecànics tous són especialment interessants per desenvolupar dispositius de sensat i actuació innovadors gràcies a la naturalesa inalàmbrica dels sistemes òptics, la selectivitat sintonitzable a diferents longituds d'ona i la possibilitat de ser combinada amb altres tipus d'estimulació (p. ex. camps elèctrics o magnètics). En particular, la inclusió de nanopartícules o nanoestructures plasmòniques en substrats polimèrics tous (p. ex. elastòmers) comporta possibilitats interessants, com les característiques òptiques fàcils de modificar dels materials plasmonics i la gran elasticitat i robustesa dels materials tous. Aquesta nova classe de materials és referida en aquesta tesi com a *metamaterials plasmomecànics tous*.

Tot i així, aquest particular camp d'estudi es relativament recent, pel qual encara hi ha moltes oportunitats i reptes que han de ser afrontats. Per aquest motiu, aquesta tesi està dedicada al desenvolupament de nous metamaterials plasmomecànics tous, portant a terme l'estudi detallat de les seves propietats òptiques i mecàniques (englobant les ressonàncies plasmòniques, fenòmens fotònics i les respostes a esforç mecànic) i el seu disseny per a l'ús en aplicacions pràctiques en l'àmbit del sensat i l'actuació. La litografia col·loïdal és utilitzada per fabricar nanoestructures plasmòniques (Fe, Au), en combinació amb materials elastomèrics com el poli(dimetilsiloxà) (PDMS), per aconseguir cada particular metamaterial plasmomecànic.

Específicament, les dificultats d'implementar absorbents de llum en ampla de banda eficients en substrats flexibles o elàstics són abordades amb el desenvolupament d'un nou metamaterial basat en una capa de ferro nanoestructurat sobre una capa fina elastomèrica. Aquest nou metamaterial combina les ressonàncies plasmòniques amortides del ferro nanoestructurat amb l'absorció infraroja del PDMS per aconseguir una absorció independent de l'angle i amb un ample de banda sense precedents (mitjana del 84% des de 300 a 18000 nm). Aquest excepcional comportament òptic, juntament amb un gran desajustament de les propietats mecàniques d'ambdós materials és explotat per a desenvolupar diversos dispositius foto-termo-mecànics inalàmbrics i innovadors. Específicament, un iris artificial autoregulat, biomimètic i sense alimentació s'ha desenvolupat, el qual modula la seva obertura interna en resposta a la intensitat de llum incident, i per tant auto-regulant la potència de llum transmesa. A més a més, una pinça controlada per llum i un interruptor elèctric activat via llum s'han desenvolupat per a demostrar la extensa aplicabilitat d'aquest metamaterial. La quasi-plana absorció en gran ample de banda permet l'actuació d'aquests dispositius mitjançant tant llum monocromàtica com policromàtica (làser, LED blanc o llum solar), i inclús la feble emissió infraroja d'emissors tèrmics. A més a més, la independència a l'angle d'incidència de la

llum permet la efectivitat d'aquests dispositius en qualsevol orientació respecte a la llum incident.

A través de l'explotació de les propietats magnètiques del ferro, el mateix metamaterial és utilitzat també per a desenvolupar un actuador inalàmbric i multi-funcional (responsiu tant òptica com magnèticament). Específicament, el control senzill de la força i direcció de l'actuació magnètica és combinada amb la actuació lumínica de gran ample de banda, permetent condicions d'operació remotes i versàtils per a aplicacions en robòtica tova. A més a més, s'ha aconseguit la incorporació de la funcionalitat d'auto-sensat a través d'incloure una estructura de reixa fotònica a la part posterior de l'actuador, la qual proveeix de coloració estructural a l'actuador. La resposta mecànica de l'actuador a qualsevol estímul extern (p. ex. òptic o magnètic) es mostra com a un canvi de coloració (resposta mecanocròmica) i és quantificada en temps real a través de l'anàlisi del valor Hue dels píxels de les imatges preses a través d'una càmera RGB convencional o d'un smartphone. L'actuació remota i multi-estímul del dispositiu, juntament amb les seves capacitats d'auto-sensat estableixen les bases per al desenvolupament de mecanismes en bucle per a sistemes inalàmbrics automatitzats, els quals són de gran interès per a operacions en robòtica tova en ambients inaccessibles o perillosos.

Finalment, s'ha demostrat el desenvolupament de la primera cavitat Fabry-Perot estirable i amplificada plasmònicament, juntament amb la seva aplicabilitat per a sensat òptic d'esforç. Aquest nou material consisteix en una matriu de "mitja-closques" d'or plasmonic auto-organitzats, les quals són auto-incrustades dins un substrat elastomèric arrugat. El seu innovador protocol de fabricació està basat en l'estrès generat durant el curat del polímer, el qual és catalitzat per la superfície d'or de les mitja-closques. Aquest estrès provoca l'auto-empassament de les partícules plasmòniques dins la matriu polimèrica en profunditats controlades i la generació espontània de les arrugues superficials. Aquesta morfologia tant peculiar dóna lloc a un comportament òptic poc convencional que pot ser afinat a través de les condicions de fabricació. El material presenta una resposta òptica intensa (en variació de longitud d'ona i increment d'intensitat) a l'esforç mecànic, amb sensibilitat similar a altres aproximacions basades en processos de fabricació més complexes. A més a més, presenta gran robustesa i deformabilitat, les quals permet la seva aplicació com a sensor inalàmbric de pressió/esforç en superfícies corbades.

En resum, aquesta tesi aborda diferents reptes en el desenvolupament de materials intel·ligents optomecànics tous per a diverses plataformes de sensat i actuació. Aprofitant el comportament òptic únic dels nanomaterials plasmonics i les propietats fisicoquímiques dels elastòmers, nous metamaterials plasmomecànics s'han desenvolupat, caracteritzat i aplicat per a fer un pas endavant en el desenvolupament i implementació de materials optomecànics intel·ligents en diferents camps, com per exemple dispositius òptics autoregulats, robòtica tova o sensors d'esforç mecànic.

III. Abstract

During the last decade, smart materials have emerged as an exciting trend in materials science. Its main concept consists on the reversible self-response to external stimulation (such as temperature, light or electric fields) by changing its own physicochemical properties (e.g. shape, colour or stiffness), and they are usually based in soft materials in combination with other materials with extra functionalities. Within this scope, soft optomechanical materials are especially appealing for developing innovative sensing and actuation devices due to the wireless nature of optics, the tunable selectivity to different wavelengths, and the possibility to be combined with other types of stimuli (such as electric or magnetic fields). In particular, the inclusion of plasmonic nanoparticles or nanostructures into soft polymer substrates (e.g. elastomers) entail interesting possibilities, such as the easily-tunable optical features of plasmonic materials and large elasticity and robustness of soft materials. This new class of materials are referred as *soft plasmomechanical metamaterials*.

However, this particular field of study is relatively recent; thereby many opportunities and challenges still need to be dealt with. To that end, this thesis is dedicated to the development of new soft plasmomechanical metamaterials, bringing together the detailed study of their optical and mechanical properties (encompassing plasmonic resonances, photonic phenomena and responses to mechanical strain), with the design for their use into practical applications within the scope of sensing and actuation. Colloidal lithography is used to fabricate assembled plasmonic nanostructures (e.g. Fe, Au), that are following combined with elastomeric materials such as poly(dimethylsiloxane) (PDMS), to achieve each particular plasmomechanical metamaterial.

Specifically, the difficulties of implementing efficient broadband light absorbers into flexible or stretchable substrates are tackled by the development of a novel metamaterial based on a nanostructured iron layer on a thin elastomer film. This new metamaterial combines the damped plasmonic resonances of the nanostructured iron with the infrared absorption of PDMS to achieve an unprecedented broadband and angle-independent light absorption in flexible materials (average 84% from 300 to 18000 nm). This exceptional optical behaviour, together with a large mismatch on the mechanical properties of both materials are exploited to develop diverse innovative untethered photo-thermo-mechanical devices. Specifically, a power-free, self-regulated biomimetic artificial iris is developed, which modulates its inner aperture in response to the incident light intensity, thereby self-regulating the transmitted light power. Also, a light-controlled mechanical gripper and a light-triggered electrical switch are developed to demonstrate the further applicability of this metamaterial. The nearly-flat ultrabroadband absorption enables the actuation of these devices by both monochromatic and polychromatic light sources (e.g., laser, white LED or sunlight), and even by weak infrared thermal emitters. In addition, the angle independency allows the device effectiveness at any orientation to the incident light.

By exploiting the magnetic properties of iron, the same metamaterial is then used to develop an untethered, multi-functional (single and dual optical/magnetically-responsive) actuator. Specifically, an easy control of the magnetic actuation strength and direction is combined with the broadband light actuation, enabling remote and versatile work operation conditions for soft-robotics applications. In addition, the incorporation of a self-sensing functionality is achieved by including a photonic grating structure at the actuator back-side, which provides structural coloration to the actuator. The mechanical response of the actuator to any external stimuli (e.g. optical or magnetic) is displayed as a coloration shift (mechanochromic response) and quantified in real-time by the analysis of the Hue value in the pixels of the images taken by a conventional RGB camera or a smartphone camera. The remote and multi-stimuli actuation of the device, together with its self-sensing capabilities set the foundations for the development of feedback mechanisms in untethered automated systems, which are of great interest for soft robotics operation in inaccessible or hazardous environments.

Finally, the development of the first stretchable plasmonic-enhanced Fabry-Perot cavity is demonstrated, together with its applicability for optical strain sensing. This new material consists on an array of self-assembled plasmonic gold semi-shells which are self-embedded into a wrinkled elastomer matrix. Its innovative fabrication protocol is based on the stress generation during the polymer crosslinking, which is catalysed by the gold surface of the semi-shells. This stress leads to the self-swallowing of the plasmonic particles inside the polymer matrix at controlled depths and the spontaneous generation of surface wrinkles. This peculiar morphology gives rise to unconventional optical behaviour that can be tuned by the manufacturing conditions. The material shows strong optical response (in both wavelength shift and reflectivity increase) to mechanical strain, with similar sensitivity to other sensing approaches based in more complex fabrication processes. Furthermore, it shows large robustness and deformability, that enables its application as wireless pressure/strain sensing into curved surfaces.

Overall, this thesis tackles different challenges in the development of soft smart optomechanical materials for diverse sensing and actuation platforms. Taking advantage of the unique optical behaviour of plasmonic nanomaterials and the physicochemical properties of elastomers, novel plasmomechanical metamaterials are here developed, characterized and applied to take a step forward in the development and implementation of optomechanical smart materials into different fields, such as self-regulated optical devices, soft robotics or strain sensors.

IV. Table of Contents

V. Motivation

Sensors and actuators are the basic constituting parts of embedded systems. In general terms, a sensor is a device responsible of monitoring external stimuli that affect a system by converting them into a readable signal. By contrast, an actuator receives an input stimulation and converts it into a physical change on the system. Thermometers, cameras or accelerometers are typical examples of sensors, while actuators are usually referred to devices that exert a mechanical force into the system, such as valves or electric motors.
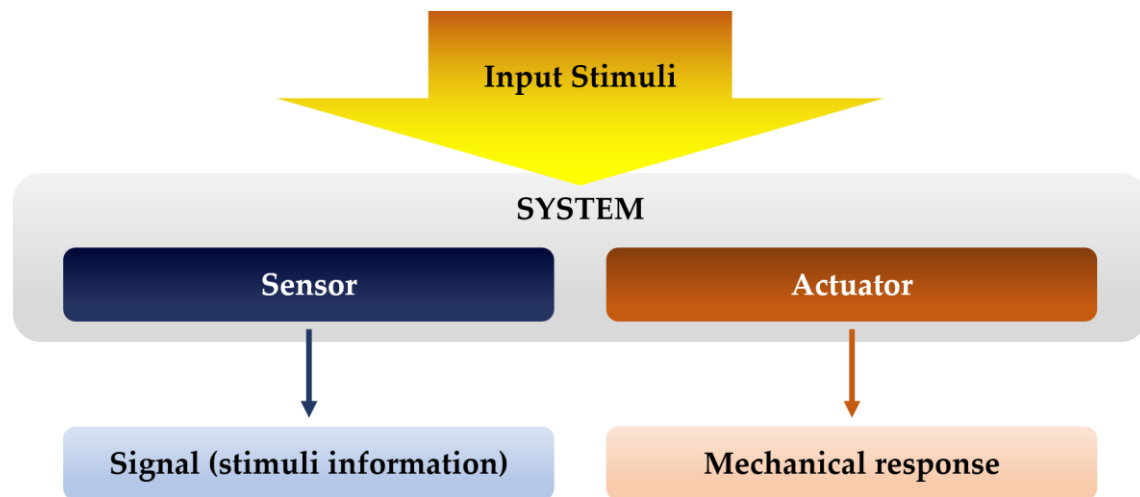
Figure V-1. Schematic diagram of sensing and actuation in an embedded system.

Currently, most of the embedded systems are based on electronics. Both the readable signal from sensors and the input stimulation of actuators are electric signals, which are managed by electronic machinery. These are commonly referred as *smart systems* (e.g. smartphones, computers...). The concept of smartness entails some attributes such as autonomous operation, self-sensing, memory and multi-functionality. However, the field of electronics is currently facing several important challenges. The exponential growth in computing performance predicted by Moore's law[1] is flattening out due to the enhanced heat losses and the unpredictable quantum behaviour of electrons in few-nanometres long circuit features, forcing scientists and engineers to rethink the way electronic machinery should be developed in the future[2]. Moreover, electronic circuits present some constraints, such as limited robustness to mechanical strains and harsh environmental conditions. Finally, but not less important, the amount of waste derived from electronics is enormous, reaching 50 million tons per year worldwide[3]. From them, only a 20% is formally recycled, having a dramatic impact on the environment, the human health and the global economy. Alternatively, a large interest has arisen in the last years in the so-called *smart materials*. In this case, the development of intelligent systems is based in the intrinsic physicochemical properties of rationally designed materials, instead of the currently used electronic and logical operations.

Smart materials (or stimuli-responsive materials) are usually defined as materials that have the ability to reversibly respond to one or more environmental stimuli (such as light,

temperature, strain, humidity, pH or electric and magnetic fields) by changing their own properties (e. g. shape, size, viscosity, stiffness, colour, among others) and thereby exerting a function[4]. They are in general soft materials, such as polymers or hydrogels, sometimes combined with other biological or hard materials or nanomaterials to achieve the desired functionality[5]. This approach seeks to avoid the problematics related to electronic circuitry, but conserving its smartness features (multi-functionality, self-monitoring, autonomous operation…), as well as increasing devices lifetimes, expanding the operating conditions, lowering component weight and reducing the overall complexity of the systems. To give a more comprehensive example of this replacement strategy, a conceptual schematic is shown in Figure V-2. In addition, the research and development on the physicochemical properties of materials generates the possibility to create new artificially-designed materials with extraordinary features, overcoming the naturally existing materials. These category of materials is known as *metamaterials*.
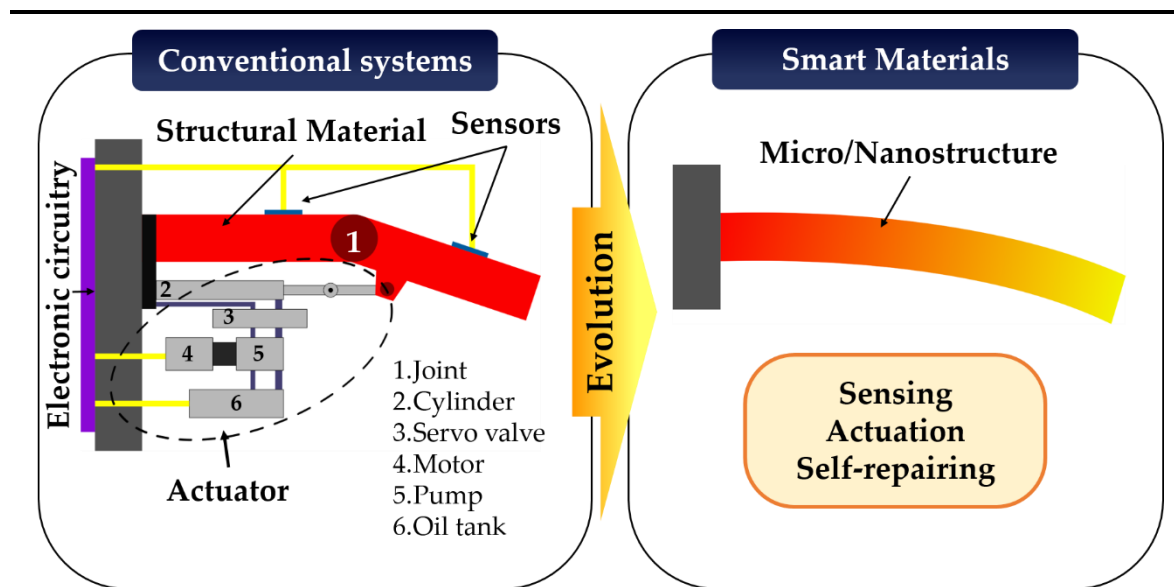
Figure V-2. Schematic representation of the transition from conventional systems to smart materials. Adapted figure[6].

Smart materials technology covers a broad range of categories, depending on the stimuli, the material response and the applications[4]. In this thesis, the attention has been focused on smart materials able to response to light by converting this stimulus into a mechanical response, and the opposite, i.e. tuning the material optical properties (such as transparency, reflectivity or colour) by mechanical stimulation. This category of smart materials is referred as optomechanical materials. Optomechanical materials present several features that make them very appealing for developing novel sensing and actuation devices. Actuation schemes based on optically-responsive materials (i.e. generation of mechanical forces by optical stimulation) have the capability to operate remotely, at long distances, with high spatial resolution and in a very controllable manner. Moreover, the optical properties of materials can be rationally tuned to give selectivity to a certain wavelength, or to trigger different responses as a function of the wavelength. For these purposes, plasmonic materials have demonstrated to be specially promising due to their exceptional

and easily-tunable optical features, such as narrow optical resonances, enhanced absorption of light, or high sensitivity to environmental variations. The rational design of plasmonic metamaterials and their combination with soft materials are denominated as *soft plasmomechanical metamaterials*. Also, since light stimulation it is not usually interfered by other stimuli, it can be combined to develop multi-stimuli responsive materials with multiple functionalities (e.g. opto-magnetic). On the other hand, the most relevant advantages of materials that change their optical properties to mechanical stimulation (i.e. optomechanical sensing schemes) rely on the untethered nature of the optical measurement: it can be performed wirelessly, even at naked eye (e.g. colorimetric detection), and sometimes it does not even require external powering.

VI. Aim & Objectives

The smart materials technology in general, and optomechanical materials in particular, is a very young field in full growth of development, full of challenges to be solved and promising future applications. The aim of this thesis is establishing the development of novel soft optomechanical metamaterials for smart sensing and actuation of devices, based on the combination of plasmonic metamaterials, soft polymers, and photonic nanostructures. This approach brings together the last advances in soft actuation, plasmonic resonances and photonic phenomena to achieve unconventional optical behaviour in metamaterials. Special interest has been also put in the application of these developments into practical and real uses. In particular, the development of three different materials/devices have been tackled in this thesis:

1. An ultrabroadband and angle-independent light absorber based on the unexplored optical behaviour of iron nanostructures and its application for soft optomechanical devices, such as a self-regulating artificial iris or light-controlled mechanical gripper and electrical switch.

2. An untethered soft actuator system based on a versatile opto-magnetic actuation control of the device, together with the incorporation of a self-sensing mechanochromic mechanism and its straightforward real-time analysis.

3. A new class of stretchable, plasmonic-assisted, Fabry-Perot cavity with enhanced optomechanical response for optical strain sensing applications using stretchable matrixes.

VII. Dissertation outline

This thesis is divided into six chapters which are summarized below:

- The <u>first chapter</u> presents an overview of smart materials and its applications, together with a detailed literature review of current research in soft optomechanical materials for different sensing and actuation platforms. This includes not only plasmonic materials, but other optical strategies that are relevant to the context of this thesis.

- The <u>second chapter</u> provides the necessary theoretical background on optics and mechanics to comprehend in detail all the aspects of this thesis. It includes the physics of plasmonic materials and photonic gratings, the mechanical theory of micromechanical systems and the physicochemical properties of soft polymers.

- The <u>third chapter</u> presents the exploitation of the unexplored optical behaviour of damped plasmonic materials to develop a novel soft metamaterial based on a nanostructured iron film mechanically coupled to a thin PDMS. This combination of materials exhibits ultrabroadband and angle-independent optical absorption which is then used to develop different soft optomechanical devices, such as a self-regulated artificial iris, a light-controlled mechanical gripper and a light-triggered electrical switch.

- In the <u>fourth chapter</u>, the nanostructured-Fe/PDMS actuator is modified to achieve dual opto-magnetic responsiveness together with wireless self-detection of the actuation strength. On the one hand, the magneto-mechanical properties of the material are explored and combined with optical actuation. In parallel, a periodic microstructure is defined at the actuator backside to provide mechanochromic behaviour to the structure. The optically/magnetically-induced mechanical displacements are 2D-mapped and quantified in real time by analysing the pixel coloration obtained by a conventional RGB or smartphone camera.

- In the <u>fifth chapter,</u> the first stretchable, plasmonic-enhanced Fabry-Perot cavity is developed and applied to optical strain sensing. The material, based on a gold semi-shell array that is self-embedded into a surface-wrinkled PDMS matrix, presents an unconventional optical behaviour from the coupling of plasmonic resonances and Fabry-Perot interferences together with surface light scattering. These phenomena can be controlled through the parameters of an innovative fabrication protocol based on the internal stress generated during the polymer crosslinking catalysed by the Au surface of the nanoparticles.

- Finally, the <u>sixth chapter</u> gives a summary of the conclusions obtained from this PhD dissertation. The future perspectives of the presented projects are discussed.

- In the final appendixes, extra documentation regarding this thesis is given: in appendix A, a detailed description of the experimental techniques is provided in

order to give specific methodologic details of the experimental work that has been carried out in this thesis. In Appendix B, the list of physicochemical properties of PDMS is detailed. Finally, in Appendix C, the list of publications, patents and industrial contracts arising from this thesis is presented.

VIII. References

1.   Moore, G. E. Cramming more components onto integrated circuits, *Electronics* **38**, (1965).

2.   Waldrop, M. M. The chips are down for Moore's law. *Nature News* **530**, 144 (2016).

3.   Platform for Accelerating the Circular Economy (United Nations). A New Circular Vision for Electronics: Time for a Global Reboot. *World Economic Forum* (2019).

4.   Li, Q. Intelligent stimuli-responsive materials: from well-defined nanostructures to applications. *John Wiley & Sons* (2013).

5.   Wei, M., Gao, Y., Li, X. & Serpe, M. J. Stimuli-responsive polymers and their applications. *Polym. Chem.* **8**, 127–143 (2016).

6.   Asanuma, H. Intelligent composite materials having capabilities of sensing, health monitoring, actuation, self-repair and multifunctionality. *Intelligent Materials* 478–490 (2007).

1. Introduction: Smart Sensing and Actuation Platforms Based on Soft Optomechanical Metamaterials

This thesis is focused on the study, development and application of soft plasmomechanical metamaterials. Therefore, this first chapter presents the necessary background on the topic in order to understand its framework. Firstly, the broad field of smart materials is introduced, including its different categories and applications. After that, an exhaustive literature review of soft optomechanical materials is presented, giving special emphasis to the applications in sensing and actuation. The information presented in this chapter will allow the reader to put this thesis' work in context and fully understand its achievements within the field of soft optomechanics.

1.1. INTRODUCTION TO SMART MATERIALS

1.1.1. Definition and context of smart materials

Even though the research and development of smart materials is relatively recent, stimuli-responsive materials are already present in nature in diverse forms. Among many examples, pine cones have the ability to open or close their scales in response to the humidity conditions due a differential hygroscopic expansion of their components[1], the Venus flytrap plant can capture insects by rapidly closing their leaves by changing the hydrostatic pressure of the leaf sub-layers after perceiving consecutive touches[2], wood presents strain memory effects[3], and chameleons can alter their skin coloration in response to environmental stimuli by changing the periodical micro-/nanostructures in their skin[4].

Regarding the artificial design and development of smart materials, one of the first examples in history can be found at Giza's pyramids, specifically at the lime mortar used for construction. It is well documented that lime mortar exhibits self-repairing properties due to the dissolution of calcium bearing compounds by water (coming from the rain) and its transport to areas with voids and cracks to begin a re-crystallization (therefore, self-healing) process[5]. However, it is not very clear if the ancient Egyptians knew about this process. Actually, until recently, humanity only considered materials as structural components[6]. It was not until the 19th century, when, together with the first descriptions of light and electromagnetism and, ultimately, the birth of modern physics, scientists started to explore new properties and functionalities of materials. A very illustrative example is the discovery of piezoelectricity by Pierre and Jacques Curie in 1880[7]: the demonstration that an electrical potential can be generated by applying mechanical strain in a material lead to the development of many devices that are used nowadays, such as accelerometers, microphones or radars. This change of perspective about the materials' use from only structural to functional entailed a paradigm shift and the beginning of the modern era of materials science. During the last 50 years, the development of new fabrication and characterization equipment (e.g. optical lithography, electron microscopy, confocal microscopy…), together with the rapid development of nanotechnology, provided very useful tools to explore the physics of materials at the molecular and macromolecular level. Understanding the behaviour of the building blocks from which the materials are formed has been the key to understand, predict and ultimately modify the physicochemical properties of materials to our benefit.

Nowadays, we have the ability to design and create many structural and (multi)-functional materials based on the acquired knowledge of the physical phenomena, computational tools and the most advanced manufacturing and characterization techniques. In order to go further and develop intelligently designed materials, we need to seek the inclusion of both structure and function, together with efficient operation and feedback from the material itself (Figure 1-1). Ironically, to develop well-designed, efficient smart materials, the scientific community need to look back and get inspired by the natural systems. As mentioned previously, nature has designed, through thousands of years of evolution,

systems that are able to sense and adapt to different environmental conditions, combining both structure and multiple functionality, ensuring the efficiency of the performed tasks. Therefore, current trends in research of novel smart materials combine deep understanding of the physical processes, inspiration from natural systems and advanced technology for design and manufacturing, always pointing towards their implementation into functional devices.
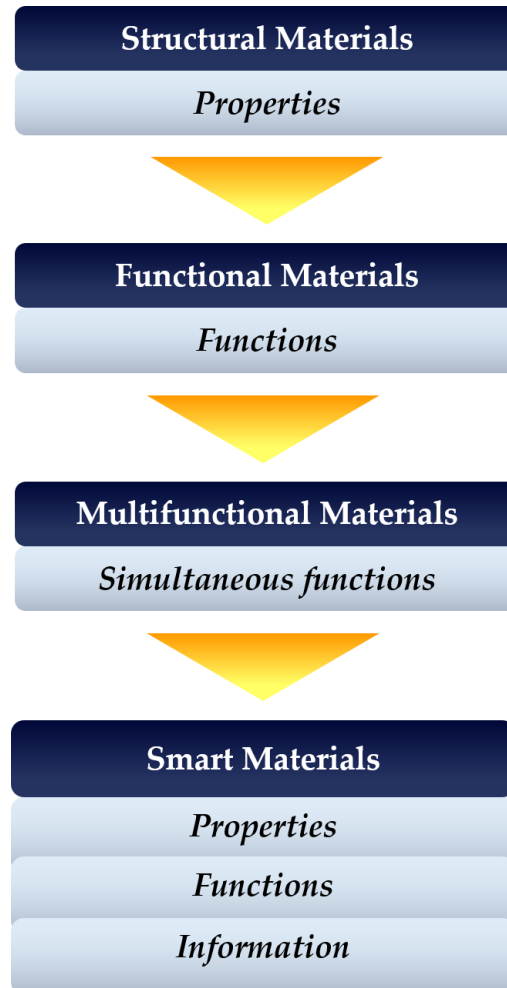
Figure 1-1. Flow chart of the evolution of materials science. Adapted figure[6].

1.1.2. Categories of smart materials

Smart materials can be classified in different manners. Here, the numerous categories of smart materials are organized as a function of the stimulus to which respond and the type of response. In Figure 1-2 a schematic diagram of the main smart material categories is shown. It is worth noting that most of the responses can also act as a stimulus, hence multiple stimuli-response events can occur consecutively. The stimulus and response are usually the main aspects to take into account to decide which type of smart material is the most suitable to solve a certain problem. In many occasions, each application has specific constraints (for example, self-adjustable windows require a change on the light transmission as a final response, while a biomimetic robot needs a controlled mechanical

movement). However, every stimulus and response has its intrinsic advantages and limitations. In brief, chemical stimuli present an enhanced selectivity (absorption of specific solvents, enzyme-substrate recognition…), but chemical processes are generally slow and fluid media are required for the reactions to take place. On the contrary, heat transport is especially efficient in solid environments, but it is usually constrained to the thermal conductivity of the material components, which might be not adequate for high frequency processes. In this regard, electrical stimulation is probably the fastest and most controllable stimulus of the list. However, it is limited by the use of electrical connections, which can be an obstacle for certain applications. The best alternatives to achieve wireless stimulation with a fast response is the use of light or magnetic fields. On the one hand, optical stimuli can be delivered in a local and controllable manner, even having selectivity based on the working wavelength. However, it is restricted to be used in non-opaque environments. On the other hand, magnetic stimulation can be operated in almost any environment and at relatively long distances with high precision. Nonetheless, it usually requires the use of rare metallic elements or very strong magnetic fields that constrain its applicability range. Finally, mechanical strain can also act as an input stimulus, being especially suitable to operate in mobile devices (e.g. robotics). However, the materials need some degree of elasticity and compliancy.
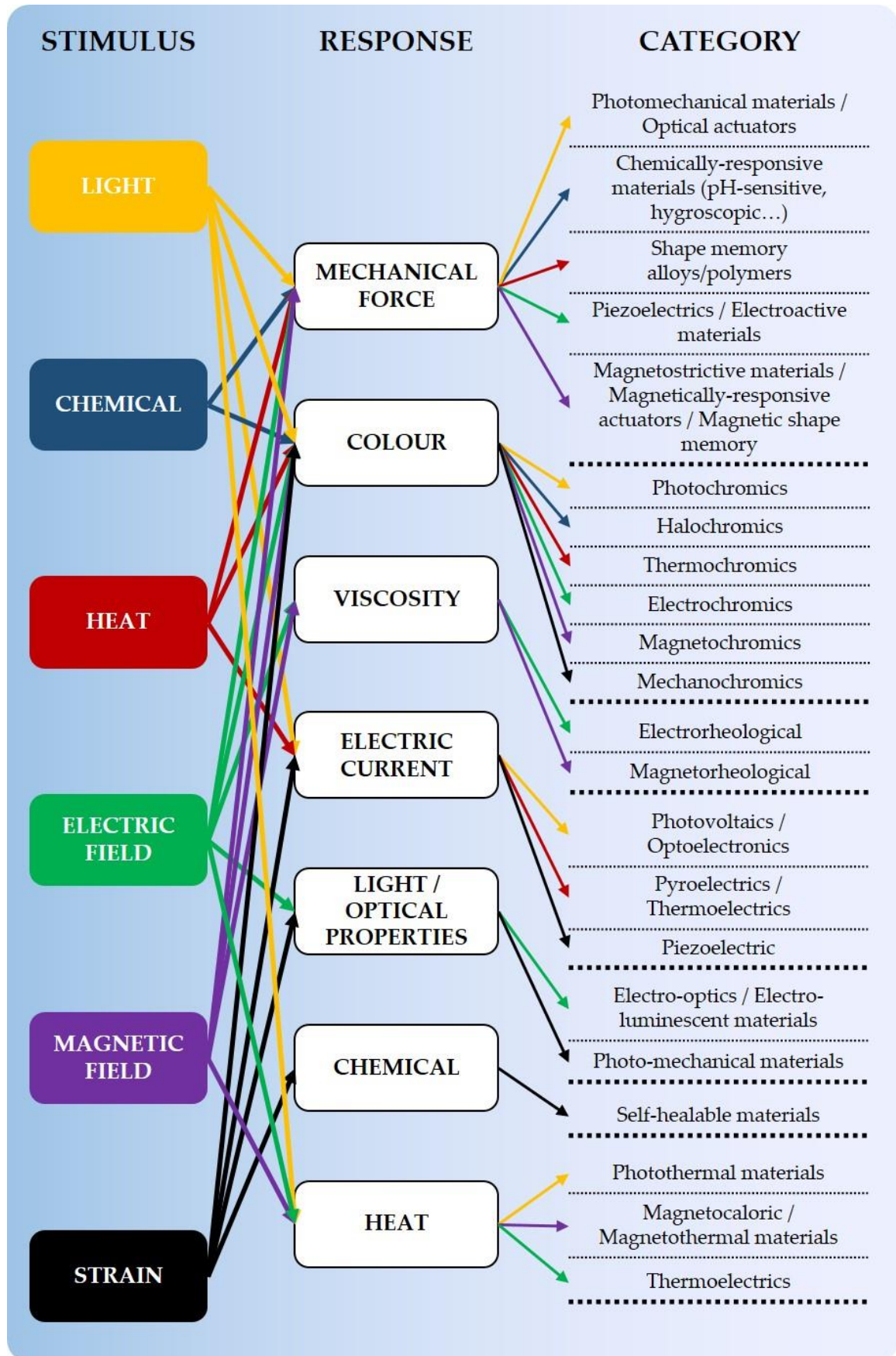
Figure 1-2. a) Classification diagram of smart materials by type of stimulus and response.

1.1.3. Overview of smart materials applications

Due to the vast number of possible combinations of stimuli and response, the range of applications that can be developed is very broad. To give a comprehensive overview of the possible uses of smart materials, a selection of some relevant applications are detailed here.

Structural materials with additional functionalities attract the attention of many different areas, such as the automotive industry and civil engineering. For instance, shape-memory materials (alloys or polymers) allow the passive adaptation of the structure to environmental stimuli (such as humidity or temperature) and the recovery of their fundamental shape thereupon an external stimulation[8]. Also, smart adhesives are appealing due to the controllable adhesion mediated by external stimuli, such as heat or light[9] and self-healing materials even have the ability to self-repair the damaged parts of the structure[10]. In this line, recent research on materials for clothing is pointing towards the development of materials with passive functionalities, such as self-cleaning, self-healing and thermoregulation[11]. Another example is the development of new generation of windows: current trends are focusing on the autonomous change of their colour or transparency upon an external stimulus, which have a tremendous potential for energy saving due to the thermal and light regulation inside buildings and vehicles. To accomplish this purpose, thermochromic, electrochromic or photochromic materials are needed[12]. Regarding energy generation, by definition, it requires the use of stimuli-responsive materials, including photovoltaics, pyroelectricity or piezoelectricity, among others. For example, piezoelectric materials can be implemented in the roads of some big cities in order to obtain energy from the pressure that cars apply when go over them to be then re-used to give power to other devices, such as traffic lights[13]. Another interesting example is the development of pyroelectrics for the exploitation and recycling of waste heat into useable energy[14]. Stimuli-responsive materials are also of great relevance in the biomedical field. Current therapies are pointing towards the use of controlled drug delivery systems, which are based on encapsulated drugs that are released in the presence of an external stimulus, such as a change in the chemical environment, light or magnetic stimulation[15]. On the other hand, prosthetics needs the use of self-adaptable and controllable materials to mimic the functions and performance of natural organs. In this line, electrically, optically and magnetically-responsive materials are being of great interest for developing artificial muscles[16]. Following this trend, they are also being applied in robotics, in which the conventional hard materials are replaced by stimuli-responsive soft polymers, which is known as soft robotics[17]. These systems are being extensively investigated in order to achieve similar task performance with higher durability, external control and lower costs. Furthermore, the next step is to include self-detection of the movement and the strain that the structure experiences, giving a real-time readout of the actuation. To do so, it is needed to develop and include stretchable strain sensors into the devices. In a similar way, they can be of interest for structural health monitoring, to detect and prevent damages in large structures[18] or for movement recording and analysis of gestures and postures, which can give important information for physiotherapists or athletes[19].

1.2. SOFT OPTOMECHANICAL METAMATERIALS FOR SMART SENSING AND ACTUATION

As mentioned previously, the unique optical properties of plasmonic and photonic structures in combination with the exceptional mechanical features of soft polymers (and specifically, elastomers) are being used to develop different kinds of smart materials with optomechanical response. This combination of materials is especially interesting from the optical and mechanical point of view: elastomers are usually transparent to visible light and near-infrared, where most of plasmonic nanostructures present their surface plasmon resonances. Therefore, the substrate does not interfere with the optical response of the plasmonic materials in the wavelength range of interest. On the other hand, plasmonic materials can be incorporated to elastomeric substrates with high compliancy and handle high substrate deformations. Hereunder, an extensive literature review of soft plasmomechanical metamaterials for sensing and actuation platforms is presented.

1.2.1. Soft optomechanical metamaterials for sensing

Devices that can detect mechanical deformations giving a readable output are very interesting in many ways. Firstly, strain or displacement sensors are needed for structures where is important to determine the mechanical stress that they experience, such as buildings, vehicles, packages or even wearable devices. On the other hand, mechanical sensors are themselves a transductor to detect other kind of stimuli: an external stimulus (e.g. chemical, biochemical, optical…) produces a mechanical deformation of the material, which gives a readable signal of the stress that it is experiencing. This category, for example, include some biosensors and MEMS that have been widely developed in the last decade. There is an increasing interest to develop soft, stretchable materials to detect mechanical deformations since they can handle large strains, recover after many cycles and are usually inexpensive. However, soft mechanical sensors require of a compliant transductor. Several options exist, but electrical and optical are the most appealing. Regarding the optical transduction, it presents several advantages that have been previously outlined, such as its wireless nature, easy reading and possibility to 2D mapping of strain, even at micrometre size resolution.

In general, there are two different ways for detecting the mechanical deformation (as a direct stimulus or as a response to other stimuli) of a smart material by optical means: the first is a change on the light spectrum or colour (i.e. mechanochromic detection) and the other one is based on change of the transmitted or reflected light intensity. In general, mechanochromic detection relies on the interaction of light with materials at the sub-wavelength or wavelength scale (i.e. nanophotonics). Plasmonic materials and metamaterials are typical sub-wavelength regime materials, in which the electromagnetic field of the incident light interacts with the electronic structure of materials. On the other hand, photonic structures such as gratings and photonic crystals are wavelength-scale

structures, where diffraction and interference effects are predominant. In contrast, optical detection based on light intensity variations are more commonly based on bigger dimension structures, such as surface textures, waveguides and microlenses[20].

1.2.1.1. Strain sensing based on plasmonic materials

Near-field interaction

The most widely used strategy for the detection of mechanical strain and deformations using plasmonic materials consists on taking advantage of the strong interaction between neighbouring plasmonic nanoparticles or nanostructures (i.e. near field interaction), which is extremely sensitive to the interparticle distance. For example, U. Cataldi and co-workers extensively studied a gold nanoparticle-coated PDMS plasmomechanical sensor[21–24]. Their fabrication method based on chemical growing allows the precise control of the inter-particle gap with the number of growing cycles, hence they described that the effect is relevant only if the inter-particle separation is smaller than half times the nanoparticles' diameter. This effect becomes more significant as the particles go closer, which is correlated to the rapidly decaying electric field strength from the centre to outside a plasmonic nanoparticle. Taking advantage of this, they also studied how this material can be used to mechanically tune the photogenerated heat of the gold nanoparticles upon laser excitation[25]. Also, a theoretical investigation of the plasmonic behaviour for different gold nanoparticle arrays experiencing mechanical strain was recently published by the same group[26]. Taking into account that for most elastomeric substrates a tensile strain in the X direction leads a compression in Y and Z directions, the incident light polarization has a significant importance on the sensitivity for a particular stretching direction. In this line, Millyard *et al.* designed a strain sensor based on self-assembled gold nanoparticles on a PDMS film[27]. They studied the resonance shifting as a function of the strain for polarized (parallel and transverse to the stretch) and unpolarised light. Besides, they also studied the compression in the perpendicular direction of the PDMS film, which leads to an elongation in all directions in the plane of the gold nanoparticle array and therefore, to an enhanced sensitivity and polarization independency. Using closed-packed structures of gold nanoparticles (NPs), it may occur that cracks on the NP array structure are formed due to the strain, which leads to a decrease on the number of particles in the cracking area. Then, the deformation can be measured in terms of intensity shrink instead of wavelength shift[28]. Another option is to embed the nanoparticles into the polymer film[29,30]. The nanoparticle chains inside the polymer start to disassemble when it is stretched, so the coupling peak's wavelength shifts. Taking advantage of this, a pressure sensor has been developed, in which the change of colour of the material is analysed using a conventional smartphone camera[31]. Similarly, Burel *et al.* proposed the encapsulation of gold nanoparticles into silica microcapsules that could be incorporated into polymer films to give a mechanochromic response[32] and Choe *et al.* designed a colorimetric patch based on AuNP-decorated thermoresponsive hydrogel[33].

Gold nanoparticles have been widely used in plasmomechanical materials since its optical response is very well-known. However, other geometries and metals have been also used.

For example, nanodisks are also widely used in the field of plasmomechanical metamaterials for sensing. An extensive theoretical study of the polarization-dependent resonance on gold nanodisks heptamer units was first described by Cui *et al.*[34]. Similarly, the dependence of the optical resonance to the orientation of a pair of gold nanodisks, as well as the effect of compression and stretching was first described by Kan *et al.*[35]. Then, Mahmoud *et al.* reported the fabrication of silver nanodisks on PDMS, achieving a linear response for tensile strain but an exponential trend for compression[36]. Likewise, a square array of gold nanodisks on PDMS nanopillars was reported[37]. In this approximation they also study the inverse optical behaviour between polarized light parallel and perpendicular to the stretch axis. Another gold nanodisks square array was also studied by Gao *et al.*[38]. In their device, buckling of PDMS occurs for high stretches, which also enhances the red-shifting due to a change in the effective interaction between disks. Following this idea, gold nanodisks transferred to a buckled PDMS substrate were also studied by Feng *et al.*[39]. Additionally, it is worth mentioning that more sophisticated nanostructures, such as bowtie antennas[40,41] or nanorod arrays[41] are being developed and transferred to flexible and elastic substrates by using nanofabrication techniques such as electron beam lithography. Thanks to the excellent control on the inter-particle distance and nanostructure shape and dimensions, these metamaterials can achieve enhanced sensitivities and a very precise control on the plasmon resonances. Split-ring resonators are an interesting example of a precise control on the plasmonic resonances by rationally tuning the shape and dimensions of the optical metamaterial. The optical response for different geometries, dimensions and separations between elements were investigated by Pryce *et al.*[42,43]. Then, the resonance frequency was tuned as a function of the applied strain, which alters the separation between the plasmonic elements.
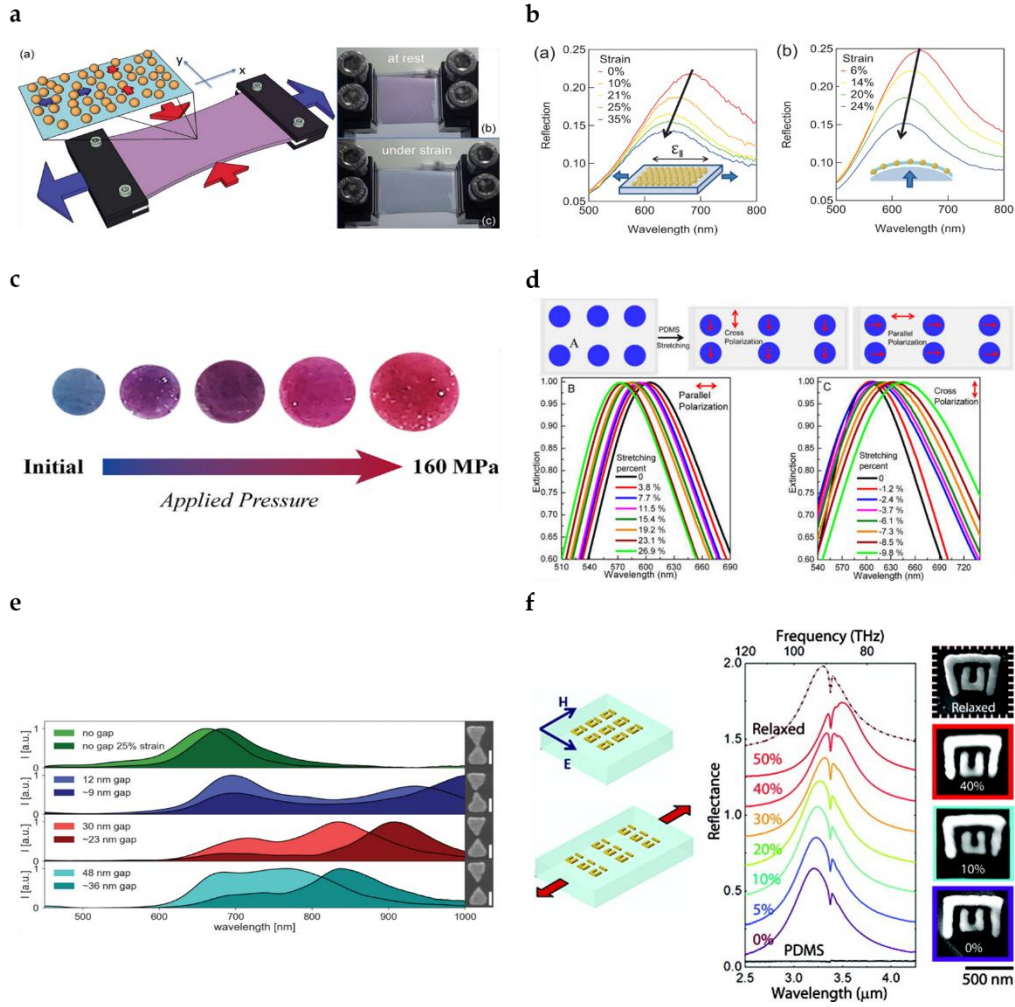
Figure 1-3. Strain sensors based on plasmonic near-field interaction. a) Gold nanoparticles chemically grown on a PDMS substrate[22]. b) Optomechanical response of gold nanoparticle array on PDMS to unidirectional and bidirectional strain[27]. c) Colorimetric pressure sensor based on gold nanoparticles embedded into polyacrylamide[31]. d) Polarization-dependent response of silver nanodisks on PDMS[36]. e) Optomechanical response of bow-tie antennas of different separations to 25% strain[40]. f) Strain-responsive split-ring resonators on PDMS[43].

Propagating surface plasmons

Besides the near field interaction that arises from the localized Mie resonances in the plasmonic nanoparticles, the use of periodic arrays of plasmonic nanostructures that can support propagating modes (SPPs) have been also studied and developed. For example, silver- and gold-capped, hexagonal close-packed polystyrene nanospheres array on PDMS were reported by Zhu X *et al.*[44,45]. Metal-capped nanospheres can support localized resonances, however, since they are almost in contact and in a periodic organization, delocalized, propagating modes are observed. These are not only strain-sensitive, but also angle sensitive. When the material is stretched, two effects are present: the increasing distance between the metallic caps and the distortion of the lattice type, which leads to a redshift of the plasmon resonance. Periodic arrays of nanowires have been also

investigated. For instance, "U-shaped", aluminium-coated polyurethane nanowires were fabricated by Lütolf *et al.*[46]. In this material, the electric field can be guided in the direction perpendicular to the nanowires. In short, an SPP mode is combined with a localized Fabry-Perot like mode, which experience a redshift and a steep decrease on the amplitude upon increasing strain. This is translated into a macroscopic colorimetric change that can be easily analysed. Following a similar trend, a strain-sensitive, strong coupling through plasmonic-photonic interactions of gold nanolines on flexible substrates have been also investigated[47]. Other periodic plasmonic structures can also be used as strain-sensitive plasmonic strain sensors. For instance, gold-coated nanovoids in PDMS were also studied as plasmonic periodic nanostructures that can support localized Mie plasmon modes and propagating Bragg plasmon modes[48]. Also, roll-to-roll fabrication of tunable plasmonic arrays of gold-coated asymmetric nanopyramids of PDMS was reported by Yoo *et al.*[49]. The stretching of the material leads to a change in the angle between the pyramid facet and the incident light. Due to the high angular sensitivity of SPPs on the pyramidal facets, this material achieves an outstanding sensitivity of 15.22 nm for a 1% strain, being to date the most sensitive plasmonic strain sensor reported to date.
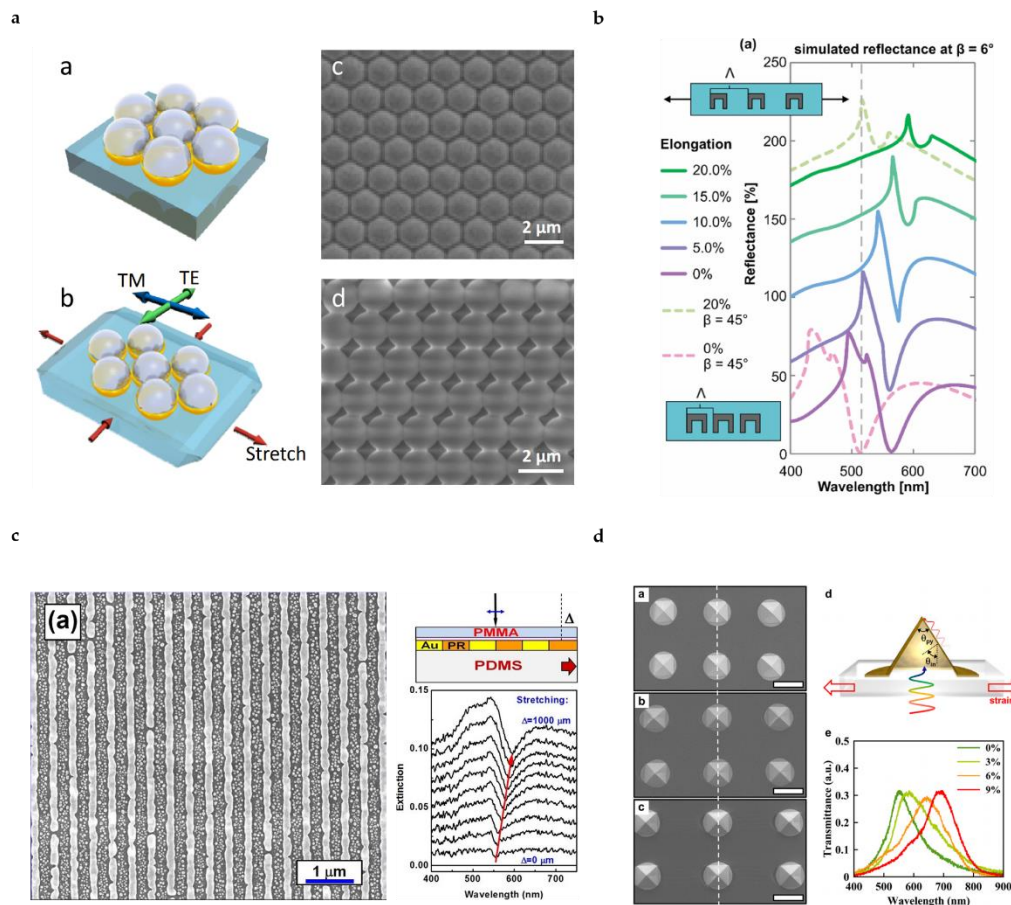
Figure 1-4. Strain sensors based on surface propagating plasmons. a) Array of gold-capped polystyrene nanospheres on PDMS[45]. b) Optomechanical response of U-shaped, aluminium-coated polyurethane nanowires[46]. c) Optomechanical response of gold nanolines on PDMS[47]. d) Array of gold-coated nanopyramids in PDMS and corresponding optomechanical response[49].

## 1.2.1.2. Mechanochromic sensing using soft photonic structures

Photonic crystals and diffraction gratings are widely used in many optic devices, such as monochromators and spectrometers. The light diffraction and interferences in the periodic micro/nanostructure causes a wavelength separation of the transmitted/reflected light in different angles, which is at the same time very sensitive to variations in the periodicity and refractive index. Therefore, these structures are of great interest for developing optical sensors to detect mechanical strain or even other kinds of stimuli. The periodicity of the photonic crystal can be in one, two or three dimensions and they are usually fabricated by the use of either the self-organization of colloidal particles or photolithography[50].

Most of three-dimensional photonic crystals (also referred as opals) are based on self-assembly of polystyrene or silica nanospheres[51], followed by the infiltration of a polymer matrix (such as PDMS) and a posterior etching of the spheres. Works from Weismann *et al.*[52] and Fudouzi *et al.*[53,54] firstly described the fabrication protocol and the strong colorimetric response of the opal structures to applied mechanical strain. This strategy was then followed by many other authors, studying in detail the diffraction phenomena in distorted crystal lattices[55], optimizing the fabrication protocol to achieve more robust and reversible actuation[56] and the use of different soft materials, such as hydrogels[57] or shape-memory polymers[58]. In addition, the mechanochromic response of opal structures has been also taken advantage of to develop other varied applications. For example, an elastomeric opal was used to develop a colorimetric fingerprinting and to tune the photoluminiscent emission of PbS quantum dots just by the application of pressure[59]. Also, hydrogel opals have been of great interest to develop thermoresponsive colorimetric sensors. The high thermal expansion of hydrogels causes the isotropic deformation of the crystal lattice, thereby producing large colour shifts[60]. Following a similar strategy, other types of sensors have been developed, such as biosensors and indicators[61] or detection of magnetic fields[62,63], among others[64]. On the other hand, two-dimensional arrays of particles have been also used to develop strain-sensing and mechanochromic devices. For example, colour writing in photonic "papers" was also proposed by Fudouzi *et al.*[65]. They demonstrated the fabrication of 2D photonic crystals based on polystyrene nanospheres, which interparticle distance (and therefore, its coloration) varies when swelling occurs due to the application of an organic solvent. Following this work, Yang *et al.* used 2D photonic crystals based on silica nanospheres on poly(ethylene glycol) methacrylate (PEGMA) to develop a colorimetric pressure sensor with high sensitivity and fast response[66]. Also, a colorimetric pressure sensor for optofluidic applications was developed[67], using self-assembled polystyrene nanospheres as a template to generate a bidimensional photonic crystal on the elastomer structure.

Even though the fabrication based on the self-assembly of colloidal particles is a non-expensive, versatile fabrication method, it is difficult to achieve very large areas with high homogeneity. Alternatively, nanoimprint lithography (NIL) offers an easy, low-cost methodology to produce large areas of periodic nanostructured surfaces[68,69,70]. In general terms, it is based on the fabrication of a master mould by optical lithography and physical etching, which can be replicated several times using soft, elastic polymers (such as

elastomers). In this sense, the use of photonic gratings for mechanochromic sensing have been reported for many authors. For example, colorimetric pressure sensors have been proposed[71,72], which are of great relevance in non-contact measurements such as in the intraocular pressure sensing[71]. Also, they have been tested as self-reporting mechanism of the actuation of soft-robotic structures[73,74]. Furthermore, some efforts have been made to develop improved alternatives to conventional NIL. For example, Zhang *et al*. proposed an improved methodology to achieve unidimensional photonic gratings with small patterns based on the stretchability of a PDMS substrate mould[75]. The generation of periodic surface corrugations on PDMS by an oxygen plasma treatment of initially stretched PDMS was also proposed[76] (this methodology will be more detailed in the following subsection). Going a little bit further, Xu *et al*. demonstrated the fabrication of microprism arrays and diffraction gratings of different geometries using shape memory polymers and its posterior optomechanical analysis to build shape-memorizing micro-optics[77].

Finally, it is worth mentioning other fabrication approaches that seek to develop biomimetic structures, which are inspired by the micro and nanostructures found in some living organisms. For example, *Morpho* butterfly wings are composed of a complex tridimensional microstructure that presents iridescence. Therefore, many authors explored the replication of these structures to build highly sensitive photonic gratings[78–80] and even combine them with plasmonic nanoparticles to achieve NIR-responsiveness[81]. On the other hand, the multilayer structure in tropical fish scales was replicated by using multilayers of hydrolysed polyacrylamide (PAAm) hydrogel and highly reflective polymerized poly(dodecyl glyceryl itaconate) (DGI) platelets to achieve ultrafast-response time, full-colour tunable range and high spatial resolution[82,83]. Also, a rolling technique of a PDMS and a triblock copolymer (PSPI) was developed to fabricate a concentric photonic crystal that replicates the hierarchical photonic structure found in the seed coat of *Margaritaria nobilis* fruits, which is used as a band-gap tunable, mechanochromic optical fiber[84].
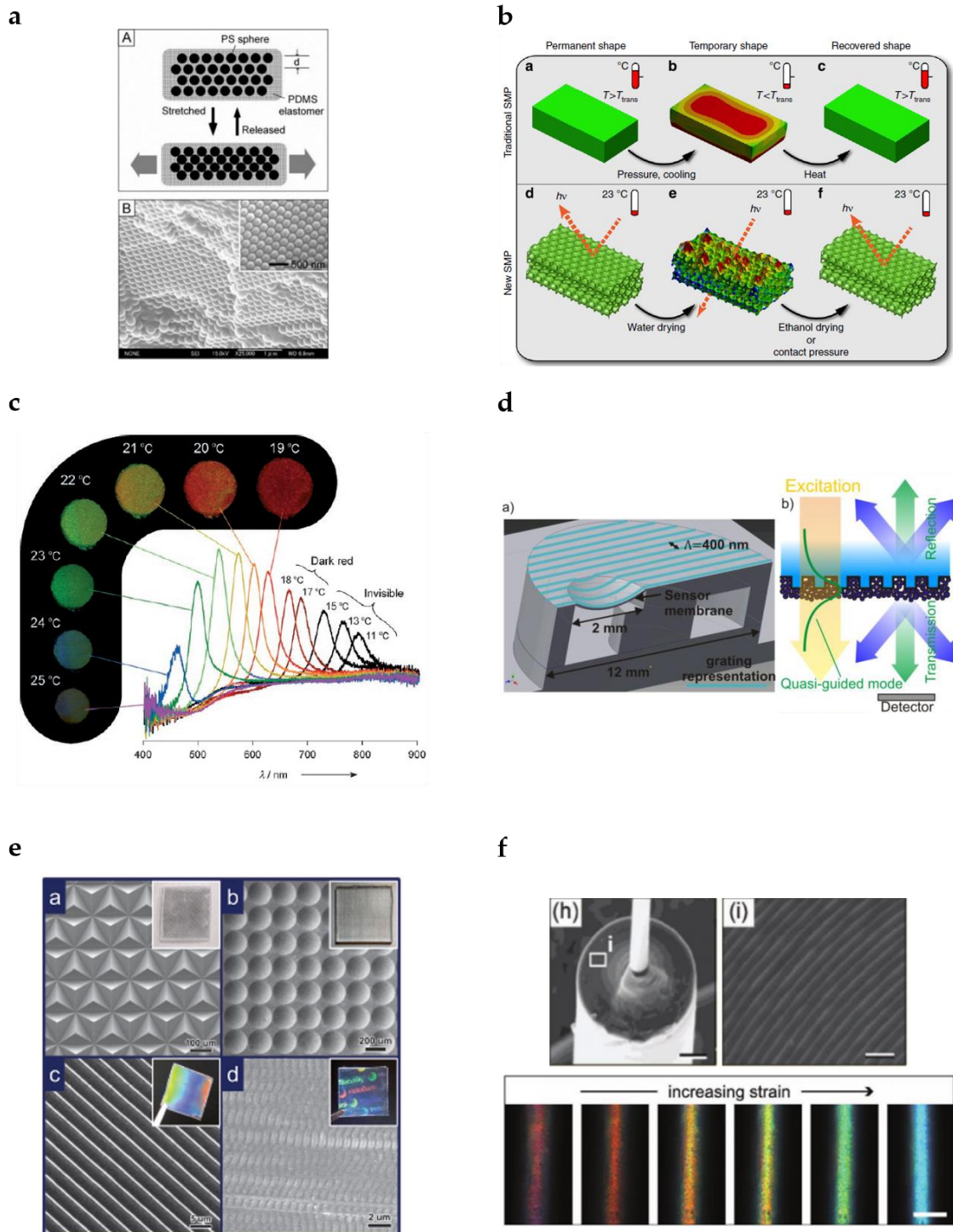
Figure 1-5. a) PDMS 3D opal photonic grating schematics and SEM image[54]. b) Working principle of shape-memory polymer opal[58]. c) Thermally-adjustable photochromic hydrogel spectrometry and representative images[60]. d) Schematic representation of a pressure sensor based on a flexible photonic crystal membrane[71]. e) SEM image of different micropatterned shape-memory polymers for programmable micro-optics[77]. f) Mechanochromic elastic fibre based on a bio-inspired multilayer of PDMS/PSPI[84].

1.2.1.3. Strain sensing based on light intensity variations in wrinkled surfaces

When light interacts with surfaces with textures of bigger dimensions than the light wavelength or randomly oriented corrugations, scattering phenomena occurs, leading to a shrinking on the transmitted and reflected light in the normal direction. To fabricate surface textures on elastic polymers, a very easy, cost-effective method to produce controlled surface corrugations on PDMS was proposed by Bowden *et al*.[85]. Relying on the linear buckling theory[86], that states that two materials of different Young modulus that experience certain mechanical strain produce surface buckles spontaneously to minimize the surface energy arising from the differential deformation, they evaporated gold layer to a heated (and therefore expanded) PDMS substrate. When the substrate is cooled down, the compression of the gold layer produces the sufficient mechanical strain to generate the surface wrinkles. Furthermore, they studied how these surface wrinkles can be controlled using micropatterned areas, such as microposts or ridges. Following this work, other approximations have been proposed such as the spin-coating of stiffer polymers to stretched PDMS[87], oxygen plasma or UVO treatment to generate a stiffer surface layer[88–90] or mediated by an ion bombarment[91].

Taking advantage of the transparency to visible light and the high elasticity of PDMS, many authors used this wrinkle generation strategy to build devices with mechanically-modulated transparency, having great potential to be used in smart windows or rewritable optical displays, among other applications. For example, Kim *et al*. fabricated unidirectional and bidirectional wrinkling patterns and demonstrated the dynamic tuning of optical diffraction, as well as their use as switchable screens and windows[88]. The same principle was used by Shrestha *et al*., where they fabricated a wrinkled pattern of a ZnO thin film on PDMS to build a mechanically tunable window[92]. Also, a dynamic micromirror with mechanically tunable reflection was developed by using an aluminium thin film coating as stiff layer on a shape memory polymer[93,94]. Li *et al*. demonstrated a very wide range of transparency tuning by combining the surface wrinkles and the microcracks that occur on the surface due to high strains[95]. In this line, surface wrinkled poly(vinyl alcohol) (PVA)/PDMS bilayer was also demonstrated as a mechanically switchable transparency material[96]. Taking advantage of the hydrophilicity of PVA, the mechanical stress was generated due to an increase of ambient humidity. Similarly, they demonstrated a similar phenomenon due to the thermal expansion of the material. Furthermore, Zeng *et al*. described the fabrication of three wrinkled PVA/PDMS bilayers with different response and dynamics to ambient moisture, which can be applied as water indicators or anticounterfeit tabs[97].

In addition, more complex nanostructures have been fabricated in combination with microscale surface wrinkles. For example, Lee *et al*. described the fabrication of a surface wrinkled PDMS with an array of nanoposts[90]. They used a template of nanoporous anodic aluminium oxide to fabricated the nanoposts by replica moulding, followed by PDMS stretching and ultraviolet-ozone (UVO) surface treatment. They demonstrated a highly

sensitive transparency to mechanical strain, as well as reversible hydrophilicity (and therefore, self-cleaning capabilities) due to the nanopost patterning. On the other hand, hierarchical surface wrinkles have been also proposed to achieve smaller wrinkle patterning and therefore structural coloration, in addition to tunable transparency[76,98].

Lastly and different from the mechanically tunable transparency applications, surface wrinkled elastomeric materials have been used not only as materials with mechanically tunable optical properties, but also as a template to build metal nanowires with tunable plasmonic resonances at the NIR[99]. Its combination with carbon nanotubes generate NIR-responsive dynamic wrinkling patterns for various optically-controlled devices[100]. To go further into the description of optically-responsive materials, light-responsive actuators are covered in detail in the following subsection.
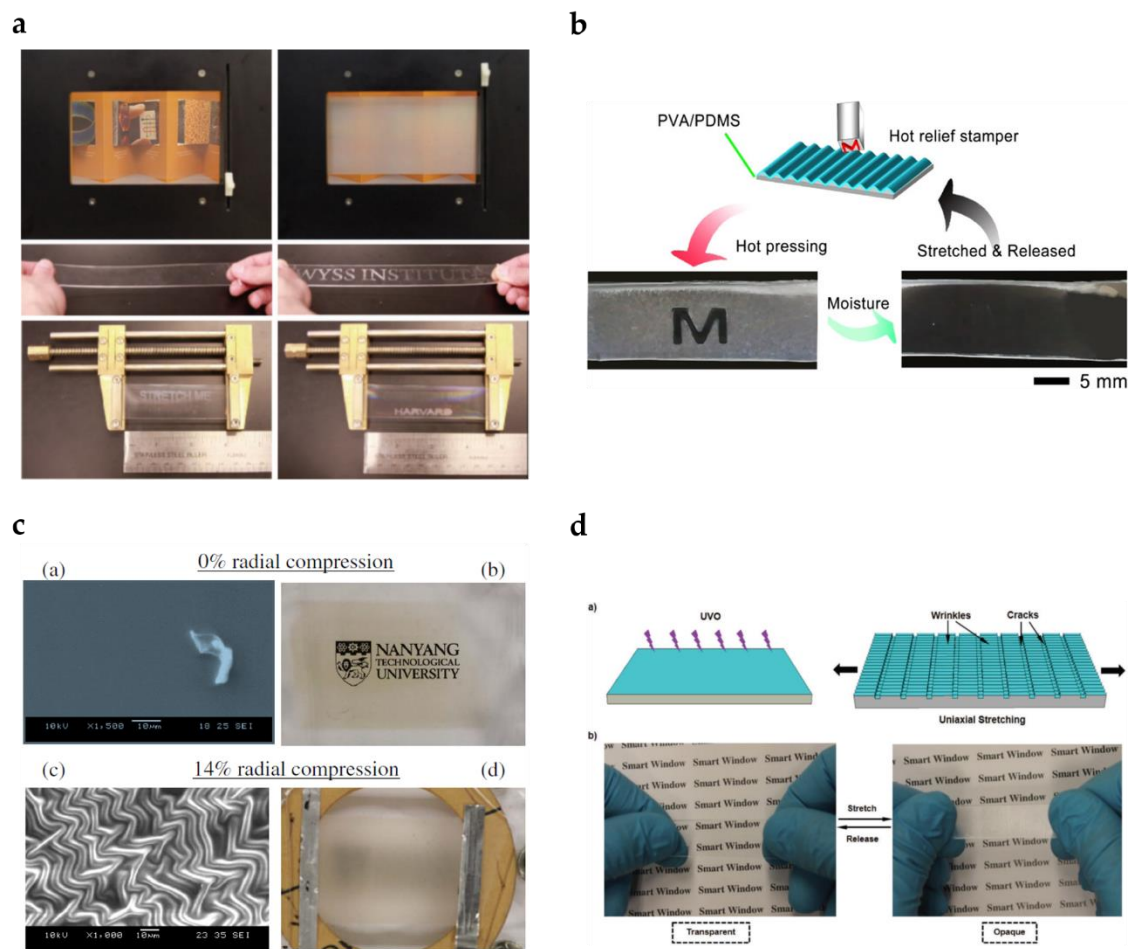
Figure 1-6. a) Mechanically-tunable switched transparency of wrinkled PDMS and proof of concept as dynamic window and switchable display[88]. b) Image of surface wrinkled PVA/PDMS film to develop switchable displays[96]. c) SEM image and macroscopic view of a tunable window based on zinc-oxide thin film on PDMS[92]. d) Switchable transparency in PDMS based on the formation of surface wrinkles and microcracks[95].

1.2.2. Soft optomechanical actuators

Recently, the interest on the development of materials for soft stimuli-responsive actuators has been growing considerably. These materials are especially appealing due to their advantages in respect to conventional hard actuators, such as the great adaptability to changing environments, strong resiliency to high loads, easy miniaturization and low-cost. Also, they can be modelled to incorporate extra functionalities, such as biocompatibility or self-sensing. Therefore, they can be used in a diverse range of applications, including wireless soft robotics[101–103], artificial muscles[104,105], self-regulated optical components[106], externally controlled switches[100] and energy harvesting[107,108]. Light-responsive actuators have the advantage to be remotely controlled, with high precision and rapid modulation. Also, they can have wavelength specificity, giving an extra feature of multifunctionality. In general, the driving motor of photoresponsive soft actuators are based on the light-induced heating (photothermia) or on the light-mediated rearrangement of dynamic chemical bonds (e.g. cis-trans isomerization)[109,110].

1.2.2.1. Soft photothermal actuators

Soft actuators driven by photogenerated heat are generally composed by a soft matrix (that are usually polymer or gel) and the photothermal agent, which can be based on inorganic materials (e.g. plasmonic nanoparticles), carbon-based materials or organic dyes[111], having each one a different heat generation physical mechanism. On the other hand, the actuation mechanism (the conversion of the photogenerated heat into mechanical work) is usually based on a differential thermal expansion between the photothermal agent and the substrate or based on a thermally-driven phase transition of the soft substrate, even though other approximations have been also explored.

Soft actuators based on differential thermal expansion

Photothermal actuators driven by a differential thermal expansion are generally composed by two distinguishable layers (i.e. bimorph actuators), which have a large mismatch on the thermal expansion coefficient (CTE) between layers. The differential volume expansion when the bilayered material is heated produces a stress that provokes the actuation. Thereby, the magnitude of the actuation is directly proportional to the difference in CTE and the temperature increase.

In general, polymers and elastomers present very high CTE, while metals and carbon-based materials have very low or even negative CTE[112]. Therefore, many authors choose this combination of materials. Regarding plasmonic materials, Shi *et al.* developed an actuator based on a bilayer of gold nanoparticles mixed on poly(N-isopropylacrylamide) (PNIPAM) and poly(acrylamide) (PAAm)[113]. In this system, gold nanoparticles are heated upon irradiation at the plasmon resonance wavelength, which produces the differential thermal expansion between both layers. Moreover, the effect is enhanced due to the desorption of water molecules from the polymer surface.

Plasmonic resonances are specially interesting to achieve wavelength selectivity. In this line, an actuator based on gold nanorods on PMMA was demonstrated[105]. The rational tuning of the nanorod dimensions makes possible to build an actuator with regions that are sensitive to different wavelength in the visible and NIR.

Carbon-based materials are also widely used to build bimorph actuators. For instance, many authors used graphene oxide deposited on polymers, such as PDMS or PMMA to develop actuators for different kind of applications. For example, they have been demonstrated as a light-controlled electrical switch, smart curtain that self-folds due to the sunlight irradiation or even as crawler and swimming robots[114–116]. Gao *et al.* took advantage of the water desorption effect to produce the opposite movement (to the light induced actuation) due to an increase of ambient humidity[117] and thereby construct a bi-functional mechanical gripper. Furthermore, graphene oxide sheets have been combined with other photothermal agents to give extra capabilities: Yang *et al.* incorporated gold nanoparticles in poly(dopamine) to achieve an enhanced responsivity of the actuator[118]. Graphene oxide has also been combined with carbon nanotubes in PDMS to achieve dual movement and twisting due to thermally-induced actuation and water desorption[119]. Single-wall carbon nanotubes have been used to build different photothermal actuators[120,121]. Actually, they present an optical absorption very dependent on the nanotube chirality, which has been exploited of to develop a multi-wavelength responsive actuator[122]. Finally, other photothermal agents have been applied for this type of photothermal actuators. For example, a trilayered actuator build of carbon black ink on polyethylene terephthalate (PET) and an acrylic layer was developed[107]. In this approximation, they demonstrated the combined actuation of thermal expansion and water desorption to build a mechanical gripper, crawling robot and a solar-driven mill, being appealing for innovative energy harvesting. Examples of other materials include the development of an artificial, NIR-responsive Venus flytrap based on a poly(3,4-ethylenedioxythiophene) (PEDOT) on PDMS bilayer[123] and a leaf-inspired, ($Ti_3C_2T_x$)– cellulose composite on a polycarbonate (PC) membrane. In the latter example, different photothermally driven smart devices were built, such as a worm-like robot, a light-controlled electrical switch, or applications in displays and camouflage[124].
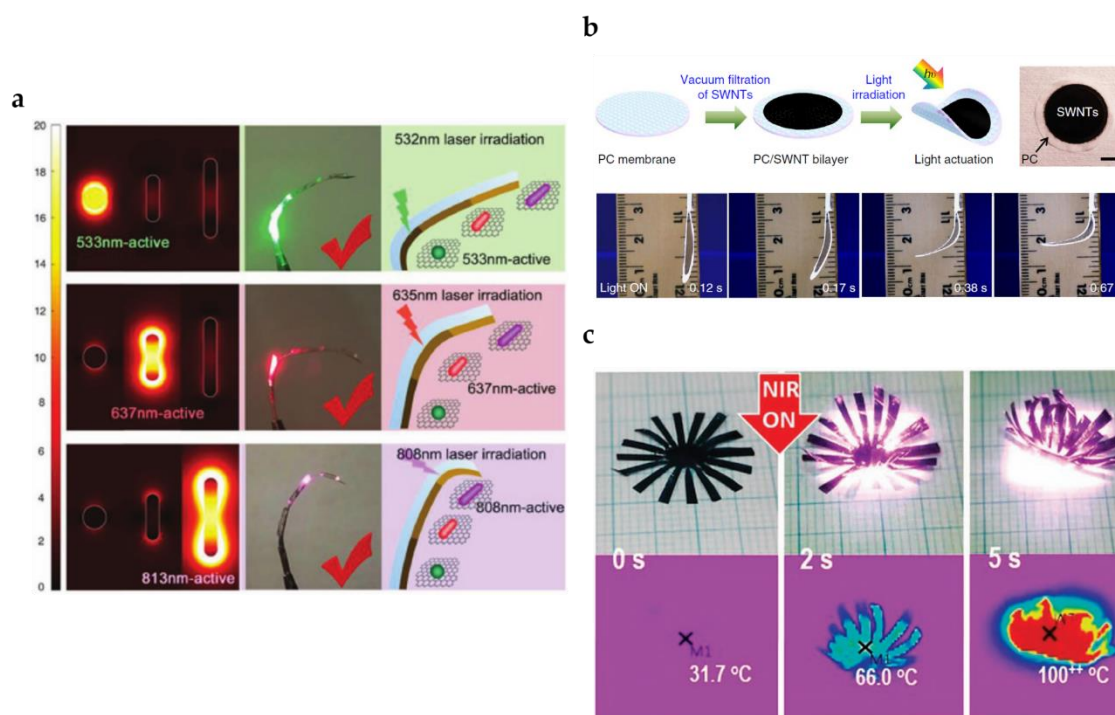
Figure 1-7. Soft actuators based on photothermally driven differential thermal expansion. a) Multi-wavelength responsive actuator based on gold nanorods[105]. b) PC/SWNT circular actuator[122]. c) Venus flower-like PEDOT-PDMS actuator under NIR irradiation[123].

Soft actuators based on thermally-driven phase transitions

The other common strategy to build soft photothermal actuators is to generate a phase change in the substrate material to generate the actuating mechanical force. Specifically, thermotropic liquid crystals (LC) are an ideal class of materials due to its softness and temperature-dependent macromolecular order. These can be classified into liquid crystal polymers (LCP), networks (LCN) or elastomers (LCE) depending on the macromolecular structure and their physicochemical properties[125].

Analogous to the actuators driven by thermal expansion, phase transitions actuators are also based on varied photothermal agents. For example, Shi *et al*. developed a colour-changing actuator based on a silver nanoparticle array on a LCE substrate[126]. In their approach, silver nanoparticles generate the necessary heat to drive a phase change on the LCE and produce a deflection on the structure. This deflection, in turn, modifies the nanoparticle arrangement, which produces a shift on the reflected colour. On the other hand, the easy-tailored wavelength specificity of plasmonic particles to build multifunctional photothermal actuators was demonstrated by Chen *et al*. They studied the plasmon resonance shift of encapsulated copper nanorods, which include in a poly(vinyl alcohol) (PVA) matrix to build wavelength-dependent actuators[127]. A different example of phase change-driven actuation was presented by Meder *et al*., in which they used gold nanoparticles in a liquid dispersion encapsulated in an elastomeric matrix. Thereby, the plasmonic-assisted heating evaporates the encapsulated liquid, causing an increase of pressure that drives a mechanical response[128]. Regarding carbon-based materials, chiral

SWNTs were used to develop a wavelength-selective light actuator on a VO_2 substrate[129]. Also, they demonstrate how the phase change in VO_2 is much faster than in conventional polymers (in the order of milliseconds). Another interesting approximation for light-driven actuation with LCN was presented by Zeng *et al*. Similarly to the smart curtain applications previously detailed, they developed a self-regulating artificial iris that was capable to modulate the light transmission depending on the incident light[106]. They based the device on a circular arrangement of 12 actuators build of a red dye mixed in a LCN matrix, which was cured using a circularly polarized light to achieve the actuation in a radial alignment. Finally, iron-based materials are also worth mentioning. The use of iron or iron-oxide powder in combination with a LCN was used to develop a dual stimuli actuator[130,131]. In their approximation, the authors can actuate the structure with the incident light, and at the same time produce movement by a magnetic field. This material was tested to develop a mechanical gripper that could be transported and rotated by a magnet and actuated using blue light.

Soft actuators based on other mechanisms

Mechanical structures based on bilayers can be used to produce the mechanical work due to thermal dehydration. Analogously to the thermal expansion driven actuators, the mechanism is driven by a differential expansion/contraction between the two layers due the absorption/desorption of the ambient humidity. As previously mentioned, it is possible to combine both effects (thermal expansion and thermal hydration) to produce an enhanced effect or a dual response[113,117,118]. Nonetheless, soft actuators only driven by thermal dehydration have been also developed. For example, a graphene oxide-polydopamine (PDA) actuator was developed to build origami self-folding devices[132]. Using this approach, programmable structures such a soft-robotic hand or a walker robot were demonstrated. In this line, Arazoe *et al*. built an autonomous actuator with high sensitivity and extremely fast response to variations in environmental humidity[133]. Their structures were based on π-stacked carbon nitride polymer (CNP) on a glass substrate of guanidinium carbonate (Gdm_2CO_3).

On the other hand, Mourran *et al*. studied soft, light-triggered microswimmers based on gold nanoparticles on PNIPAM matrix[134]. They studied different geometries to maximize the propelling motion of the soft-robot due to the swelling/shrinking of the structure produced by the rapid photogenerated heating of gold nanoparticles upon NIR irradiation. Lastly, a peculiar example of photothermal mediated actuation was demonstrated by Li *et al*.[135]. In this work, they build a magnetically-responsive actuator based on CrO_2 on PDMS and silk fibroin. Since the magnetization of CrO_2 is temperature dependent, the strength of the magnetic actuation could be controlled by the photogenerated heat.
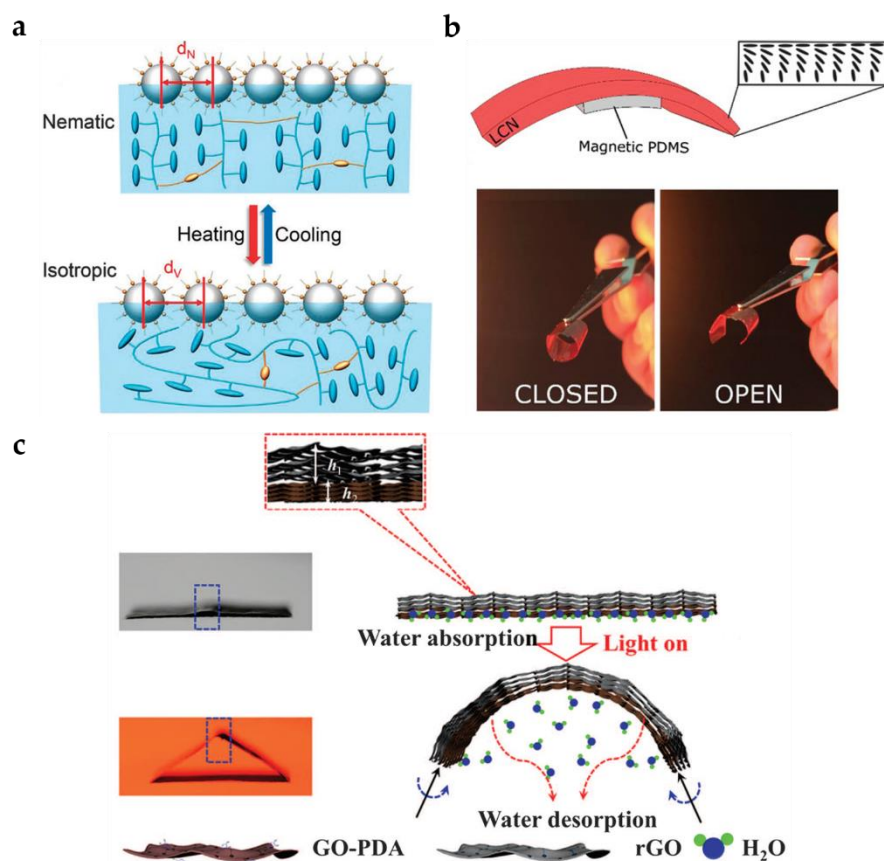
Figure 1-8. a) Soft actuator structure based on a silver nanoparticle array on a LCE. Photogenerated heat produce a phase change on the polymer and a change on interparticle distance[126]. b) Iron powder-PDMS + LCN actuator providing magnetic- and light-driven actuation[131]. c) GO-PDA actuator based on a differential water desorption[132].

1.2.2.2. Soft photochemical actuators

In general terms, photochemical actuators rely the conversion of light into mechanical work by the rearrangement of dynamic chemical bonds in the chemical structure of the actuator material. The endpoint macroscopic deformation is dependent on the collective structural reorganization at the molecular scale. The most common strategy is to include molecular photo-switches (such as azobenzenes, spiropyrans or fulgides) into the polymer-based actuator (usually build of LCNs or LCEs). These molecules have the ability to produce a cis-trans isomerization as a response to a certain light wavelength (usually ultraviolet and visible light). For example, Iamsaard *et al*. demonstrated the incorporation of azobenzene molecular switches into LCNs to build optomechanical devices. The resulting material can fold under the incident UV light due to the cis-trans isomerization of azobenzene molecules. Furthermore, depending on the molecule alignment in respect to the geometry of the actuator, different deformations can be achieved, from left-handed to right-handed helix twisting[136]. Many other authors followed the same principle to develop different devices, such as crawling and swimming soft microrobots[137,138], an artificial flytrap[103] or biomimetic artificial cilia for lab-on-a-chip applications[139].

On the other hand, another strategy that has been studied is based on new classes of cross-linked polymers that include exchangeable, reversible bonds into the structure to induce re-arrangements of the crosslinking network as a response to the incident light. For example, Ube *et al*. combined poly(hydrogenmethylsiloxane) and vinyl compounds to produce LCE containing dynamic covalent bonds based on ester and hydroxy groups[140]. These showed reversible bending upon UV and visible light, as well as rearrangement of the initial chemical structure by heat application. In parallel, liquid crystalline elastomers with allyl sulfide functional group were synthesized by other groups to fabricated optomechanical structures with different programmable actuation modes[141,142]. In this case, the light-to-mechanical conversion was driven by the exchange reaction between allyl sulfide groups. Other examples of reversible, dynamic chemical bonds for photochemical actuation include the use of hydrogen bonds[143].
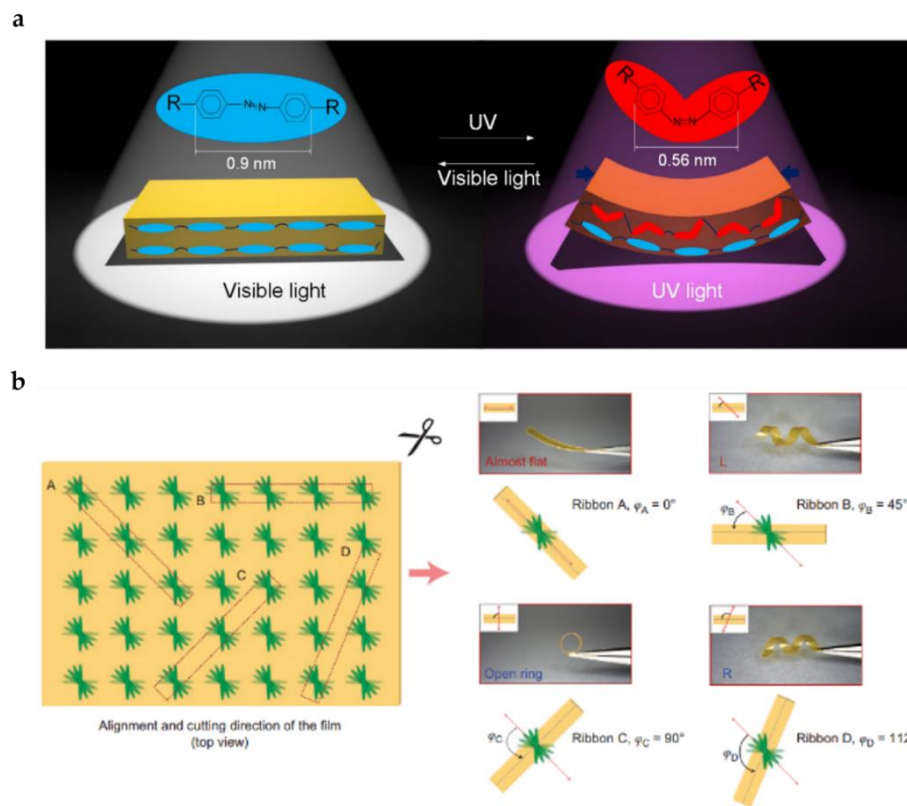
Figure 1-9. a) Light-mediated cis-trans isomerization of azobenzene inside a LCE matrix[137]. b) Different variety of chiral shapes depending on the cut orientation in respect to the reorientation angle of azobenzene (displayed in green)[136].

1.3. REFERENCES

1. Dawson, C., Vincent, J. F. V. & Rocca, A.-M. How pine cones open. *Nature* **390**, 668–668 (1997).

2. Chen, Z. *et al.* Mechanics without Muscles: Fast motion of the Venus flytrap and bio-inspired Robotics. *APS March Meeting Abstracts* (2013).

3. Ugolev, B. N. Wood as a natural smart material. *Wood Sci. Technol.* **48**, 553–568 (2014).

4. Teyssier, J., Saenko, S. V., van der Marel, D. & Milinkovitch, M. C. Photonic crystals cause active colour change in chameleons. *Nat. Comm.* **6**, 6368 (2015).

5. Lubelli, B., Nijland, T. & Van Hees, R. Self-healing of lime based mortars: microscopy observations on case studies. *Heron,* **56** (2011).

6. Thompson, B. S., Gandhi, M. V. & Kasiviswanathan, S. An introduction to smart materials and structures. *Mater. Des.* **13**, 3–9 (1992).

7. Curie, J. & Curie, P. Développement par compression de l'électricité polaire dans les cristaux hémièdres à faces inclinées. *Bull. Mineral.* **3**, 90–93 (1880).

8. Sun, L. *et al.* Stimulus-responsive shape memory materials: A review. *Mater. Des.* **33**, 577–640 (2012).

9. Ko, H. & Javey, A. Smart actuators and adhesives for reconfigurable matter. *Acc. Chem. Res.* **50**, 691–702 (2017).

10. Belie, N. D. *et al.* A review of self-healing concrete for damage management of structures. *Adv. Mater. Interfaces* **5**, 1800074 (2018).

11. Cheung, T.W., Li, L. Sustainable development of smart textiles: a review of 'self-functioning' abilities which makes textiles alive. *JTEFT* **4**, (2018).

12. Tällberg, R., Jelle, B. P., Loonen, R., Gao, T. & Hamdy, M. Comparison of the energy saving potential of adaptive and controllable smart windows: A state-of-the-art review and simulation studies of thermochromic, photochromic and electrochromic technologies. *Sol. Energ. Mater. Sol. Cells* **200**, 109828 (2019).

13. Kour, R. & Charif, A. Piezoelectric roads: energy harvesting method using piezoelectric technology. *Innov. Energ. Res.* **5**, 1000132 (2016).

14. Pandya, S. *et al.* New approach to waste-heat energy harvesting: pyroelectric energy conversion. *NPG Asia Mater.* **11**, 26 (2019).

15. Said, S. S., Campbell, S. & Hoare, T. Externally addressable smart drug delivery vehicles: current technologies and future directions. *Chem. Mater.* **31**, 4971–4989 (2019).

16. Mirvakili, S. M. & Hunter, I. W. Artificial muscles: mechanisms, applications, and challenges. *Adv. Mater.* **30**, 1704407 (2018).

17. Majidi, C. Soft-matter engineering for soft robotics. *Adv. Mater. Technol.* **4**, 1800477 (2019).

18. Murayama, H., Wada, D. & Igawa, H. Structural health monitoring by using fiber-optic distributed strain sensors with high spatial resolution. *Photonic Sens.* **3**, 355–376 (2013).

19. Amjadi, M., Kyung, K.-U., Park, I. & Sitti, M. Stretchable, skin-Mountable, and wearable strain sensors and their potential applications: A review. *Adv. Funct. Mater.* **26**, 1678–1698 (2016).

20. Kolle, M. & Lee, S. Progress and opportunities in soft photonics and biologically inspired optics. *Adv. Mater.* **30**, 1702669 (2018).

21. Cataldi, U., Cerminara, P., Sio, L. D., Caputo, R. & Umeton, C. P. Fabrication and characterization of stretchable PDMS structures doped with Au nanoparticles. *Mol. Cryst. Liq. Cryst.* **558**, 22–27 (2012).

22. Cataldi, U. *et al.* Growing gold nanoparticles on a flexible substrate to enable simple mechanical control of their plasmonic coupling. *J. Mater. Chem. C* **2**, 7927–7933 (2014).

23. Caputo, R., Cataldi, U., Bürgi, T. & Umeton, C. Plasmomechanics: A colour-changing device based on the plasmonic coupling of gold nanoparticles. *Mol. Cryst. Liq. Cryst.* **614**, 20–29 (2015).

24. Maurer, T. *et al.* The beginnings of plasmomechanics: towards plasmonic strain sensors. *Front. Mater. Sci.* **9**, 170–177 (2015).

25. Palermo, G. *et al.* Flexible thermo-plasmonics: an opto-mechanical control of the heat generated at the nanoscale. *Nanoscale* **10**, 16556–16561 (2018).

26. Lio, G. E., Palermo, G., Caputo, R. & De Luca, A. Opto-mechanical control of flexible plasmonic materials. *J. Appl. Phys.* **125**, 082533 (2019).

27. Millyard, M. G. *et al.* Stretch-induced plasmonic anisotropy of self-assembled gold nanoparticle mats. *Appl. Phys. Lett.* **100**, 073101 (2012).

28. Correa-Duarte, M. A. *et al.* Optical strain detectors based on gold/elastomer nanoparticulated films. *Gold Bull.* **40**, 6–14 (2007).

29. Chiang, Y.-L. *et al.* Mechanically tunable surface plasmon resonance based on gold nanoparticles and elastic membrane polydimethylsiloxane composite. *Appl. Phys. Lett.* **96**, 041904 (2010).

30. Han, X., Liu, Y. & Yin, Y. Colorimetric stress memory sensor based on disassembly of gold nanoparticle chains. *Nano Lett.* **14**, 2466–2470 (2014).

31. Topcu, G., Guner, T., Inci, E. & Demir, M. M. Colorimetric and plasmonic pressure sensors based on polyacrylamide/Au nanoparticles. *Sens. Actuator A Phys.* **295**, 503–511 (2019).

32. Burel, C. A. S. *et al.* Plasmonic-based mechanochromic microcapsules as strain sensors. *Small* **13**, 1701925 (2017).

33. Choe, A. *et al.* Stretchable and wearable colorimetric patches based on thermoresponsive plasmonic microgels embedded in a hydrogel film. *NPG Asia Mater.* **10**, 912–922 (2018).

34. Cui, Y., Zhou, J., Tamma, V. A. & Park, W. Dynamic tuning and symmetry lowering of fano resonance in plasmonic nanostructure. *ACS Nano* **6**, 2385–2393 (2012).

35. Kan, T., Matsumoto, K. & Shimoyama, I. Optical measurement of directional strain by scattering from nano-disk pairs aligned on an elastomer. *Nanotechnology* **23**, 315201 (2012).

36. Mahmoud, M. A. Polarized optomechanical response of silver nanodisc monolayers on an elastic substrate induced by stretching. *J. Phys. Chem. C* **119**, 19359–19366 (2015).

37. Wang, Y. *et al.* Strain-tunable plasmonic crystal using elevated nanodisks with polarization-dependent characteristics. *Appl. Phys. Lett.* **108**, 071110 (2016).

38. Gao, L. *et al.* Optics and nonlinear buckling mechanics in large-area, highly stretchable arrays of plasmonic nanostructures. *ACS Nano* **9**, 5968–5975 (2015).

39. Feng, D., Zhang, H., Xu, S., Tian, L. & Song, N. Fabrication of plasmonic nanoparticles on a wave shape PDMS substrate. *Plasmonics* **12**, 1627–1631 (2017).

40. Laible, F., Gollmer, D. A., Dickreuter, S., Kern, D. P. & Fleischer, M. Continuous reversible tuning of the gap size and plasmonic coupling of bow tie nanoantennas on flexible substrates. *Nanoscale* **10**, 14915–14922 (2018).

41. Aksu, S. *et al.* Flexible plasmonics on unconventional and nonplanar substrates. *Adv. Mater.* **23**, 4422–4430 (2011).

42. Pryce, I. M., Aydin, K., Kelaita, Y. A., Briggs, R. M. & Atwater, H. A. Characterization of the tunable response of highly strained compliant optical metamaterials. *Philos. Trans. Royal Soc. A* **369**, 3447–3455 (2011).

43. Pryce, I. M., Aydin, K., Kelaita, Y. A., Briggs, R. M. & Atwater, H. A. Highly strained compliant optical metamaterials with large frequency tunability. *Nano Lett.* **10**, 4222–4227 (2010).

44. Zhu, X., Shi, L., Liu, X., Zi, J. & Wang, Z. A mechanically tunable plasmonic structure composed of a monolayer array of metal-capped colloidal spheres on an elastomeric substrate. *Nano Res.* **3**, 807–812 (2010).

45. Zhu, X. *et al.* A stretch-tunable plasmonic structure with a polarization-dependent response. *Opt. Express* **20**, 5237–5242 (2012).

46. Lütolf, F., Casari, D. & Gallinet, B. Low-cost and large-area strain sensors based on plasmonic fano resonances. *Adv. Opt. Mater.* **4**, 715–721 (2016).

47. Zhang, X., Zhang, J., Liu, H., Su, X. & Wang, L. Soft plasmons with stretchable spectroscopic response based on thermally patterned gold nanoparticles. *Sci. Rep.* **4**, 4182 (2014).

48. Cole, R. M., Mahajan, S. & Baumberg, J. J. Stretchable metal-elastomer nanovoids for tunable plasmons. *Appl. Phys. Lett.* **95**, 154103 (2009).

49. Yoo, D., Johnson, T. W., Cherukulappurath, S., Norris, D. J. & Oh, S.-H. Template-stripped tunable plasmonic devices on stretchable and rollable substrates. *ACS Nano* **9**, 10647–10654 (2015).

50. Zhang, R., Wang, Q. & Zheng, X. Flexible mechanochromic photonic crystals: routes to visual sensors and their mechanical properties. *J. Mater. Chem. C* **6**, 3182–3199 (2018).

51. Vogel, N., Goerres, S., Landfester, K. & Weiss, C. K. A convenient method to produce close- and non-close-packed monolayers using direct assembly at the air–water interface and subsequent plasma-induced size reduction. *Macromol. Chem. Phys.* **212**, 1719–1734 (2011).

52. Weissman, J. M., Sunkara, H. B., Tse, A. S. & Asher, S. A. Thermally switchable periodicities and diffraction from mesoscopically ordered materials. *Science* **274**, 959–963 (1996).

53. Fudouzi, H. & Xia, Y. Colloidal crystals with tunable colors and their use as Photonic papers. *Langmuir* **19**, 9653–9660 (2003).

54. Fudouzi, H. & Sawada, T. Photonic rubber sheets with tunable color by elastic deformation. *Langmuir* **22**, 1365–1368 (2006).

55. Kontogeorgos, A. *et al.* Inducing symmetry breaking in nanostructures: anisotropic stretch-tuning photonic crystals. *Phys. Rev. Lett.* **105**, 233909 (2010).

56. Viel, B., Ruhl, T. & Hellmann, G. P. Reversible deformation of opal elastomers. *Chem. Mater.* **19**, 5673–5679 (2007).

57. Yetisen, A. K. *et al.* Photonic hydrogel sensors. *Biotechnol. Adv.* **34**, 250–271 (2016).

58. Fang, Y. *et al.* Reconfigurable photonic crystals enabled by pressure-responsive shape-memory polymers. *Nat. Commun.* **6**, 7416 (2015).

59. Arsenault, A. C. *et al.* From colour fingerprinting to the control of photoluminescence in elastic photonic crystals. *Nat. Mater.* **5**, 179–184 (2006).

60. Matsubara, K., Watanabe, M. & Takeoka, Y. A thermally adjustable multicolor photochromic hydrogel. *Angew. Chem. Int. Ed. Engl.* **46**, 1688–1692 (2007).

61. Burgess, I. B., Lončar, M. & Aizenberg, J. Structural colour in colourimetric sensors and indicators. *J. Mater. Chem. C* **1**, 6075–6086 (2013).

62. Zhu, C. *et al.* Magnetochromatic microcapsule arrays for displays. *Adv. Funct. Mater.* **21**, 2043–2048 (2011).

63. Kim, J., Choi, S.-E., Lee, H. & Kwon, S. Magnetochromatic microactuators for a micropixellated color-changing surface. *Adv. Mater.* **25**, 1415–1419 (2013).

64. Shang, L., Zhang, W., Xu, K. & Zhao, Y. Bio-inspired intelligent structural color materials. *Mater. Horiz.* **6**, 945–958 (2019).

65. Fudouzi, H. & Xia, Y. Photonic papers and inks: color writing with colorless materials. *Adv. Mater.* **15**, 892–896 (2003).

66. Yang, D., Ye, S. & Ge, J. From metastable colloidal crystalline arrays to fast responsive mechanochromic photonic gels: an organic gel for deformation-based display panels. *Adv. Funct. Mater.* **24**, 3197–3205 (2014).

67. Escudero, P., Yeste, J., Pascual-Izarra, C., Villa, R. & Alvarez, M. Color tunable pressure sensors based on polymer nanostructured membranes for optofluidic applications. *Sci. Rep.* **9**, 3259 (2019).

68. Guo, L. J. Nanoimprint lithography: methods and material requirements. *Adv. Mater.* **19**, 495–513 (2007).

69. Kooy, N., Mohamed, K., Pin, L. T. & Guan, O. S. A review of roll-to-roll nanoimprint lithography. *Nanoscale Res. Lett.* **9**, 320 (2014).

70. Espinha, A. *et al.* Hydroxypropyl cellulose photonic architectures by soft nanoimprinting lithography. *Nat. Photon.* **12**, 343–348 (2018).

71. Karrock, T. & Gerken, M. Pressure sensor based on flexible photonic crystal membrane. *Biomed. Opt. Express,* **6**, 4901–4911 (2015).

72. Nazirizadeh, Y., Karrock, T. & Gerken, M. Visual device for pressure measurement using photonic crystal slabs. *Opt. Lett.* **37**, 3081–3083 (2012).

73. Zhu, Y., Xu, M., Jin, H., Yang, J. & Dong, E. Chromatic surface microstructures on bionic soft robots for non-contact deformation measurement. in *2017 IEEE International Conference on Robotics and Automation (ICRA)* 6737–6742 (2017).

74. Suzumori, K., Mihara, M. & Wakimoto, S. Beautiful Flexible Microactuator changing its structural color with variable pitch grating. in *2011 IEEE International Conference on Robotics and Automation* 2771–2776 (2011).

75. Zhang, B., Cui, J., Duan, J. & Cui, M. A new fabrication method for nano-gratings based on the high flexibility of PDMS. *Opt. Laser Technol.* **92**, 206–210 (2017).

76. Li, Z., Liu, Y., Marin, M. & Yin, Y. Thickness-dependent wrinkling of PDMS films for programmable mechanochromic responses. *Nano Res.* **13**, 1882–1888 (2020).

77. Xu, H. *et al.* Deformable, programmable, and shape-memorizing micro-optics. *Adv. Funct. Mater.* **23**, 3299–3306 (2013).

78. Zhang, F. *et al.* Infrared detection based on localized modification of Morpho butterfly wings. *Adv. Mater.* **27**, 1077–1082 (2015).

79. Kustandi, T. S., Low, H. Y., Teng, J. H., Rodriguez, I. & Yin, R. Mimicking domino-like photonic nanostructures on butterfly wings. *Small* **5**, 574–578 (2009).

80. Pris, A. D. *et al.* Towards high-speed imaging of infrared photons with bio-inspired nanoarchitectures. *Nat. Photon.* **6**, 195–200 (2012).

81. Lu, T. *et al.* Near-infrared trigged stimulus-responsive photonic crystals with hierarchical structures. *ACS Appl. Mater. Interfaces* **9**, 34279–34285 (2017).

82. Yue, Y. *et al.* Mechano-actuated ultrafast full-colour switching in layered photonic hydrogels. *Nat. Commun.* **5**, 4659 (2014).

83. Haque, Md. A., Kurokawa, T., Kamita, G., Yue, Y. & Gong, J. P. Rapid and reversible tuning of structural color of a hydrogel over the entire visible spectrum by mechanical stimulation. *Chem. Mater.* **23**, 5200–5207 (2011).

84. Kolle, M. *et al.* Bio-inspired band-gap tunable elastic optical multilayer fibers. *Adv. Mater.* **25**, 2239–2245 (2013).

85. Bowden, N., Brittain, S., Evans, A. G., Hutchinson, J. W. & Whitesides, G. M. Spontaneous formation of ordered structures in thin films of metals supported on an elastomeric polymer. *Nature* **393**, 146–149 (1998).

86. Chen, C.-M. & Yang, S. Wrinkling instabilities in polymer films and their applications. *Polym. Int.* **61**, 1041–1047 (2012).

87. Jiang, B., Liu, L., Gao, Z. & Wang, W. A general and robust strategy for fabricating mechanoresponsive surface wrinkles with dynamic switchable transmittance. *Adv. Opt. Mater.* **6**, 1800195 (2018).

88. Kim, P. *et al.* Rational design of mechano-responsive optical materials by fine tuning the evolution of strain-dependent wrinkling patterns. *Adv. Opt. Mater.* **1**, 381–388 (2013).

89. Cheng, X. *et al.* Controlled fabrication of nanoscale wrinkle structure by fluorocarbon plasma for highly transparent triboelectric nanogenerator. *Microsyst. Nanoeng.* **3**, 16074 (2017).

90. Lee, S. G. *et al.* Switchable transparency and wetting of elastomeric smart windows. *Adv. Mater.* **22**, 5013–5017 (2010).

91. Park, H.-G., Jeong, H.-C., Jung, Y. H. & Seo, D.-S. Control of the wrinkle structure on surface-reformed poly(dimethylsiloxane) via ion-beam bombardment. *Sci. Rep.* **5**, 12356 (2015).

92. Shrestha, M. & Lau, G.-K. Tunable window device based on micro-wrinkling of nanometric zinc-oxide thin film on elastomer. *Opt. Lett.* **41**, 4433–4436 (2016).

93. Wang, Y. *et al.* Programmable localized wrinkling of thin films on shape memory polymers with application in nonuniform optical gratings. *Appl. Phys. Lett.* **112**, 251603 (2018).

94. Wang, Y. *et al.* Tunable surface wrinkling on shape memory polymers with application in smart micromirror. *Appl. Phys. Lett.* **114**, 193701 (2019).

95. Li, Z. *et al.* Harnessing surface wrinkling–cracking patterns for tunable optical transmittance. *Adv. Opt. Mater.* **5**, 1700425 (2017).

96. Jiang, B. *et al.* Fast dual-stimuli-responsive dynamic surface wrinkles with high bistability for smart windows and rewritable optical displays. *ACS Appl. Mater. Interfaces* **11**, 40406–40415 (2019).

97. Zeng, S. *et al.* Moisture-responsive wrinkling surfaces with tunable dynamics. *Adv. Mater.* **29**, 1700828 (2017).

98. Lin, G. *et al.* Self-similar hierarchical wrinkles as a potential multifunctional smart window with simultaneously tunable transparency, structural color, and droplet transport. *ACS Appl. Mater. Interfaces* **9**, 26510–26517 (2017).

99. Barelli, M., Repetto, D. & de Mongeot, F. B. Infrared plasmonics via self-organized anisotropic wrinkling of Au/PDMS nanoarrays. *ACS Appl. Polym. Mater.* **1**, 1334–1340 (2019).

100. Li, F., Hou, H., Yin, J. & Jiang, X. Near-infrared light–responsive dynamic wrinkle patterns. *Sci. Adv.* **4**, eaar5762 (2018).

101. Zhao, H., O'Brien, K., Li, S. & Shepherd, R. F. Optoelectronically innervated soft prosthetic hand via stretchable optical waveguides. *Sci. Robot.* **1**, eaai7529 (2016).

102. Zhao, Y. *et al.* Soft phototactic swimmer based on self-sustained hydrogel oscillator. *Sci. Robot.* **4**, eaax7112 (2019).

103. Wani, O. M., Zeng, H. & Priimagi, A. A light-driven artificial flytrap. *Nat. Commun.* **8**, 15546 (2017).

104. Li, M.-H. & Keller, P. Artificial muscles based on liquid crystal elastomers. *Philos. Trans. Royal Soc. A* **364**, 2763–2777 (2006).

105. Han, B. *et al.* Plasmonic-assisted graphene oxide artificial muscles. *Adv. Mater.* **31**, 1806386 (2019).

106. Zeng, H., Wani, O. M., Wasylczyk, P., Kaczmarek, R. & Priimagi, A. Self-regulating iris based on light-actuated liquid crystal elastomer. *Adv. Mater.* **29**, 1701814 (2017).

107. Li, J. *et al.* Photothermal bimorph actuators with in-built cooler for light mills, frequency switches, and soft Robots. *Adv. Funct. Mater.* **29**, 1808995 (2019).

108. Yu, L. & Yu, H. Light-powered tumbler movement of graphene oxide/polymer nanocomposites. *ACS Appl. Mater. Interfaces* **7**, 3834–3839 (2015).

109. Stoychev, G., Kirillova, A. & Ionov, L. Light-responsive shape-changing polymers. *Adv. Opt. Mater.* **7**, 1900067 (2019).

110. Mauro, M. Gel-based soft actuators driven by light. *J. Mater. Chem. B* **7**, 4234–4242 (2019).

111. Bisoyi, H. K., Urbas, A. M. & Li, Q. Soft materials driven by photothermal effect and their applications. *Adv. Opt. Mater.* **6**, 1800458 (2018).

112. Yoon, D., Son, Y.-W. & Cheong, H. Negative thermal expansion coefficient of graphene measured by Raman spectroscopy. *Nano Lett.* **11**, 3227–3231 (2011).

113. Shi, Q. *et al.* Photothermal surface plasmon resonance and interband transition-enhanced nanocomposite hydrogel actuators with hand-Like dynamic manipulation. *Adv. Opt. Mater.* **5**, 1700442 (2017).

114. Hu, Y. *et al.* A Graphene-based bimorph structure for design of high performance photoactuators. *Adv. Mater.* **27**, 7867–7873 (2015).

115. Wang, X., Jiao, N., Tung, S. & Liu, L. Photoresponsive graphene composite bilayer actuator for soft robots. *ACS Appl. Mater. Interfaces* **11**, 30290–30299 (2019).

116. Leeladhar, Raturi, P. & Singh, J. P. Sunlight-driven eco-friendly smart curtain based on infrared responsive graphene oxide-polymer photoactuators. *Sci. Rep.* **8**, 3687 (2018).

117. Gao, Y.-Y. *et al.* Gradient assembly of polymer nanospheres and graphene oxide sheets for dual-responsive soft actuators. *ACS Appl. Mater. Interfaces* **11**, 37130–37138 (2019).

118. Yang, Y., Liu, Y. & Shen, Y. Plasmonic-assisted graphene oxide films with enhanced photothermal actuation for soft robots. *Adv. Funct. Mater.* **30**, 1910172 (2020).

119. Wang, W. *et al.* Multistimulus responsive actuator with GO and carbon nanotube/PDMS bilayer structure for flexible and smart devices. *ACS Appl. Mater. Interfaces* **10**, 27215–27223 (2018).

120. Yamamoto, Y., Kanao, K., Arie, T., Akita, S. & Takei, K. Air ambient-operated pNIPAM-based flexible actuators stimulated by human body temperature and sunlight. *ACS Appl. Mater. Interfaces* **7**, 11002–11006 (2015).

121. Hu, Y. *et al.* Electrically and sunlight-driven actuator with versatile biomimetic motions based on rolled carbon nanotube bilayer composite. *Adv. Funct. Mater.* **27**, 1704388 (2017).

122. Zhang, X. *et al.* Photoactuators and motors based on carbon nanotubes with selective chirality distributions. *Nat. Commun.* **5**, 2983 (2014).

123. Lim, H. *et al.* Construction of a photothermal Venus flytrap from conductive polymer bimorphs. *NPG Asia Mater.* **9**, e399 (2017).

124. Cai, G., Ciou, J.-H., Liu, Y., Jiang, Y. & Lee, P. S. Leaf-inspired multiresponsive MXene-based actuator for programmable smart devices. *Sci. Adv.* **5**, eaaw7956 (2019).

125. White, T. J. & Broer, D. J. Programmable and adaptive mechanics with liquid crystal polymer networks and elastomers. *Nat. Mater.* **14**, 1087–1098 (2015).

126. Shi, Y., Zhu, C., Li, J., Wei, J. & Guo, J. A color-changing plasmonic actuator based on silver nanoparticle array/liquid crystalline elastomer nanocomposites. *New J. Chem.* **40**, 7311–7319 (2016).

127. Chen, J. *et al.* Space-confined seeded growth of Cu nanorods with strong surface plasmon resonance for photothermal actuation. *Angew. Chem. Int. Ed.* **58**, 9275–9281 (2019).

128. Meder, F., Naselli, G. A., Sadeghi, A. & Mazzolai, B. Remotely Light-powered soft fluidic actuators based on plasmonic-driven phase transitions in elastic constraint. *Adv. Mater.* **31**, 1905671 (2019).

129. Wang, T., Torres, D., Fernández, F. E., Wang, C. & Sepúlveda, N. Maximizing the performance of photothermal actuators by combining smart materials with supplementary advantages. *Sci. Adv.* **3**, e1602697 (2017).

130. da Cunha, M. *et al.* On untethered, dual magneto- and photoresponsive liquid crystal bilayer actuators showing bending and rotating motion. *Adv. Opt. Mater.* **7**, 1801604 (2019).

131. da Cunha, M. *et al.* An untethered magnetic- and light-responsive rotary gripper: shedding light on photoresponsive liquid crystal actuators. *Adv. Opt. Mater.* **7**, 1801643 (2019).

132. Mu, J. *et al.* Origami-inspired active graphene-based paper for programmable instant self-folding walking devices. *Sci. Adv.* **1**, e1500533 (2015).

133. Arazoe, H. *et al.* An autonomous actuator driven by fluctuations in ambient humidity. *Nat. Mater.* **15**, 1084–1089 (2016).

134. Mourran, A., Zhang, H., Vinokur, R. & Möller, M. Soft microrobots employing nonequilibrium actuation via plasmonic heating. *Adv. Mater.* **29**, 1604825 (2017).

135. Li, M. *et al.* Flexible magnetic composites for light-controlled actuation and interfaces. *Proc. Natl. Acad. Sci. U.S.A.* **115**, 8119–8124 (2018).

136. Iamsaard, S. *et al.* Conversion of light into macroscopic helical motion. *Nat. Chem.* **6**, 229–235 (2014).

137. Huang, C. *et al.* Miniaturized swimming soft robot with complex movement actuated and controlled by remote light signals. *Sci. Rep.* **5**, 17414 (2015).

138. Palagi, S. *et al.* Structured light enables biomimetic swimming and versatile locomotion of photoresponsive soft microrobots. *Nat. Mater.* **15**, 647–653 (2016).

139. van Oosten, C. L., Bastiaansen, C. W. M. & Broer, D. J. Printed artificial cilia from liquid-crystal network actuators modularly driven by light. *Nat. Mater.* **8**, 677–682 (2009).

140. Ube, T., Kawasaki, K. & Ikeda, T. Photomobile liquid-crystalline elastomers with rearrangeable networks. *Adv. Mater.* **28**, 8212–8217 (2016).

141. Qian, X. *et al.* Untethered recyclable tubular actuators with versatile locomotion for soft continuum robots. *Adv. Mater.* **30**, 1801103 (2018).

142. McBride, M. K. *et al.* A readily programmable, fully reversible shape-switching material. *Sci. Adv.* **4**, eaat4634 (2018).

143. Ni, B., Xie, H.-L., Tang, J., Zhang, H.-L. & Chen, E.-Q. A self-healing photoinduced-deformable material fabricated by liquid crystalline elastomers using multivalent hydrogen bonds as cross-linkers. *Chem. Commun.* **52**, 10257–10260 (2016).

2. Theoretical Foundations for Soft Plasmomechanical Metamaterials

The core of this thesis comprises the study and understanding of the optical and mechanical properties of soft plasmomechanical metamaterials in order to efficiently design and apply them for each particular application. In this chapter, the indispensable theoretical basis to comprehend all the aspects of the experimental work is given. In particular, this chapter focuses on the optical properties of plasmonic nanoparticles, photonic effects in micrometre-sized structures, mechanical properties of elastomers and the optomechanical and magnetomechanical responses in bendable and stretchable structures.

2.1. OPTICAL PROPERTIES OF PLASMONIC MATERIALS

When light interacts with a metal nanoparticle or nanostructure, the sinusoidal electric field of light exert forces on the conduction band electrons on the metal surface. These forces generate a collective wave motion of the surface electrons that provoke an enhancement of the electric field around the metal surface (in other words, it generates a *surface plasmon*)[1]. Thereby, the branch of optics that studies these phenomena is called *plasmonics*. Two different kinds of surface plasmons can be distinguished: surface plasmon polaritons (SPPs) are referred to the plasmons that are propagated through a metallic surface (Figure 2-1a), and localized surface plasmon resonances (LSPR) describe the plasmons that are confined around a single metallic nanoparticle (Figure 2-1b). As well as any other type of oscillation, surface plasmons have their inherent resonance frequencies. At the resonance frequency (i.e. light wavelength), the electromagnetic field enhancement around the metal surface is maximized, provoking an enhanced absorption or scattering of the incident light. Interestingly, plasmon resonances are extremely sensitive to the material, shape and size of the metal nanostructure, as well as its surrounding environment.
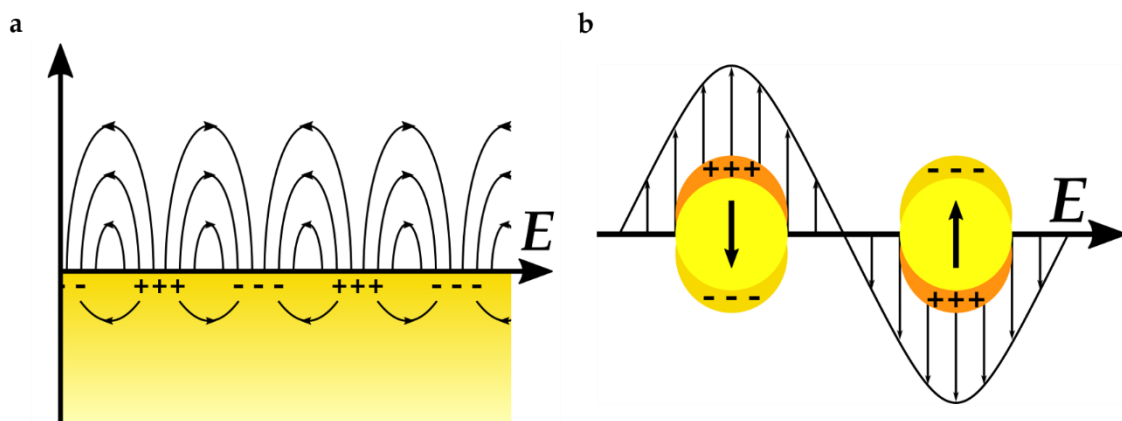
Figure 2-1. Schematic representation of (a) surface plasmon polaritons (SPP) and (b) localized plasmon resonances (LSPR).

Due to the large and sensitive electromagnetic enhancement in plasmonic materials, their applications are numerous and relevant in many fields. For example, the light confinement at sub-wavelength dimensions is of great interest to overcome the resolution of optical lithography, that is limited to the diffraction limit[2]. On the other hand, the electromagnetic enhancement around single plasmonic nanoparticles can lead to a very intense and localized light absorption. This energy is thereby converted into heat, which can be implemented in diverse ways, such as localized heating of tumour cells (i.e. hyperthermia)[3], catalysis of chemical reactions[4], or energy harvesting[5]. Besides, the high sensitivity to the material morphology can be exploited to develop high-resolution, reflective displays by the reversible tuning of the shape and size of the plasmonic nanostructures[6]. Also, the extreme sensitivity to the surrounding environment makes plasmonic materials ideal for chemical and biochemical sensing[7]. Furthermore, the surface plasmons amplify the inelastic light-

matter interaction used for Raman spectroscopy (SERS), allowing even single molecule detection[8].

From all the diverse approximations to use plasmonic materials, an important part of this thesis relies on the LSPR and on the enhanced light absorption in plasmonic nanostructures. Therefore, a detailed description of the physics behind the localized resonances is given subsequently, giving a special focus on the light absorption and the heat generation.

2.1.1. Localized Surface Plasmon Resonances

Mie theory describes the optical response of a spherical particle, involving the analytical solution of Maxwell's equations, to model the interaction between spherical metallic nanoparticles and electromagnetic radiation[9]. The electric polarizability of the material (i.e. the ability to form an electric dipole as a response to an external electric field) must be first calculated to determine the electric field enhancement around the nanoparticle surface. If the particle is much smaller than the wavelength of light, the quasistatic approximation can be applied. In this case, the phase of the electromagnetic field is constant over all the particle volume, so the spatial field distribution can be calculated assuming the simplified problem of a particle in an electrostatic field[10]. By solving the Laplace's equation taking this assumption into consideration, the electric polarizability can be obtained as:

$$\alpha(\omega) = 4\pi a^3 \frac{\varepsilon - \varepsilon_m}{\varepsilon + 2\varepsilon_m} \tag{2-1}$$

where $\alpha(\omega)$ is the complex polarizability of the nanoparticle, a is the nanoparticle radius, and ε and ε_m are the dielectric permittivity of the metal and the surrounding medium, respectively. Both are function of the excitation wavelength. Knowing the expression for the electric polarizability, and considering the geometrical cross-section of a spherical particle, the scattering (C_{sca}) and absorption (C_{abs}) cross-sections can be calculated as[11]:

$$C_{sca} = \sigma_{geom}\sigma_{sca} = \frac{8\pi}{3}k^4a^6 \left|\frac{\varepsilon - \varepsilon_m}{\varepsilon + 2\varepsilon_m}\right|^2 \tag{2-2}$$

$$C_{abs} = \sigma_{geom}\sigma_{abs} = 4\pi k a^3 \, Im\left|\frac{\varepsilon - \varepsilon_m}{\varepsilon + 2\varepsilon_m}\right| \tag{2-3}$$

Here, the real part of the metal dielectric function rules over the frequency position, while the imaginary part determines the broadening and absorption processes from the damping and dephasing of electron oscillations[12].

From these definitions, several important conclusions can be deduced. Since the permittivity ($\varepsilon(\omega)$) is frequency dependent, the absorption and scattering are maximized at a certain wavelength. From Equation 2-2 and 2-3, it is clear that scattering is maximized when Re[$\varepsilon(\omega)$] = -2ε_m (i.e. the Fröhlich condition[13]). This frequency can be extracted by applying the Drude model of electrical conduction[14]:

$$\varepsilon(\omega) = 1 - \frac{\omega_p^2}{\omega^2 + i\gamma_e\omega} + \sum_j \frac{f_j}{\omega_j^2 - \omega^2 - i\gamma_j\omega} \tag{2-4}$$

Here, ω_p and γ_e are the resonant frequency and damping constant of the bulk electron plasma of the metal, and f is the phenomenological oscillator strength representing the bound electrons. The sum on j is over different oscillators. From the Drude model, assuming that the frequency of electron collisions (γ) is small, the frequency of the dipole surface plasmon can be expressed as $\omega_{sp} \approx \omega_p/\sqrt{3}$ [15]. Therefore, the scattering cross-section can be expressed as:

$$C_{sca} = \frac{8\pi}{3} \frac{\omega_{sp}^4}{\left(\omega^2 - \omega_{sp}^2\right)^2 + \omega^2\gamma^2} k^4 a^6 \tag{2-5}$$

From this expression, it is demonstrated that the resonance presents a Lorentzian line shape, having its maximum at the natural frequency of the dipole surface plasmon.

As mentioned previously, there are many factors that can influence the frequency and the width of the plasmon resonance. A comprehensive revision of these dependencies is given subsequently.

Material dependency

The bulk electron plasma frequency ω_p (and therefore, the natural frequency of the dipole surface plasmon) is determined by the density of free electrons in the metal (N) and their effective mass (m_e), which is exclusively dependent on the material. It can be calculated as:

$$\omega_p = \sqrt{\frac{Ne^2}{\varepsilon_0 m_e}} \tag{2-6}$$

where e is the electron charge and ε_0 the electric permittivity of vacuum. However, in the case of metals, the bound electrons also contribute to the dielectric function, which is represented at the second term of the Drude model (Equation 2-4). This can be of great importance, for example, to understand the differences between the plasmonic resonance of gold and silver nanoparticles: even though both metals have similar bulk plasma electronic densities ($N = 5.9 \times 10^{22}$ and 5.9×10^{23} cm^{-3} for gold and silver, respectively), gold presents a red-shifted and damped plasmon resonance band in comparison to silver due to their different inter-band transitions onset[12,16].

Environment influence

Surface plasmon resonances are very sensitive to variations on the environment. The presence of a surrounding medium produces the screening of the Coulomb forces of the oscillating electrons, which shifts the plasmon resonance energy[17]. Therefore, plasmonic materials are ideal to be used for optical sensors and biosensors. A modification of the permittivity of the medium surrounding the nanoparticle (for instance, due to the adsorption of a biomolecule on the nanoparticle surface or a modification of the medium composition) will inevitably produce an alteration of the resonance frequency, in which the Fröhlich condition is fulfilled. On the other hand, the presence of another plasmonic particle in close vicinity can also affect the surface plasmon. In general terms, the strong electric field around a plasmonic nanoparticle enhances the electronic transitions of optical

absorbers and emitters in the near surroundings. For example, SERS is based in this phenomenon[18].

In the case of two metal nanoparticles that are in close proximity, the electric field of each nanoparticle can couple[19]. This near-field coupling modulates the frequency of the plasmon resonance, leading to a red-shift of the resonance wavelength. The red-shifting demonstrates that the coupling is energetically favourable, needing less energy to achieve the resonance, in comparison to the resonance of a single nanoparticle. However, is important to consider that the near-field coupling rapidly vanishes with the increasing distance due to the strong confinement of the electric field around the nanoparticle surface, which decays with distance at $1/r^3$, being r the distance from the particle[20].

Shape dependency

Until this point, only the spherical geometry has been considered. In order to take into account other possible geometries and symmetries, a more general description of the electric polarizability should be considered, adding a correction factor κ, that incorporates the dependence of the electron oscillations on the geometry, such as:

$$\alpha = (1 + \kappa)V \frac{\varepsilon - \varepsilon_m}{\varepsilon + \kappa \varepsilon_m} \tag{2-7}$$

note that the volume of the particle (V) has been included. In physical terms, κ determines the ease of the electrons to be polarized. In the case of a sphere, substituting κ ($\kappa = 2$) and the volume of a sphere, Equation 2-1 can be obtained. In the case of non-spherical geometries, several dipole or multipole resonances can occur due to the multiple axis of symmetry of the particles. For example, in the case of a nanorod (a = b ≠ c), two different resonances are present, corresponding to its major and minor axis, with a different κ for each axis. Therefore, a colloidal suspension of plasmonic nanorods present two different resonances, due to the random orientation of each particle in respect to the incident light.

Size dependency

From Equation 2-2 and 2-3, it is noticeable that an increase on the particle size implies a greater contribution of the scattering in comparison to absorption processes, as expected from the a^6 and a^3 dependencies. On the other hand, it is worth noting that the quasistatic approximation does not consider any dependence of the LSPR wavelength position on the particle size (a). However, an increase in size weakens the restoring force (i.e. the electrostatic interaction between the charges on the opposite sizes of the particle), thereby producing a red-shift. Furthermore, if the particle is sufficiently large, the quasistatic approximation is no longer valid and the accurate description of the plasmon resonance requires the full Mie solution. In this case, the dephasing between the electron oscillations and the incident electromagnetic field produce retardation effects that contribute to the LSPR by red-shifting and broadening the plasmon resonance. Eventually, if the particle size is comparable to the light wavelength or larger, not only the dipolar, but higher order multipole modes become relevant[21].

2.1.2. Photothermal effect

Heat generation

Since metallic nanoparticles are very inefficient light emitters, almost all the energy absorbed from the incident light is transformed into heat. The light absorption results from the photon energy dissipation due to inelastic processes, which warm up the whole metal lattice structure. Therefore, the efficiency to convert the incident light into heat (i.e. the photothermal efficiency, μ) can be expressed as the ratio between the absorption cross-section and the extinction cross-section, which is the sum of the absorption and scattering:

$$\mu = \frac{C_{abs}}{C_{abs} + C_{sca}} \qquad (2\text{-}8)$$

Since light scattering becomes predominant when the nanoparticle size increase, small particles present, in general, highest photothermal efficiency than their bigger counterparts.

The amount of heat (Q) generated by the light absorption can be obtained directly from the absorption cross section and the incident light irradiance (I) (i.e. light power per unit surface) as:

$$Q = C_{abs}I \qquad (2\text{-}9)$$

This expression is easily calculated for particle geometries with a known expression of the absorption cross-section. However, for more complex morphologies, the heat generation can be derived from the heat power density ($q(r)$) inside the nanoparticle, which considers the electronic current density and the electric field ($E(r)$) inside the metal. It can be expressed as[22]:

$$q(\boldsymbol{r}) = \frac{\omega}{2} Im\left(\varepsilon(\omega)\right)\varepsilon_0 \left|\boldsymbol{E}(\boldsymbol{r})\right|^2 \qquad (2\text{-}10)$$

Then, the generated heat Q is obtained by integrating the heat power density over the nanoparticle volume:

$$Q = \int_V q(\boldsymbol{r})d^3r \qquad (2\text{-}11)$$

However, for complex geometries, the electric field inside the nanoparticle needs to be calculated using computational techniques in order to obtain $q(r)$.

Temperature profile

The temperature increase of the nanoparticle and the surrounding medium can be determined from the resolution of the heat diffusion equation at the steady state regime[23]:

$$\nabla \cdot [\kappa(\boldsymbol{r})\nabla T(\boldsymbol{r})] = -q(\boldsymbol{r}) \qquad \text{inside the nanoparticle} \qquad (2\text{-}12)$$

$$\nabla \cdot [\kappa(\boldsymbol{r})\nabla T(\boldsymbol{r})] = 0 \qquad \text{outside the nanoparticle} \qquad (2\text{-}13)$$

In the case of a spherical metal nanoparticle, it can be reduced to:

$$\Delta T\,(r) = \Delta T_{NP}\frac{R}{r} \qquad\qquad r > R \qquad (2\text{-}14)$$

$$\Delta T\ (r) \approx \Delta T_{NP} \qquad \text{r} < \text{R} \tag{2-15}$$

note that inside the nanoparticle, the temperature is constant due to the high thermal conductivity of metals in comparison to any dielectric medium. Outside the nanoparticle, the temperature decreases with distance as *1/r*. The temperature difference ΔT is directly related to the heat generated by the light absorption, which can be expressed as:

$$\Delta T_{NP} = \frac{Q}{4\pi\kappa_m R} \tag{2-16}$$

For non-spherical particles, computational calculations are needed to estimate the temperature differences since there is no analytical expression to express the temperature difference as a function of the generated heat Q. However, some approaches have been proposed, such as a dimensionless geometrical correction factor[23] or a corrected value of the particle radius[24].

Finally, it is important to mention that the steady state is usually reached very fast in this type of processes (in the order of nanoseconds). The transient state duration is dependent on the characteristic size of the particle (e.g. a nanoparticle radius), which can be calculated as:

$$\tau \sim L^2 \frac{\rho C_p}{3\kappa_m} \tag{2-17}$$

where ρ is the mass density of the nanoparticle and C_p the specific heat of the metal.

In conclusion, the confinement of the light electric field around metal nanoparticles leads to enhanced absorptive and scattering processes, which are maximized when the light meets the resonance condition for the particle. The dependency on several factors (such as shape, size, composition and environment) has been detailed, meeting effects such as wavelength shifting and broadening of the resonances. A special focus has been given to the absorption processes and heat generation, remarking the linear dependency with the light irradiance and the fast reaching of the steady state.

2.2. STRUCTURAL COLORATION

While the previous section has treated the light-matter interaction at the subwavelength scale, and thereby inside the quasistatic limit, in this section the wave properties of light and its interaction with the material at the wavelength scale is considered. In particular, the structural coloration in photonic gratings is discussed.

Differently from typical coloured materials, which colouration arises from the presence of dyes, the structural coloration is generated from the light diffraction when interacts with micro-/nanostructured materials (e.g. photonic crystals or diffraction gratings). In nature, this phenomenon can be also found in several organisms, such as flowers, insects and mollusks[25].

2.2.1. Diffraction gratings

When a monochromatic light is incident on a periodic grating surface formed by grooves, it is diffracted into discrete directions. The diffracted light waves coming from each groove combines to form a diffracted wavefront (Figure 2-2a). The geometrical path difference between the light diffracted in adjacent grooves can be calculated as $d\sin\alpha + d\sin\beta$, being d the distance between grooves and α and β the angle of the incident and diffracted light, respectively. Therefore, by the principle of interference, the diffracted waves will experience a constructive interference only if this path difference equals to the light wavelength or a multiple of it. From this geometrical relationship, Bragg's law can be extracted:

$$m\lambda = d(\sin\alpha + \sin\beta) \tag{2-18}$$

Then, this formula can be reformulated in order to know the diffraction angle for a determined groove spacing and wavelength:

$$\beta(\lambda) = \arcsin(\frac{m\lambda}{d} - \sin\alpha) \tag{2-19}$$

Note that for m = 0 (and therefore β = -α), the wavelengths are not separated and the grating acts as a mirror, giving a specular reflection.

In the case of incident polychromatic light, the diffraction grating separates the different wavelengths of light into different diffraction angles, according to Equation 2-19. Therefore, for white light, the diffracted light is composed by the colour gradient range from violet to red that gives coloration to the grating material. Then, for a determined groove spacing and specific incident and diffracted angles, there exist more than a wavelength that satisfies Equation 2-18, which is indicated by the integer m. Considering that the constructive interferences occur when the path difference is equal to the light wavelength, the space needed to achieve another constructive interference is equal to wavelength multiples. These are the different diffraction orders, which, from the light grating equation, can be either positive or negative (Figure 2-2b). However, the number of orders is limited by the condition $\left|\frac{m\lambda}{d}\right| < 2$, since $|\sin\alpha + \sin\beta|$ cannot be greater than 2.
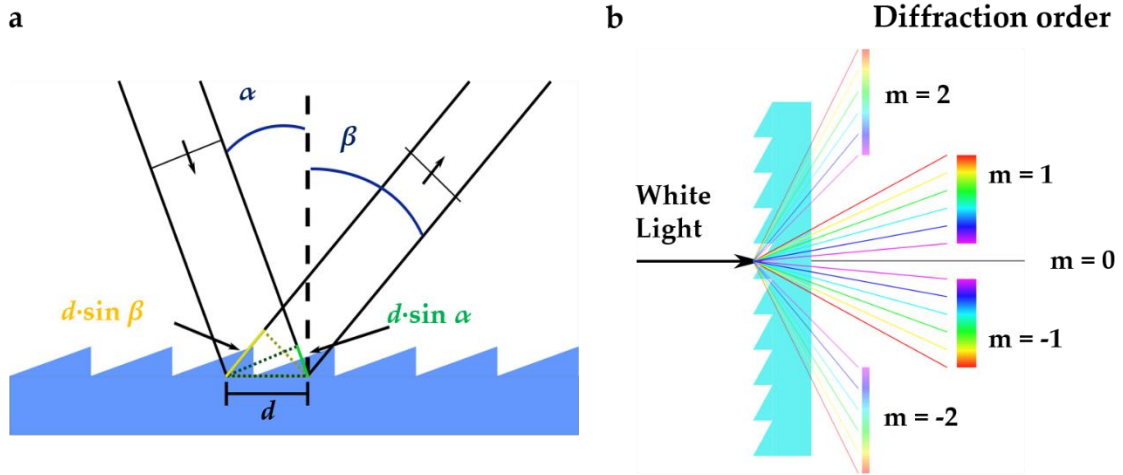
Figure 2-2. Schematic representation of the incident and diffracted wavefronts and the geometrical path differences between grooves.

Finally, it is worth noting the sign convention for the diffraction angles and orders to avoid any incoherence at the calculations. In Figure 2-3, a schematic representation of light diffraction in reflection and transmission modes is given to emphasize these assumptions. By convention, the angles of incidence and diffraction are measured from the grating normal to the beam. Also, the diffraction orders are positive if $\beta > -\alpha$ (diffraction occurs at the same side of the incident light in respect to the grating normal), and negative for $\beta < -\alpha$ (diffraction occurs at the opposite side of the incident light in respect to the grating normal).
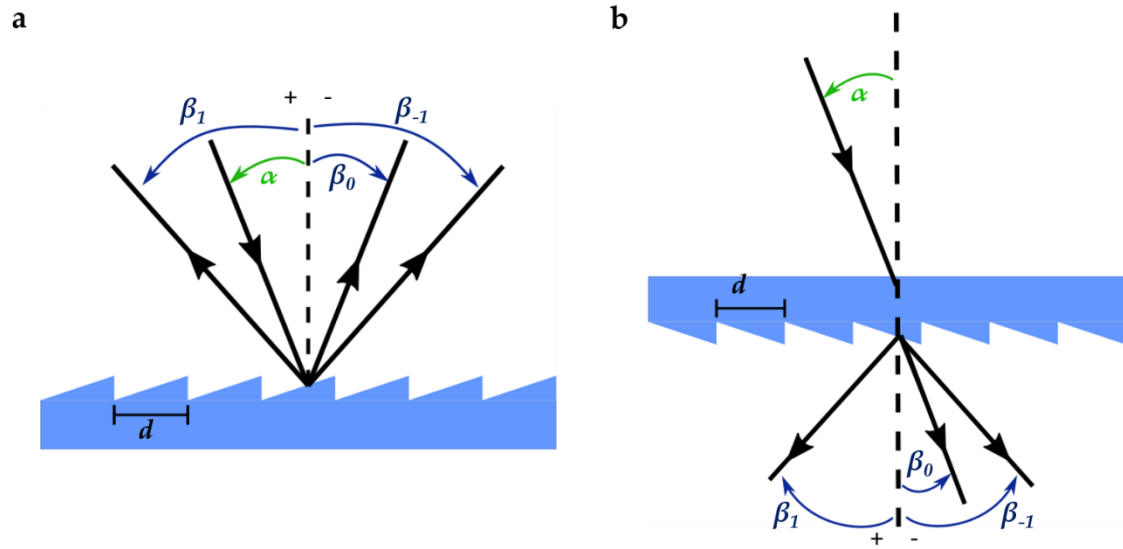
Figure 2-3. Schematic representation of light diffraction and sign convention for a) reflection mode and b) transmission mode.

2.2.2. Scattering

Aside from diffraction, when light is incident on a microstructured surface, a fraction of light is absorbed and the remaining fraction is scattered. Scattered light waves are randomly deviated in all directions in a hemisphere shape distribution normal to the surface plane.

This phenomenon occurs due to non-uniformities in the medium through they pass, such as the presence of nanoparticle (see previous discussion of plasmonics), small droplets or surface roughness. In the case of materials with microstructured surfaces, scattering usually arises from the imperfections on the grating grooves or due to a randomly-oriented surface patterning. Scattering causes a loss of directionality on an incident light beam, therefore materials that can regulate it dynamically are interesting for optomechanical devices since they can modulate the reflected/transmitted light intensity in a medium.

2.3. MECHANICAL PROPERTIES

2.3.1. Classical beam theory

The mechanical response of suspended systems (i.e. beams) to an applied load can be expressed in the most general way using Euler-Bernoulli's equation for a static beam:

$$\frac{d^2}{dx^2}\left(EI\frac{d^2w}{dx^2}\right) = q(x) \tag{2-20}$$

where E is the Young's modulus, I the area moment of inertia and $w(x)$ describes the deflection of the beam in the z direction. $q(x)$ represents the applied load per unit length to the beam. From this formula, the deflection of any type of beam can be modelled as a function of the applied load by integrating the formula and applying the adequate boundary conditions (taking into account that Euler-Bernoulli's equation is a fourth derivative, four boundary conditions are needed in any case). This thesis focusses the mechanical systems on the use of cantilevers (i.e. clamped-free beam) experiencing a uniformly distributed load (Figure 2-4a), which imply the following conditions:

- $w\ (0) = 0$. The base of the beam (the clamp) does not experience any deflection

- $w'\ (0) = 0$. Assuming that the clamp is horizontal, the derivative of the deflection at the clamp is also zero.

- $w''(L) = 0$. The bending moment at the tip of the cantilever (of length L) is zero.

- $w'''(L) = 0$. The shear stress at the tip of the cantilever is zero.

Therefore, the resulting formulas that describe the mechanical behaviour of a cantilever with a uniformly distributed load are the following:

1. Deflection

$$\delta(x) = \frac{-qx^2}{24EI}(6L^2 - 4Lx + x^2) \tag{2-21}$$

2. Slope

$$m(x) = \frac{-qx}{6EI}(3L^2 - 3Lx + x^2) \tag{2-22}$$

3. Bending moment

$$T(x) = \frac{q}{2}(L - x)^2 \tag{2-23}$$
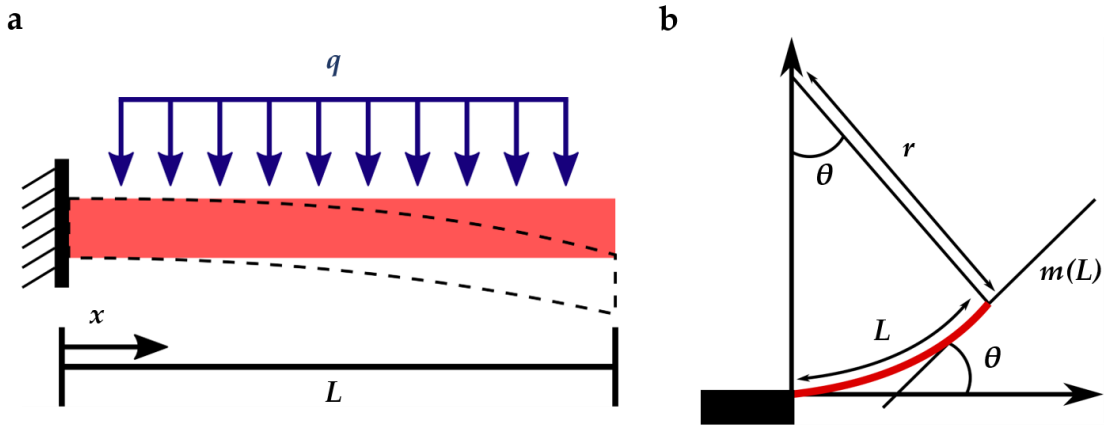
4. Shear stress

$$V(x) = -q(L - x) \tag{2-24}$$

In addition to these equations, the curvature of a cantilever beam it is usually described in polar coordinates by using the radius of curvature r and bending angle θ (Figure 2-4b). The trigonometric relationship between both systems is given by:

$$\theta = \arctan m(L) \tag{2-25}$$

$$r = \frac{180 \cdot L}{\pi \cdot \theta} \tag{2-26}$$

Where $m(L)$ is the slope of the curve that the cantilever describes.

Figure 2-4. Schematic diagram of curvature radius and bending angle in a cantilever.

Therefore, the cantilever behaviour can be fully modelled using these equations knowing the externally applied load. Regarding the load, this thesis will cover two different approaches: *i)* the generation of mechanical stress by the differential thermal expansion of the two materials composing a bimorph cantilever and *ii)* the magnetic forces generated due to the interaction between the cantilever magnetization and an external magnetic field.

2.3.2. Stress by differential thermal expansion

When bimorph cantilevers are heated, each layer of material expands differently, according to:

$$\Delta L_i = L \cdot \alpha_i \cdot \Delta T \tag{2-27}$$

being L the original length, α the thermal expansion coefficient (CTE) and ΔT the temperature variation. Sub-index i represents each individual layer. Therefore, the difference in the CTE (α) between both materials generates a mechanical stress, inducing the cantilever deflection in the direction of the material with lower CTE. For a bi-material system, the temperature induced bending can be estimated using its radius of curvature, r,

which depends on the stress from the temperature change (ΔT) and the residual stress that may be present in the material layers. It can be calculated by:

$$r = \frac{[(E_1 t_1{}^2)^2 + (E_2 t_2{}^2)^2 + 2E_1 E_2 t_1 t_2 (2t_1{}^2 + 3t_1 t_2 + 2t_2{}^2)]}{[6E_1 E_2 t_1 t_2 (t_1 + t_2)(\alpha_1 - \alpha_2)\Delta T]} \tag{2-28}$$

where t_i is the layer thickness of each layer, and E_i is the Young's modulus of the ith layer. If the thickness of the second layer is much smaller than that of the first ($t_1 \gg t_2$), Equation 2-28 can be simplified to:

$$r = \frac{\frac{E_1 t_1{}^2}{6E_2 t_2} + \frac{2t_1}{3}}{(\alpha_1 - \alpha_2)\Delta T} \tag{2-29}$$

Thus, r decreases (and therefore the curvature increases) as t_1 and E_1 decrease. Furthermore, r decreases as the difference in the CTE and the temperature change (ΔT) increase.

2.3.3. Stress by magnetic forces

Magnetic actuation in cantilevers can be performed by three different mechanisms: magnetostriction, magnetic torque or due to magnetic field gradients (magnetophoresis). Magnetostriction is a phenomenon that provokes a shape or volume change in materials under an applied magnetic field due to the reorientation of magnetic domains inside a ferromagnetic material[26]. On the other hand, a magnetic material of volume V experience a magnetic torque under an external magnetic field due to the misalignment of the magnetization of the material ($\vec{M}$) in respect to the applied magnetic field ($\vec{H}$), which tends to the alignment of both vectors[27,28]. It can be expressed as:

$$\vec{\tau}_{mag} = V\vec{M} \times \vec{H} \tag{2-30}$$

The magnetic torque ($\vec{\tau}_{mag}$) is orthogonal to both vectors, and it is maximized when $\vec{M}$ and $\vec{H}$ are perpendicular. Therefore, it is especially relevant in materials with high coercivity and it is very sensitive to angle variations. In the case of a cantilever having the magnetic moment along the beam and the magnetic field normal to its plane, the magnetic torque can be equated to the bending moment. Thereby:

$$\left(EI\frac{d^2 w}{dx^2}\right) = T = VMH \tag{2-31}$$

In the case that the magnetic force is applied at one single point, the torque is active from the clamp to that particular point and do not have any effect on the bending from that point towards the free end of the cantilever. However, in the case of homogeneous distribution of magnetic force along the cantilever, the active torque can be considered as an array of torques per unit sample over the sample length. It is expressed as:

$$T_a(x) = \frac{T}{L}(L - x) \tag{2-32}$$

Then, to determine the expression for the deflection, Equation 2-31 is double-integrated, giving:

$$\delta(x) = \frac{VHM}{6EI}\left[\frac{(L-x)^3}{L} - L^2 + 3Lx\right] \tag{2-33}$$

Also, in the presence of a magnetic field gradient, magnetic materials experience a force that pulls the material upward the magnetic field gradient, which is proportional to the magnetization and the magnetic field strength:

$$\vec{F}_{mag} = \nabla(\vec{M} \cdot \vec{B}) \tag{2-34}$$

In this case, the force is maximized when the magnetic moment is parallel to the external magnetic field, which is especially interesting for materials with no magnetic remanence, such as superparamagnetic particles[29] or vortex-like structures[30]. Therefore, the torque that the cantilever experiences can be expressed as:

$$\vec{T} = \vec{r} \times \vec{F}_{mag} \tag{2-35}$$

where $\vec{r}$ is the position vector through the cantilever length.

2.4. PHYSICOCHEMICAL PROPERTIES OF ELASTOMERS

Elastomers are a special type of polymers that present viscoelastic properties, low Young's modulus and very high elongation at break[31]. They are amorphous polymers with low transition glass temperature (T_g), which are composed by long chains which are cross-linked, usually based on carbon, oxygen, hydrogen and silicon. The molecular structure of elastomers can be schematized as the "meatball and spaghetti" structure (Figure 2-5a): in this representation, the long polymer chains are connected by covalent cross-linkages, and interact between each other by weak intermolecular forces. When stress is applied to the structure, it can be elongated because the long chains rearrange their positions, breaking the intermolecular forces to distribute the applied stress. However, once the stress is removed, it returns to its original position thanks to the covalent cross-linkages. This behaviour is observed in the bulk material as high elasticity and very high elongation at break comparing to other polymers (Figure 2-5b).

There are two main categories of elastomers: thermosets and thermoplastics. In general, they can be distinguished if their glass transition temperature is below (thermosets) or above room temperature (thermoplastics). This is translated into their response to heat: thermoset elastomers conserve their structure upon heat or pressure while thermoplastic elastomers melt when they are heated and their structure can be re-composed when it is cooled down again.
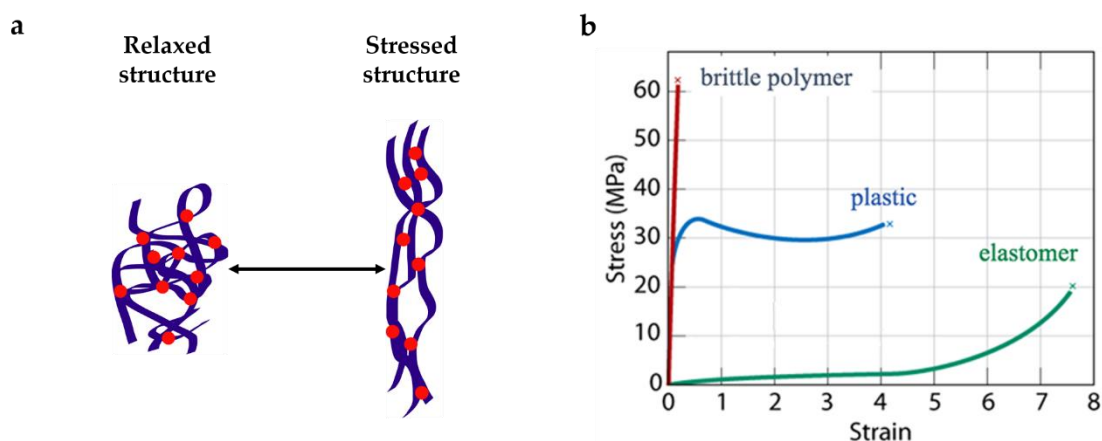
Figure 2-5. a) Schematic representation of the meatball-spaghetti structure for elastomers. b) Conceptual stress-strain curve comparison between brittle polymers, plastics and elastomers (adapted figure[32]).

2.4.1. PDMS

This thesis is focalized on the use of thermoset elastomers, and more specifically, on the use of polydimethylsiloxane (PDMS). PDMS is a silicon-based elastomer, which is composed by dimethylsiloxy units and trimethylsilyl end groups, having a general formula of MD_nM (where D and M are the dimethylsiloxy and trimethylsilyl units, respectively) (Figure 2-6). The molecular weight of PDMS (and therefore, its viscosity) is governed by the ratio between D and M units, since D-units have multiple reactive sites in contrast to M-units, which have only one and consequently forms the end of a polymer branch.
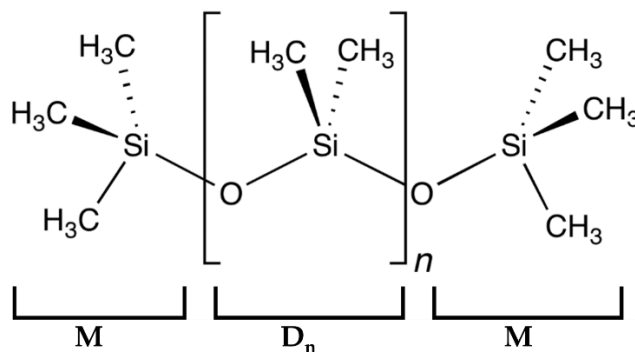
Figure 2-6. Chemical structure of PDMS

The covalent bonding between chains is based on an hydrosilylation reaction[33], which is catalysed by transition metals[34] (commercial catalysts are usually based of platinum complexes, which are added to the mixture in PDMS kits). This reaction takes place at room temperature in a very slow rate (>1 day), but it can be accelerated by increasing the temperature (i.e. <30 minutes @ 100ºC)[35]. The chemical reaction of cross-linking is detailed in Figure 2-7.
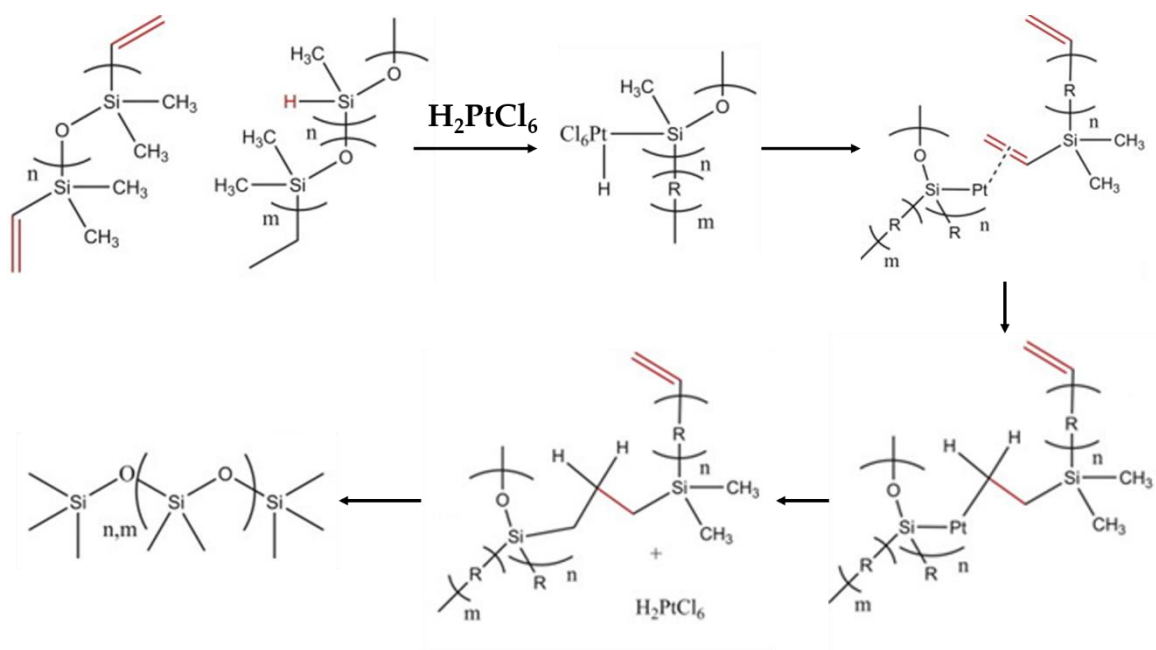
Figure 2-7. Hydrosilylation reaction of PDMS catalysed by a platinum-complex compound.

PDMS is hydrophobic and resistant to polar solvents. However, organic solvents (such as diisopropylamine, THF or chloroform) can diffuse inside and produce swelling or even dissolve the material[36]. At ambient pressure and temperature, it is optically transparent to visible and near-infrared light, inert, non-toxic and biocompatible. Like other polymers, it presents very low thermal conductivity and reasonably high thermal expansion coefficient. A list of the physicochemical properties of PDMS is included in Appendix B. Regarding the mechanical properties, PDMS Young's modulus range approximately from 0.2 to 3 MPa, which can be tuned by any factor that alters the amount of covalent cross-linkages in the structure, such as the ratio between dimethylsiloxy and trimethylsilyl units or the curing temperature[35]. It has a very high tensile strength (between 4 and 7 MPa) leading to elongations at break even higher than 100%[35].

The unique physicochemical properties and its low cost makes PDMS probably one of the most widely used polymers in materials science. For example, its thermal and chemical stability is used to apply PDMS as anticorrosion and antifouling protective coatings[37,38]. In addition to the thermal and chemical stability, the permeability to gases and biocompatibility makes this elastomer an ideal candidate for medical applications, such as topical skin treatment of contact lenses[39]. Also, it is compatible to several microfabrication techniques, such as soft lithography (e.g. micro-contact printing, replica moulding), spin-coating or plasma treatment, enabling the fabrication of sub-micron pattern features[40]. Taking advantage of this, PDMS is widely used for building microfluidic structures[41–43] to develop platforms for biomedical studies, such as cell culture substrates and scaffolds[44–46], biosensors[47,48] or organ-on-a-chip devices[49]. On the other hand, the hyperelasticity of PDMS makes it a special candidate for developing flexible and stretchable devices. For example, it is widely used as a structural material for MEMS[50–52] and micropumps[53,54]. Similarly, it is in

growing interest in the emerging field of soft-robotics[55–57] and artificial muscles[58,59], due to mechanical robustness, easy manipulation and low cost. Also, is used as a substrate for many wearable electronic devices to fully adapt to the human motion[60,61] or to develop strain sensors[62].

2.5. REFERENCES

1. Brongersma, M. L. & Shalaev, V. M. The case for plasmonics. *Science* **328**, 440–441 (2010).

2. Srituravanich, W., Fang, N., Sun, C., Luo, Q. & Zhang, X. Plasmonic nanolithography. *Nano Lett.* **4**, 1085–1088 (2004).

3. Huang, X. & El-Sayed, M. A. Plasmonic photo-thermal therapy (PPTT). *Alexandria J. Med.* **47**, 1–9 (2011).

4. Xiao, M. *et al.* Plasmon-enhanced chemical reactions. *J. Mater. Chem. A* **1**, 5790–5805 (2013).

5. Mulla, B. & Sabah, C. Multiband metamaterial absorber design based on plasmonic resonances for solar energy harvesting. *Plasmonics* **11**, 1313–1321 (2016).

6. James, T. D., Mulvaney, P. & Roberts, A. The plasmonic pixel: large area, wide gamut color reproduction using aluminum nanostructures. *Nano Lett.* **16**, 3817–3823 (2016).

7. Sepúlveda, B., Angelomé, P. C., Lechuga, L. M. & Liz-Marzán, L. M. LSPR-based nanobiosensors. *Nano Today* **4**, 244–251 (2009).

8. Vo-Dinh, T., Wang, H.-N. & Scaffidi, J. Plasmonic nanoprobes for SERS biosensing and bioimaging. *J. Biophoton.* **3**, 89–102 (2010).

9. Singh, R. & Soni, R. K. Chapter 11 - Laser-Induced Heating Synthesis of Hybrid Nanoparticles. in *Noble Metal-Metal Oxide Hybrid Nanoparticles*, 195–238 (2019)

10. Maier, S. A. *Plasmonics: Fundamentals and Applications*. (Springer Science & Business Media, 2007).

11. Bohren, C. F. & Huffman, D. R. *Absorption and Scattering of Light by Small Particles*. (John Wiley & Sons, 2008).

12. Jain, P. K. & El-Sayed, M. A. Plasmonic coupling in noble metal nanostructures. *Chem. Phys. Lett.* **487**, 153–164 (2010).

13. Fröhlich, H. *Theory of dielectrics; dielectric constant and dielectric loss.* (Clarendon Press, 1949).

14. Li, Y. *Plasmonic Optics: Theory and Applications*, 1–41 (SPIE Press Books, 2017).

15. Fan, X., Zheng, W. & Singh, D. J. Light scattering and surface plasmons on small spherical particles. *Light Sci. Appl.* **3**, e179 (2014).

16. Alvarez, M. M. *et al*. Optical absorption spectra of nanocrystal gold molecules. *J. Phys. Chem. B* **101**, 3706–3712 (1997).

17. Jain, P. K. & El-Sayed, M. A. Surface plasmon resonance sensitivity of metal nanostructures: physical basis and universal scaling in metal nanoshells. *J. Phys. Chem. C* **111**, 17451–17454 (2007).

18. Le Ru, E. C., Blackie, E., Meyer, M. & Etchegoin, P. G. Surface enhanced raman scattering enhancement factors: a comprehensive study. *J. Phys. Chem. C* **111**, 13794–13803 (2007).

19. Wang, X., Gogol, P., Cambril, E. & Palpant, B. Near- and far-field effects on the plasmon coupling in gold nanoparticle arrays. *J. Phys. Chem. C* **116**, 24741–24747 (2012).

20. Jain, P. K., Eustis, S. & El-Sayed, M. A. Plasmon coupling in nanorod assemblies: optical absorption, discrete dipole approximation simulation, and exciton-coupling model. *J. Phys. Chem. B* **110**, 18243–18253 (2006).

21. Coronado, E. A., Encina, E. R. & Stefani, F. D. Optical properties of metallic nanoparticles: manipulating light, heat and forces at the nanoscale. *Nanoscale* **3**, 4042–4059 (2011).

22. Baffou, G. & Quidant, R. Thermo-plasmonics: using metallic nanostructures as nano-sources of heat. *Laser Photo. Rev.* **7**, 171–187 (2013).

23. Baffou, G., Quidant, R. & García de Abajo, F. J. Nanoscale control of optical heating in complex plasmonic systems. *ACS Nano* **4**, 709–716 (2010).

24. Baffou, G., Quidant, R. & Girard, C. Thermoplasmonics modeling: A Green's function approach. *Phys. Rev. B* **82**, 165424 (2010).

25. Sun, J., Bhushan, B. & Tong, J. Structural coloration in nature. *RSC Advances* **3**, 14862–14889 (2013).

26. Hunter, D. *et al*. Giant magnetostriction in annealed Co 1−x Fe x thin-films. *Nat. Commun.* **2**, 518 (2011).

27. Adhikari, R., Sarkar, A. & Das, A. K. A versatile cantilever beam magnetometer for ex situ characterization of magnetic materials. *Rev. Sci. Instrum.* **83**, 013903 (2012).

28. Liu, J. A.-C., Gillen, J. H., Mishra, S. R., Evans, B. A. & Tracy, J. B. Photothermally and magnetically controlled reconfiguration of polymer composites for soft robotics. *Sci. Adv.* **5**, eaaw2897 (2019).

29. Kim, D. K., Zhang, Y., Voit, W., Rao, K. V. & Muhammed, M. Synthesis and characterization of surfactant-coated superparamagnetic monodispersed iron oxide nanoparticles. *J. Magn. Magn. Mater.* **225**, 30–36 (2001).

30. Streubel, R. *et al.* Magnetic vortices on closely packed spherically curved surfaces. *Phys. Rev. B* **85**, 174429 (2012).

31. Shanks, R. A. & Kong, I. General purpose elastomers: structure, chemistry, physics and performance. In *Advances in Elastomers I: Blends and Interpenetrating Networks* 11–45 (Springer, 2013).

32. Jr, W. D. C. & Rethwisch, D. G. *Fundamentals of Materials Science and Engineering: An Integrated Approach*. (2012).

33. Wang, D., Klein, J. & Mejía, E. Catalytic systems for the cross-linking of organosilicon polymers. *Chem. Asian J.* **12**, 1180–1197 (2017).

34. Putzien, S., Nuyken, O. & Kühn, F. E. Functionalized polysilalkylene siloxanes (polycarbosiloxanes) by hydrosilylation—Catalysis and synthesis. *Prog. Polym Sci.* **35**, 687–713 (2010).

35. Johnston, I. D., McCluskey, D. K., Tan, C. K. L. & Tracey, M. C. Mechanical characterization of bulk Sylgard 184 for microfluidics and microengineering. *J. Micromech. Microeng.* **24**, 035017 (2014).

36. Lee, J. N., Park, C. & Whitesides, G. M. Solvent compatibility of poly(dimethylsiloxane)-based microfluidic devices. *Anal. Chem.* **75**, 6544–6554 (2003).

37. Eduok, U., Faye, O. & Szpunar, J. Recent developments and applications of protective silicone coatings: A review of PDMS functional materials. *Prog. Org. Coat.* **111**, 124–163 (2017).

38. Zhang, H. & Chiao, M. Anti-fouling Coatings of poly(dimethylsiloxane) devices for biological and biomedical applications. *J. Med. Biol. Eng.* **35**, 143–155 (2015).

39. Bott, R., Gebert, M., Klykken, P., Mazeaud, I. & Thomas, X. Preparations for topical skin use and treatment. *J. Dtsch. Dermatol. Ges.*, **14**, 1061-1070 (2003).

40. Mata, A., Fleischman, A. J. & Roy, S. Characterization of polydimethylsiloxane (PDMS) properties for biomedical micro/nanosystems. *Biomed. Microdevices* **7**, 281–293 (2005).

41. McDonald, J. C. *et al.* Fabrication of microfluidic systems in poly(dimethylsiloxane). *Electrophoresis* **21**, 27–40 (2000).

42. Sia, S. K. & Whitesides, G. M. Microfluidic devices fabricated in Poly(dimethylsiloxane) for biological studies. *Electrophoresis* **24**, 3563–3576 (2003).

43. M, K. R. & Chakraborty, S. PDMS microfluidics: A mini review. *J. Appl. Polym. Sci.* **137**, 48958 (2020).

44. Torino, S., Corrado, B., Iodice, M. & Coppola, G. PDMS-based microfluidic devices for cell culture. *Inventions* **3**, 65 (2018).

45. Mi, Y., Chan, Y., Trau, D., Huang, P. & Chen, E. Micromolding of PDMS scaffolds and microwells for tissue culture and cell patterning: A new method of microfabrication by the self-assembled micropatterns of diblock copolymer micelles. *Polymer* **47**, 5124–5130 (2006).

46. Raczkowska, J. *et al.* Physico-chemical properties of PDMS surfaces suitable as substrates for cell cultures. *Appl. Surf. Sci.* **389**, 247–254 (2016).

47. Fürjes, P. *et al.* PDMS microfluidics developed for polymer based photonic biosensors. *Microsyst. Technol.* **21**, 581–590 (2015).

48. Pal, R. K., Pradhan, S., Narayanan, L. & Yadavalli, V. K. Micropatterned conductive polymer biosensors on flexible PDMS films. *Sens. Actuators B Chem.* **259**, 498–504 (2018).

49. Zhang, B., Korolj, A., Lai, B. F. L. & Radisic, M. Advances in organ-on-a-chip engineering. *Nat. Rev. Mater.* **3**, 257–278 (2018).

50. Schneider, F., Draheim, J., Kamberger, R. & Wallrabe, U. Process and material properties of polydimethylsiloxane (PDMS) for optical MEMS. *Sens. Actuators A Phys.* **151**, 95–99 (2009).

51. Kim, D.-S., Jeong, Y.-J., Lee, B.-K., Shanmugasundaram, A. & Lee, D.-W. Piezoresistive sensor-integrated PDMS cantilever: A new class of device for measuring the drug-induced changes in the mechanical activity of cardiomyocytes. *Sens. Actuators B Chem.* **240**, 566–572 (2017).

52. Nakamura, A. & Kawakami, S. An actuator–sensor hybrid device made of carbon-based polymer composite for self-sensing systems. *AIP Adv.* **9**, 065311 (2019).

53. J. Graf, N. & T. Bowser, M. A soft- polymer piezoelectric bimorph cantilever-actuated peristaltic micropump. *Lab Chip* **8**, 1664–1670 (2008).

54. Schneider, F., Draheim, J., Müller, C. & Wallrabe, U. Optimization of an adaptive PDMS-membrane lens with an integrated actuator. *Sens. Actuators A Phys.* **154**, 316–321 (2009).

55. Lim, H. *et al.* Construction of a photothermal Venus flytrap from conductive polymer bimorphs. *NPG Asia Mater.* **9**, e399 (2017).

56. Hu, Y., Lan, T., Wu, G., Zhu, Z. & Chen, W. A spongy graphene based bimorph actuator with ultra-large displacement towards biomimetic application. *Nanoscale* **6**, 12703–12709 (2014).

57. Wehner, M. *et al.* An integrated design and fabrication strategy for entirely soft, autonomous robots. *Nature* **536**, 451–455 (2016).

58. Mirvakili, S. M. & Hunter, I. W. Artificial muscles: mechanisms, applications, and challenges. *Adv. Mater.* **30**, 1704407 (2018).

59. Makino, E., Mineta, T., Mitsunaga, T., Kawashima, T. & Shibata, T. Sphincter actuator fabricated with PDMS/SMA bimorph cantilevers. *Microelectron. Eng.* **88**, 2662–2665 (2011).

60. Yeo, J. C. *et al.* Flexible and stretchable strain sensing actuator for wearable soft robotic applications. *Adv. Mater. Technol.* **1**, 1600018 (2016).

61. Chen, J. *et al.* Polydimethylsiloxane (PDMS)-based flexible resistive strain sensors for wearable applications. *Appl. Sci.* **8**, 345 (2018).

62. Ruhhammer, J., Zens, M., Goldschmidtboeing, F., Seifert, A. & Woias, P. Highly elastic conductive polymeric MEMS. *Sci. Technol. Adv. Mater.* **16**, 015003 (2015).

3. Ultrabroadband Light Absorbing Fe/Polymer Flexible Metamaterial for Soft Optomechanical Devices

Ultrabroadband light absorbers are attracting increasing interest for applications in energy harvesting, photodetection, self-regulated devices or soft robotics. However, current broadband absorbers show detrimental insufficient absorption spectral range, or light angle and polarization dependence. In this chapter, the unexplored optical properties of highly-damped plasmonic materials are combined with the infrared absorption of thin polymer films to enable developing ultrabroadband light-absorbing soft metamaterials. The developed metamaterial, composed of a nanostructured Fe layer mechanically coupled to a thin polydimethylsiloxane (PDMS) film, shows unprecedented ultrabroadband and angle-independent optical absorption (averaging 84% within 300-18000 nm). The excellent photothermal efficiency and large thermal-expansion mismatch of the metamaterial is efficiently transformed into large mechanical deflections, which are exploited to show an artificial iris that self-regulates the transmitted light power from UV to LWIR, an untethered light-controlled mechanical gripper and a light-triggered electrical switch.

3.1. INTRODUCTION

Efficient broadband light absorption is crucial for many relevant photonic devices, such as solar cells[1,2], photodetectors[3,4] or soft-actuators[5]. As their performance depends on the ability to collect and convert light into other types of energies, novel concepts are being studied to maximize the absorption spectral window[6]. Recent broadband absorbing metamaterials include microstructures with resonators[7,8], plasmonic nano-composites[9,10], or graphene-based metamaterials[11]. Plasmonic nanostructures are particularly interesting to achieve strong absorbing metamaterials due to their easily tuneable optical properties. However, highly efficient light absorption is restricted to small particles compared to the light wavelength and to the excitation of localized surface plasmon resonances in a narrow spectral band. Although resonances can be tuned by size increasing, this imposes a large scattering/absorption ratio enhancement in most plasmonic materials. This effect is more noticeable for resonances in the infrared (IR), where these materials behave as near perfect conductors with minimal radiation penetration, thereby drastically increasing the reflected and scattered light. To expand the absorption range of plasmonic materials, the use of plasmonic nanoparticles of different sizes[12–15], their combination with dielectric layers[16,17], or the nanometric control of their near-field interaction[18,19] have been proposed. Additionally, apart from conventional photonic/plasmonic materials, there are other materials, like transition metals, which have been barely explored for photonic applications and/or efficient light absorption, as is the case of metallic iron (Fe). Fe shows a negative real part of the dielectric constant from the ultraviolet (UV) to the far-IR, which is an essential condition for the generation of plasmonic resonances. However, its imaginary part is much larger than in classical plasmonic materials. This results in a large plasmonic damping, which prevents the generation of sharp resonances, hampering its application in typical plasmonic applications such as refractometric sensors or biosensors[20], or the generation of enhanced electromagnetic fields at the nanostructures edges. However, these broad resonances make Fe ideal for broadband absorption applications. Fe enables a deeper electromagnetic field penetration inside the nanostructures, thus minimizing light reflectance/scattering. This feature is particularly appealing to combine nanostructured-Fe absorption with highly absorbing materials in the far-IR, like flexible polymers, whose enhanced absorption bands in the midwave-IR–longwave-IR (MWIR-LWIR) range have been rarely exploited for practical photonic applications. Incorporating ultrabroadband light absorption into polymers is particularly appealing for developing light-controlled soft actuators, as a base for innovative applications in soft robotics[21–25], energy harvesters[26–28] or self-regulated devices[29–31]. Importantly, these applications demand strong ultrabroadband light absorption, incident light angle and polarization independence (due to the large mechanical deflections), and high compliance between the metal and the flexible polymer substrate. However, all the soft actuators reported to date fail in at least one of these requirements.

Here, it is shown that the highly-damped plasmons in nanostructured Fe films exhibit extremely efficient broadband absorption in the UV–near-infrared (UV-NIR) with minimal reflectance in the MWIR-LWIR. This, combined with flexible polydimethylsiloxane (PDMS)

films (with enhanced light absorption in the MWIR-LWIR) enables developing soft metamaterials with an unprecedented ultrabroadband absorption range. This inexpensive novel metamaterial shows an angle-independent and efficient ultrabroadband optical absorption (average 84% within 300-18000 nm), which results in an excellent photothermal conversion efficiency. Due to the large thermal-expansion-coefficient mismatch between both materials, this is efficiently transformed into large mechanical deflections. These deflections are exploited to demonstrate soft photo-thermo-mechanical devices: (i) a power-free, ultrabroadband, self-regulated artificial iris that adjusts its aperture to the light intensity (from UV to far-IR), thus mimicking a natural iris or acting as a self-regulated radiation protector; (ii) an optically-controlled mechanical gripper, enabling picking, transporting and releasing cargos, and (iii) an untethered optically-triggered electrical switch.

## 3.2. RESULTS AND DISCUSSION

3.2.1. Theoretical analysis

To highlight the key differences between classical plasmonic absorbers and highly-damped plasmonic materials for ultrabroadband absorption applications, the scattering and absorption cross sections of identical gold (Au) and Fe structures are compared by finite-difference time-domain (FDTD) simulations. As a rule of thumb, to achieve strong absorption, the absorption/scattering ratio of the structures should be maximized, whereas very broad/flat spectra are required to reach the ultrabroadband absorption. From the FDTD calculations, it is shown that Fe semi-shell structures of 500 nm diameter exhibit approximately 7-fold larger absorption cross-section compared to their Au counterparts (Figure 3-1a). Moreover, the large scattering observed in the Au structures is dramatically reduced (between 2 and 3-fold) in the Fe semi-shell. Overall, the absorption/scattering ratio of Fe semi-shells can be up to 25-fold larger than Au semi-shells in the NIR, thus highlighting their potential to achieve intense light absorption efficiency. The reason behind this stark difference is the much higher penetration of the light inside the highly damped plasmonic Fe semi-shell compared to the Au structures, as shown by the electric field distribution around and inside the metal structures, which is almost 6-fold higher at the central thickest part of the Fe metal structure (Figure 3-1b). The larger light penetration in Fe is endowed by both the lower absolute value of the real part of the dielectric constant and the much higher imaginary part (up to 20-fold larger at 800 nm wavelength compared to Au). These large differences in absorption/scattering are also clearly observed in other common plasmonic materials, like Ag and Al semi-shells (Figure 3-2a).

Interestingly, the Fe semi-shells also enable stronger absorption in a much broader spectral range (from UV to the NIR), even covering wavelengths shorter than the size of the nanostructures. In addition to the scattering reduction compared to Au, the FDTD simulations show that the forward scattering is favoured with respect to the back-scattering (Figure 3-2b). This is essential to allow the MWIR and LWIR radiation (that is not so efficiently absorbed by the Fe structures) to be transmitted and totally absorbed by another

material, such as a thin flexible polymer layer with strong absorption bands in this range. Notably, the structure geometry also plays a major role to maximize the spectral absorption range, where other more common geometries, such as spheres or discs, show substantially lower absorption bands (Figure 3-1c). Finally, it is worth highlighting that this type of highly damped plasmonic Fe semi-shell structures can be easily obtained by colloidal self-assembly and highly directional Fe evaporation[32,33]. In addition, the inherent potential to adjust the colloidal size and separation distance between self-assembled structures can also be exploited to attain even broader absorption bands.
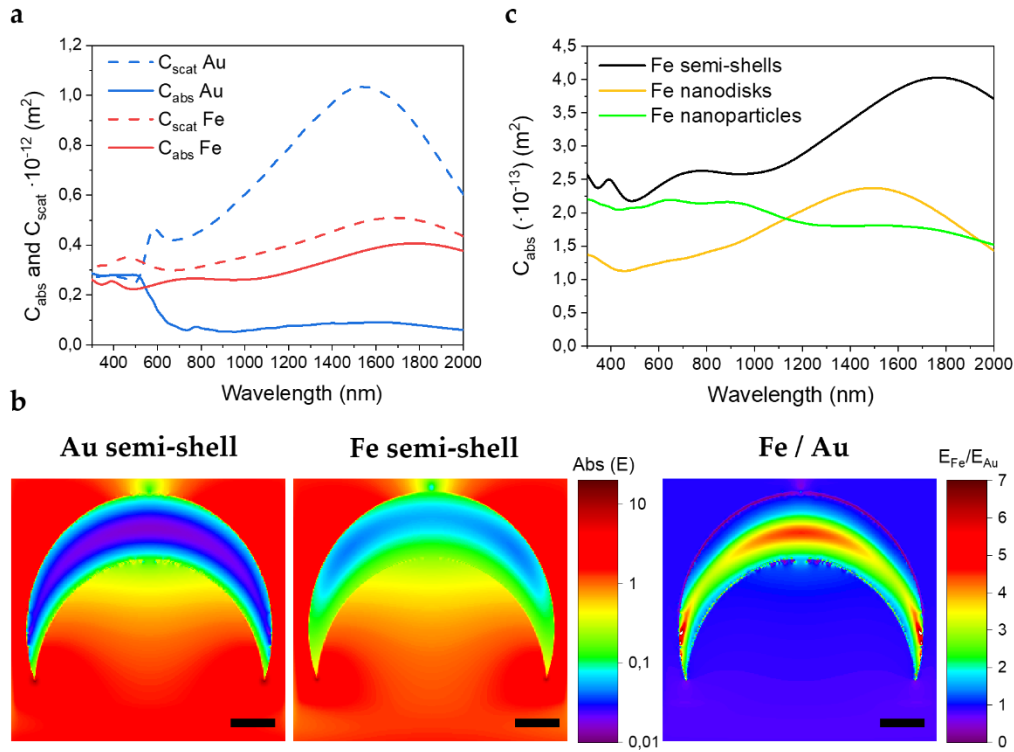
Figure 3-1. a) FDTD simulations comparing the scattering (C_{scat}) and absorption (C_{abs}) cross-sections for 500 nm diameter Au and Fe semi-shell structures. b) Electric field distribution in the central plane for Au (left) and Fe (centre) semi-shells and the ratio of the electric fields observed in each structure (right), evidencing the much larger light penetration inside the Fe structure. Scale-bar = 100 nm. c) Comparison of the C_{abs} for Fe structures of different shapes and constant size (diameter = 500 nm).
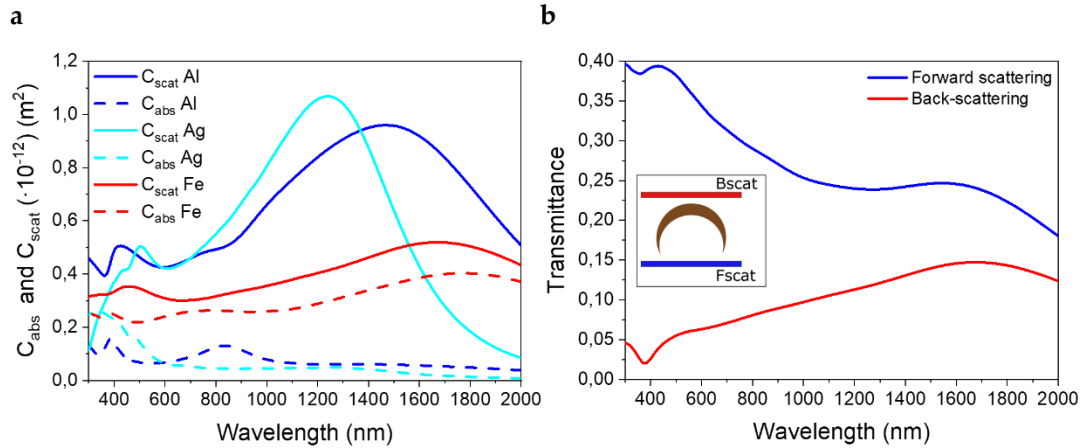
Figure 3-2. a) FDTD simulations of the scattering and absorption cross-section of aluminium (Al), silver (Ag) and Fe semi-shells of 500 nm diameter. b) Light transmittance through a perpendicular plane to the light propagation to show the forward (blue) and back scattering (red) of the Fe semi-shells. Inset picture: schematic representation of the simulation.

3.2.2. Metamaterial design and fabrication

Considering previous theoretical results, the fabrication process of the nanostructured-Fe/PDMS metamaterial is based on a scalable combination of colloidal self-assembly, physical vapour deposition and polymer casting (Figure 3a, see Appendix A for methodological details). The nanostructured-Fe film is prepared by the hexagonal close-packed self-assembly of a monolayer of polystyrene (PS) nanospheres (500 nm diameter) followed by the electron beam deposition of the Fe layer (80 nm), leading to a "semi-shell" structure[32,33]. The nanostructured-Fe film is mechanically coupled to the PDMS layer (50 μm) by transfer printing (Figure 3b). Once the metamaterial is fabricated, the generation of the optomechanical structures for soft actuation applications is performed by defining the desired geometries by laser writing and releasing them from the substrate, thus yielding free-standing structures. Note that the released structures have an initial curvature due to the generated residual stress during the releasing step. It is worth emphasizing that this fabrication process is straightforward, fast, inexpensive and easily scalable.
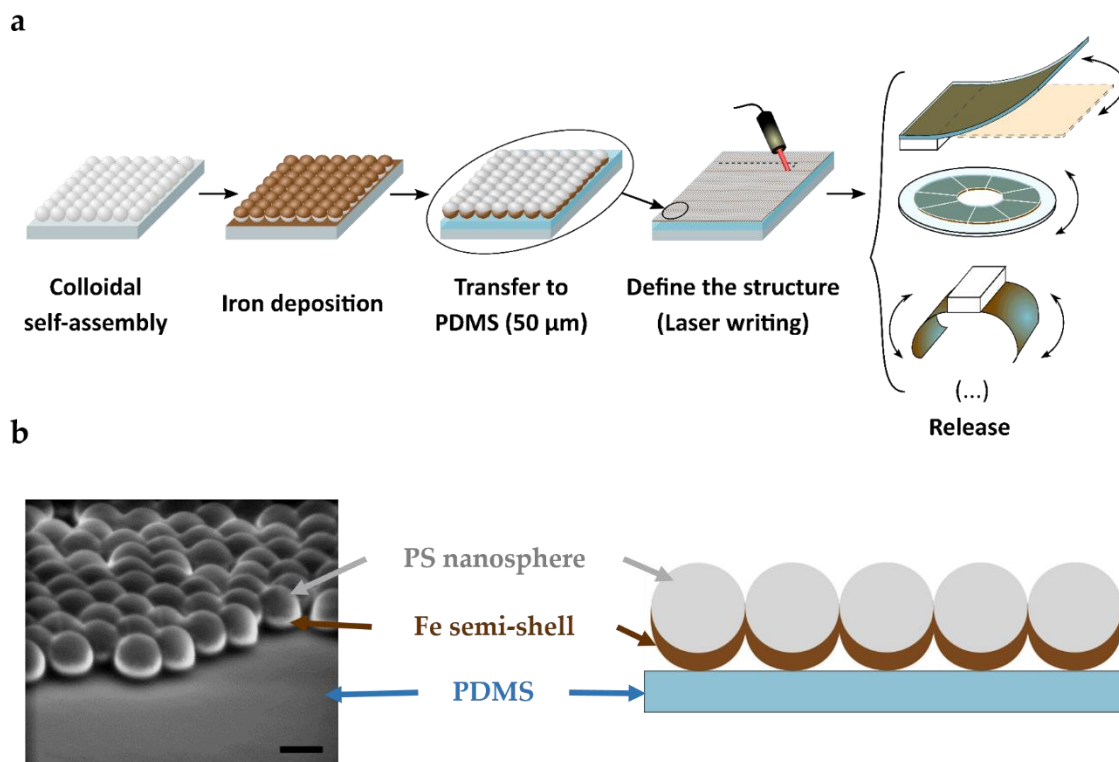
Figure 3-3. a) Schematic of the fabrication steps. b) SEM image and schematic representation of the nanostructured-Fe layer in contact to the PDMS layer (scale-bar = 500 nm).

3.2.3. Optical absorption and photothermal efficiency

In agreement with the FDTD simulations, the experimental characterization of the Fe/PDMS metamaterial demonstrated a very high optical absorption of the nanostructured-Fe layer within the Ultraviolet–Visible–Near Infrared (UV-vis-NIR) ranges (300 – 2000 nm) where the PDMS is transparent[34] (Figure 3-4a). Moreover, the nanostructured-Fe layer minimizes the reflectance in the MWIR and LWIR infrared regions (2000 - 18000 nm) (Figure 3-4c,d), thereby enabling the transmission and posterior absorption of these wavelengths by the PDMS layer, which is an efficient absorber in this range (Figure 3-4b). The synergistic combination of the optical properties of both layers results in an outstanding ultrabroadband absorption range from the UV to the LWIR, 300 – 18000 nm, with an average 84% absorption (Figure 3-4a,b). In comparison with previously reported strong (>80%) absorbers, the Fe/PDMS metamaterial shows a competitive absorption (from 75% to 94%) within a much broader wavelength range than any other reported absorber within the UV to LWIR range (Table 3-1). In contrast, the Au/PDMS metamaterial showed substantially weaker absorption (Figure 3-4a,b) because of the increased reflection of the nanostructured-Au (Figure 3-4c,d), as suggested by the FDTD simulations. The different performance between both metals is due to the highly damped plasmonic behaviour of Fe, which provides deeper electromagnetic field penetration inside the metal to maximize the absorption in the UV-vis-NIR (as previously show in Figure 3-1b), and the transmittance in the MWIR and LWIR. Oppositely, the nanostructured-Au layer behaves as a near-perfect

conductor in the NIR-LWIR, thereby enhancing the reflectance, thus decreasing even further the absorption efficiency. The superior absorption efficiency in the Fe/PDMS with respect to the Au/PDMS metamaterial was also observed for semi-shells of other diameters and different metal thicknesses (Figure 3-5). Note that by selecting the appropriate thickness of the Fe layer or the diameter of the nanostructures in the nanostructured-Fe layer, the minimum absorption of the metamaterial in the UV – NIR could be further enhanced to above 80% (Figure 3-5d).
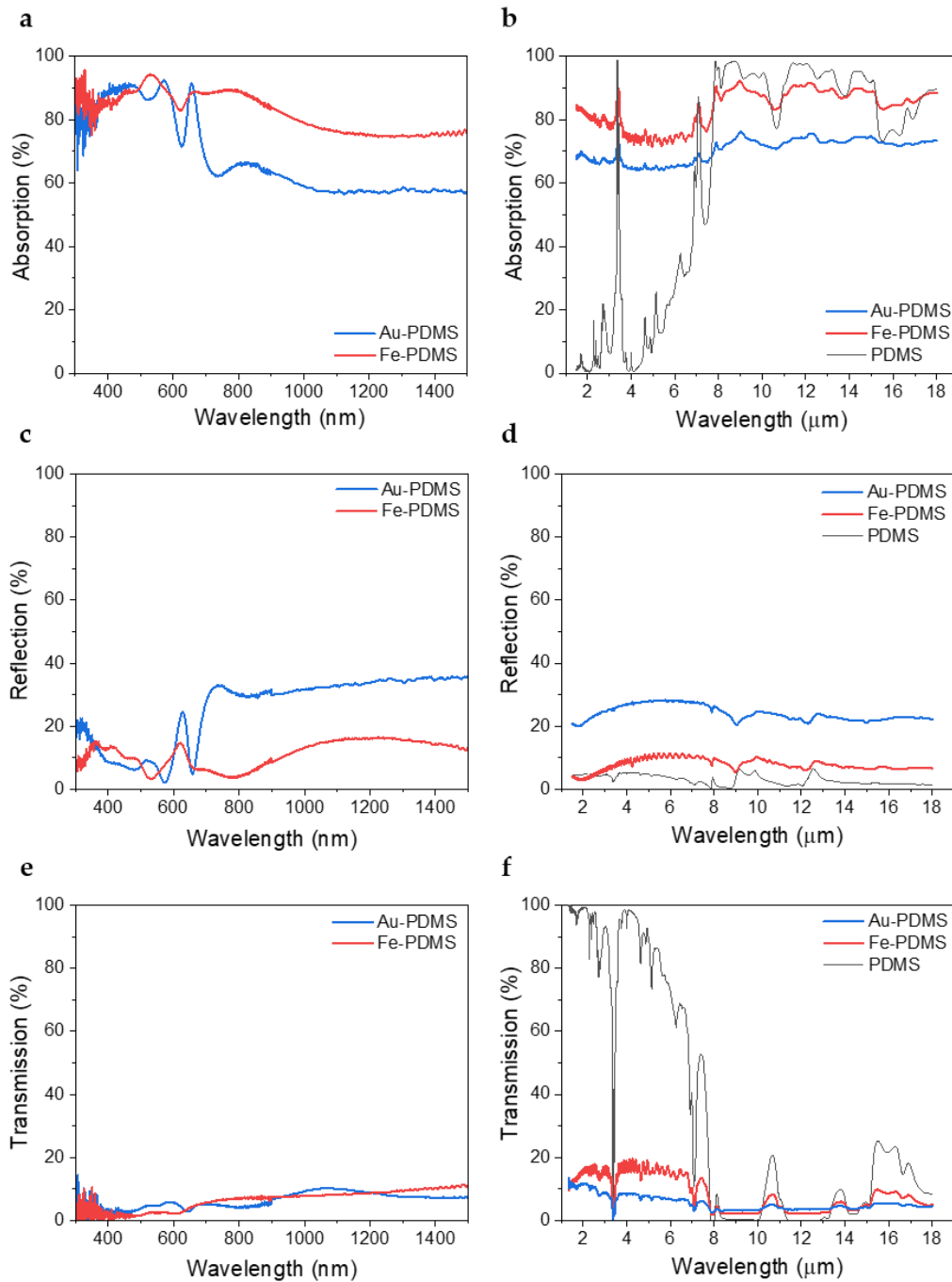
Figure 3-4. a) Absorption spectra of the Fe/PDMS- and Au/PDMS- metamaterials (a) in the UV-visible-NIR range, and (b) in the MWIR- LWIR range. c-d) UV-vis-NIR and MWIR-LWIR reflectance in the Fe/PDMS and Au/PDMS metamaterials. e-f) UV-vis-NIR and MWIR-LWIR transmittance in the Fe/PDMS and Au/PDMS metamaterials.

Material[†]	Absorption	Range (nm)
Nanostructured-Fe/PDMS	84%	300-18000
Graphene-based metamaterial[11]	85%	300-2500
TiN-SiO$_2$-ITO-Au Nanodisks[7]	98%	1400-1640
LbL TiN + PU Nanoparticles[10]	90%	300-2500
TiN Metamaterial[9]	95%	400-800
Al$_2$O$_3$+Au Collapsed Nanowires[35]	91%	400-2500
AlN – Au metasurface[36]	80%	18250-19750
Ag-SiO$_2$-Ag Trapezoidal nanowires[37]	85%	400-700
PEDOT-PDMS[22]	100%	750-1600
(MNLs/SiO$_2$)$_{x18}$ on Ag[38]	96%	300-1100
Cu/Si$_3$N$_4$/Cu stack[39]	80%	400-700
Ag/SiO$_2$ nanocomposite on Ag film[40]	95%	325-575
Au metasurface / SiO$_2$ / Au[12]	83%	370-880
ZnS/Au (gradient-metasurface-based absorber)*[41]	95%	5100-14100
Ti-SiO$_2$ cubes on Al*[42]	97%	354-1066
Ge$_2$Sb$_2$Te$_5$ / Au / SiO$_2$*[43]	92.9%	350-1500

Table 3-1. Comparison of ultrabroadband absorbers in the ultraviolet to far infrared range reported in the literature. "*" refers to theoretical studies.

[†] **Abbreviations:**

ITO = Indium Tin Oxide

LbL = Layer-by-Layer

PU = poly(urethane)

PEDOT = poly(3,4-ethylenedioxythiophene)

MNLs = Metallic Nanoparticle Layers
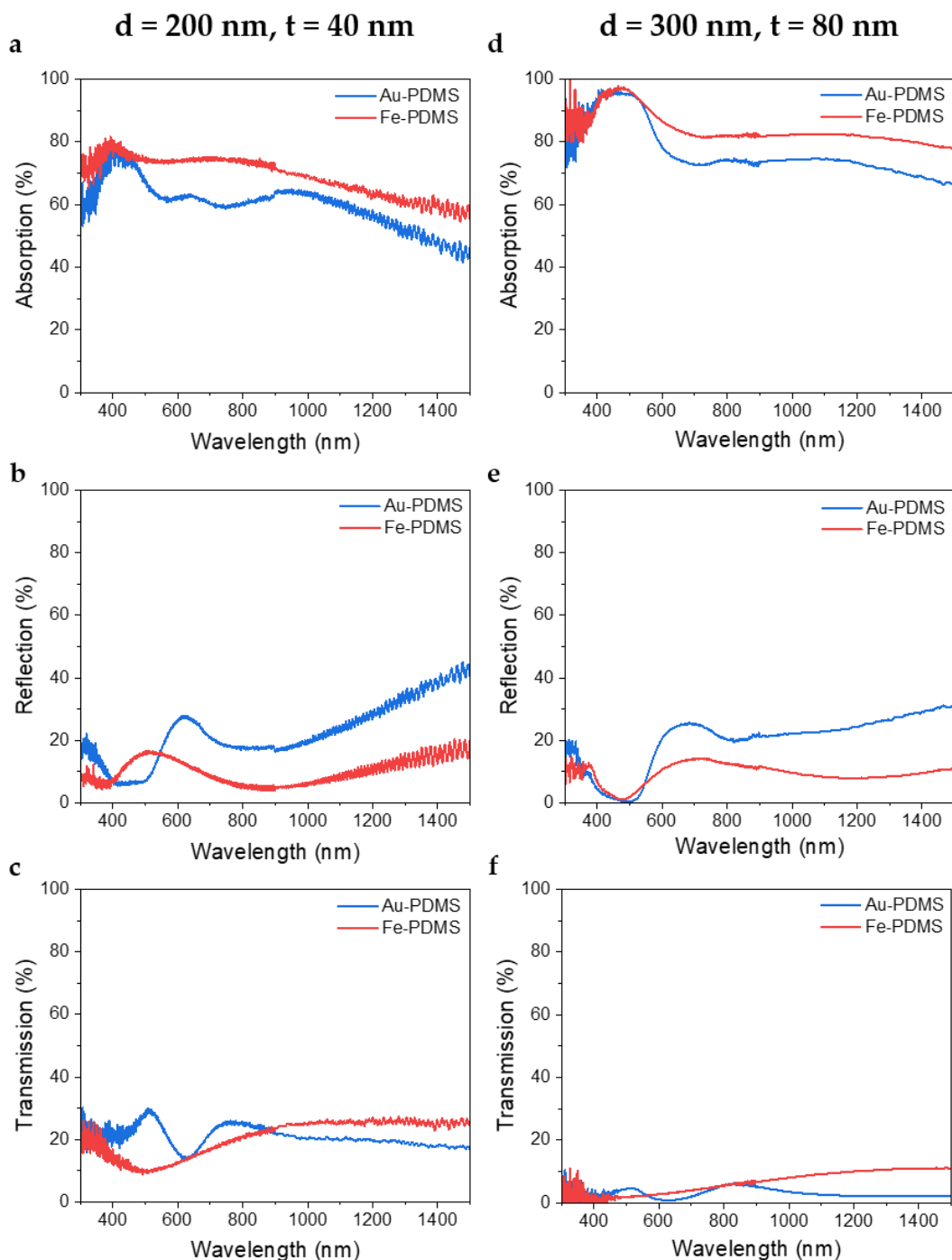
Figure 3-5. Optical properties of Au-PDMS and Fe-PDMS metamaterials with different diameters (d) of the polystyrene spheres and thickness (t) of the metal layer. a-b-c) Absorption, reflection and transmission spectra in the UV-vis-NIR for Fe/PDMS and Au/PDMS metamaterials with 200 nm polystyrene sphere diameter and 40 nm metal thickness. d-e-f) Absorption, reflection and transmission spectra in the UV-vis-NIR for Fe/PDMS and Au/PDMS metamaterials with 300 nm polystyrene sphere diameter and 80 nm metal thickness.

The photothermal conversion efficiency, $\eta = dT/dI$ (where T is temperature and I is the light irradiance), was determined by irradiating the metamaterials with four different light

sources: white-LED (410 – 700 nm), 808 nm and 1470 nm lasers, and natural sunlight. The change of temperature was found to be proportional to the light intensity for all the light sources (Fig. 3c). Moreover, the photothermal conversion efficiency of the Fe/PDMS-metamaterial did not significantly differ for any light source, which is in accordance with its nearly-flat broadband absorption. Importantly, the η of the Fe/PDMS-metamaterial exhibited minimal dependence on the light incidence angle, which is critical to provide a linear photo-thermo-mechanical response in structures with high curvatures, thus overcoming the angular limitation inherent to other absorbers[37,44]. As expected from the absorption spectra, the Fe/PDMS-metamaterial showed substantially higher η (ca. 2-fold) than the analogous Au/PDMS-metamaterial at normal incidence. Moreover, the nanostructured-Au layer presented strong angular dependence due to the diffraction-coupling to surface-plasmon-polaritons.
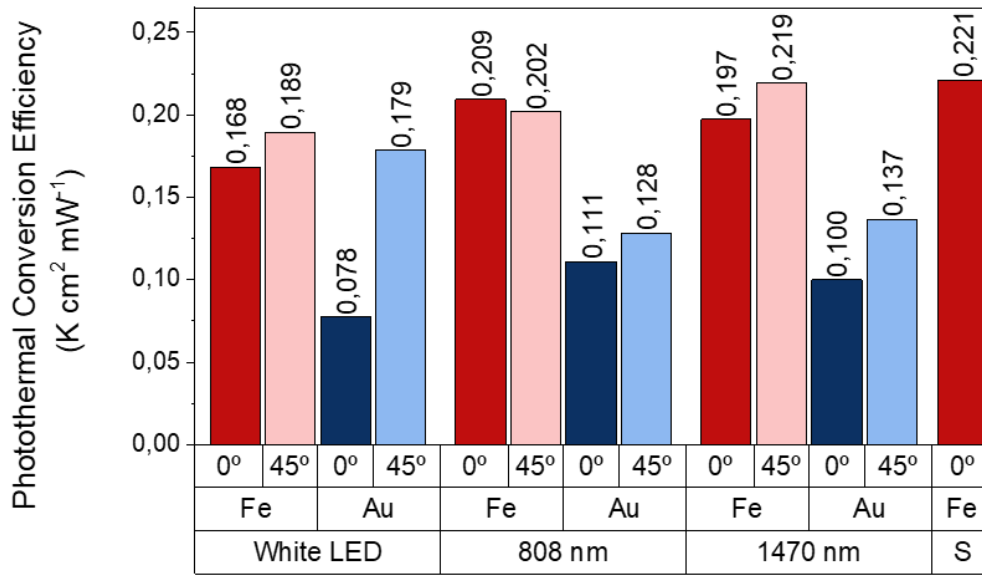
Figure 3-6. Photothermal conversion efficiency of the Fe/PDMS- and Au/PDMS-metamaterials for light sources of different emission wavelengths and incident angle ("S" = natural sunlight).

3.2.4. Optomechanical analysis

The optomechanical response was assessed in Fe/PDMS metamaterial cantilevers (Fig. 4a) by measuring the curvature changes as a function of the light intensity (Fig. 4b). In bimorph structures, the curvature change is produced by the thermal strain $\Delta\varepsilon$ generated by the light-induced temperature increase ΔT, $\Delta\varepsilon = (\alpha_{PDMS} - \alpha_{Fe})\Delta T$, where α_{PDMS} and α_{Fe} are the thermal expansion coefficients of PDMS and Fe, respectively. Since the PDMS layer thickness is much larger than the Fe layer ($t_{PDMS} \gg t_{Fe}$), the equation of the curvature ($1/r$) change can be simplified to[22]:

$$\frac{1}{r} = \frac{(\alpha_{\text{PDMS}} - \alpha_{\text{Fe}})\Delta T}{\dfrac{E_{\text{PDMS}}t_{\text{PDMS}}^2}{6E_{\text{Fe}}t_{\text{Fe}}} + \dfrac{2t_{\text{PDMS}}}{3}} \qquad (3\text{-}1)$$

Where r is the curvature radius (Fig. 4b, inset), and E_{PDMS} and E_{Fe} are the Young's-modulus of the nanostructured-Fe and PDMS layers, respectively.

The parameter "1/r" was chosen to quantify the curvature variations and to compare with the literature results, since it is independent of the cantilever length. The cantilever curvature changed linearly with the light-induced temperature changes, and therefore with the light intensity, showing a responsivity of 0.012 cm·mW^{-1}. The excellent photo-thermo-mechanical actuation of the Fe/PDMS-metamaterial is established by: i) the highly-efficient light absorption in an unprecedentedly broad spectral range to maximize the light-induced temperature changes, and ii) the large thermal expansion coefficient mismatch between both materials (α_{Fe} = 1.2·10^{-5} K^{-1}, α_{PDMS} = 3·10^{-4} K^{-1}). By fitting the experimental curvature to Eq. 1 (assuming t_{PDMS} = 50 μm, t_{Fe} = 80nm, E_{PDMS} = 1.4MPa, α_{Fe} = 1.2·10^{-5} K^{-1}, α_{PDMS}= 3·10^{-4} K^{-1}), the effective-Young's-modulus of the nanostructured-Fe layer was extracted, yielding 1.2 GPa. This value demonstrates that the nanostructured-Fe layer behaves as a continuous layer but with a substantially lower Young's-modulus than bulk-Fe (100-200 GPa), thereby highlighting its behaviour as both optical and mechanical metamaterial. Interestingly, due to large thickness difference between the Fe and the PDMS layers, the mechanical response of the bimorph Fe/PDMS-metamaterial mainly depends on the Young's-modulus and thickness of the PDMS. Therefore, its optical and mechanical responses can be independently tuned by: i) varying the thickness of the PDMS layer[45] and, ii) controlling the optical absorption of the metal layer by altering its thickness and/or morphology without substantially altering the mechanical response of the bimorph. Based on the experimental parameters, the expected responsivity enhancement by the reduction of the PDMS thickness can be estimated (Fig. 4c). Comparing to other bimorph actuators, the Fe/PDMS metamaterial presents a better responsivity than other actuators of similar thickness and the simulations predict that it could clearly surpass the responsivity of the reported actuators to date.
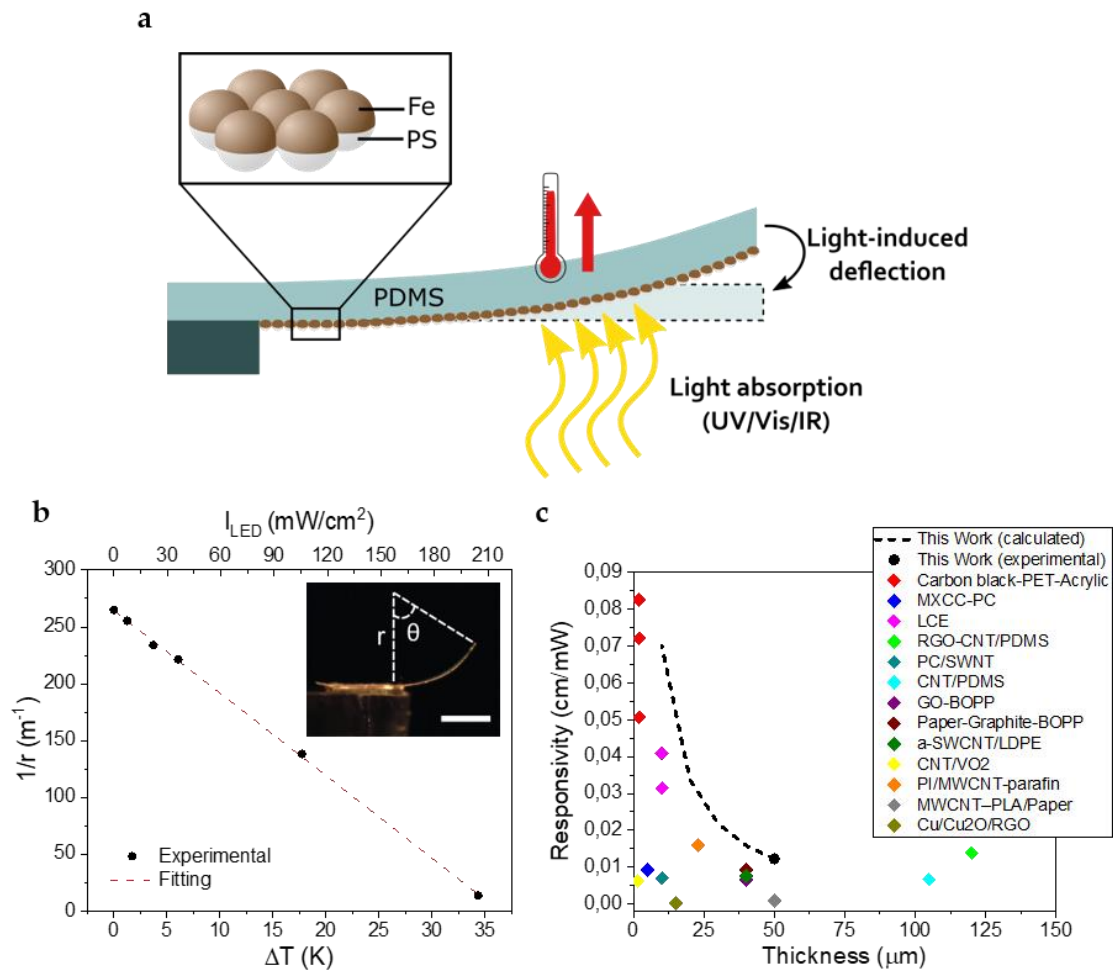
Figure 3-7. a) Schematic of the ultrabroadband optomechanical structure principle of operation. b) Curvature variation in response to light induced temperature changes (bottom) and associated white-LED irradiance (top). Inset: actual cantilever cross-view picture indicating the curvature radius/angle. Scale-bar = 2 mm. c) Comparison of the light-to-mechanical conversion efficiency of different photothermal bimorph actuators reported in the literature[21,23,30,31,38–47] (see Table 3-2 for the description of the different materials). The discontinuous black line shows the theoretical estimation of the response of the actuators described in this work by using other PDMS thicknesses.

Material[‡]	Length (cm)	Thickness (μm)	Light Irradiance (mW·cm^{-2})	Wavelength (nm)	1/r (cm^{-1})	Responsivity = r^{-1}/I (cm·mW^{-1})
Nanostructured-Fe/PDMS	0,4	50	204,5	White LED	2,51	0,0123
Carbon black-PET-Acrylic[21]	1	2	150	[760-2600 nm]	7,6	0,0507
			30	[White light]	2,5	0,0826
			30	[450 nm]	2,2	0,0721
MXCC-PC[23]	4	5	80	650-1050	0,7	0,0092
Dye DR1 mixed to LCE[30]	0,5	10	230	488	9,4	0,0410
			300			0,0314
RGO-CNT/PDMS[46]	2,4	120	250	artificial sunlight	3,5	0,0139
PC/SWNT[31]	2,5	10	20	White Light	0,1	0,0070

[‡]**Abbreviations:**
PET = Polyethylene terephthalate
MXCC = MXene(Ti$_3$C$_2$T$_x$)-cellulose composites and polycarbonate membrane
PC = Polycarbonate
LCE = Liquid Crystal Elastomer
RGO = Reduced Graphene Oxide
CNT = Carbon Nanotubes
SWNT = Single Wall carbon Nanotubes
BOPP = Biaxially oriented polypropylene
(a)-SWCNT = (acidized)-Single Wall Carbon Nanotubes
LDPE = Low Density Polyethylene
PI = PolyImide
MWCNT = Multi Wall Carbon Nanotubes
PLA = Polylactic Acid

CNT/ PDMS[47]	2,1	105	250	artificial sunlight	1,7	0,0066
GO- BOPP[48]	1,5	40	300	NIR	2,0	0,0067
Paper- Graphite- BOPP[49]	4	40	300	NIR	2,8	0,0093
a- SWCNT/ LDPE[50]	4	40	250	NIR	1,9	0,0076
CNT/ VO$_2$[51]	-	1,5	800	[not specified]	5,0	0,0063
PI/ MWCNT- parafin[52]	2	23	100	artificial sunlight	1,6	0,0160
MWCNT- PLA/ Paper[53]	6	50	275	NIR	0,2	0,0009
Cu/Cu$_2$O/ RGO[54]	4	15	1000	IR	0,17	0,00017

Table 3-2. Detailed data of the comparison of the light-to-mechanical conversion efficiency of the different photothermal bimorph actuators described in Figure 3-7d.

3.2.5. Soft Optomechanical Devices

To exploit the excellent optomechanical responsivity of the Fe/PDMS metamaterial, the application of this metamaterial into different light-controlled devices is explored. Specifically, i) a self-regulating artificial iris, ii) a light-regulated soft-robotic gripper and iii) a remotely optically-triggered electrical switch are designed.

Firstly, a self-regulated iris mimicking the behaviour of the human iris is developed. A power-free, self-regulated iris might be a solution to ophthalmological problems related to the size and dynamics of the pupil/iris, by controlling the amount of light that reaches the retina[55]. In addition, the same design can be used for an automatic light transmission control (i.e., an optical attenuator for light protection) of any source emitting in the 300 nm to 18000 nm range. Note that our iris design was geometrically inspired by a previously reported artificial iris based on liquid crystal elastomers (LCE)[30] working in the 400-600 nm range.

Using the standard dimensions of a natural iris[56], the device consisted of a circular Fe/PDMS membrane fixed at its outer diameter (11 mm) with an inner circular hole of 3 mm. The circular membrane was divided into 8 segments presenting an initial curvature of 108 ± 6 degrees (Figure 3-8), which automatically folded/unfolded depending on the incoming light intensity, thereby opening/closing the inner aperture (Figure 3-9a). The biomimetic optomechanical response was characterized by measuring the inner circle diameter of the iris (i.e., the pupil size) as a function of the incoming light irradiance from a white-LED (Figure 3-9b). The iris responded linearly to the light irradiance, reaching the nearly closed configuration with 234 mW·cm^{-2}, which corresponds to 1.7-sun intensity[57]. This system was capable of self-adjusting the pupil aperture diameter from 6.9 to 3.8 mm, which is comparable to the standard dynamic range of a natural pupil. The transmitted power through the iris (Figure 3-9b, red-line) showed a linear self-regulation reaching a relative transmitted power of 56% in the nearly closed configuration, which approximately corresponded to the relative area variation of the pupil. This transmission range can be readily tuned by adjusting the inner hole diameter.
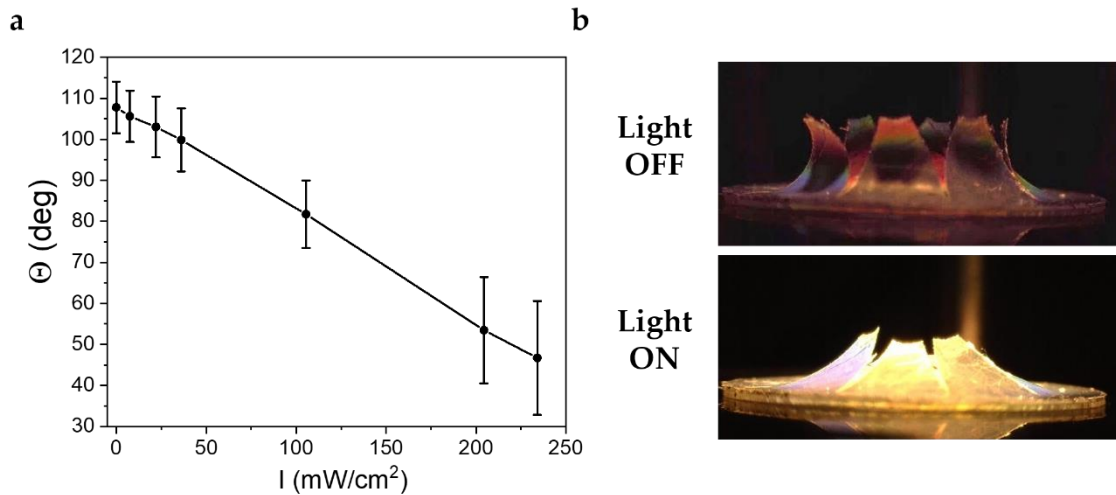
Figure 3-8. a) Average angle change of the segments of the artificial iris as a function of light intensity. b) Side-view image of the artificial iris upon white light actuation.
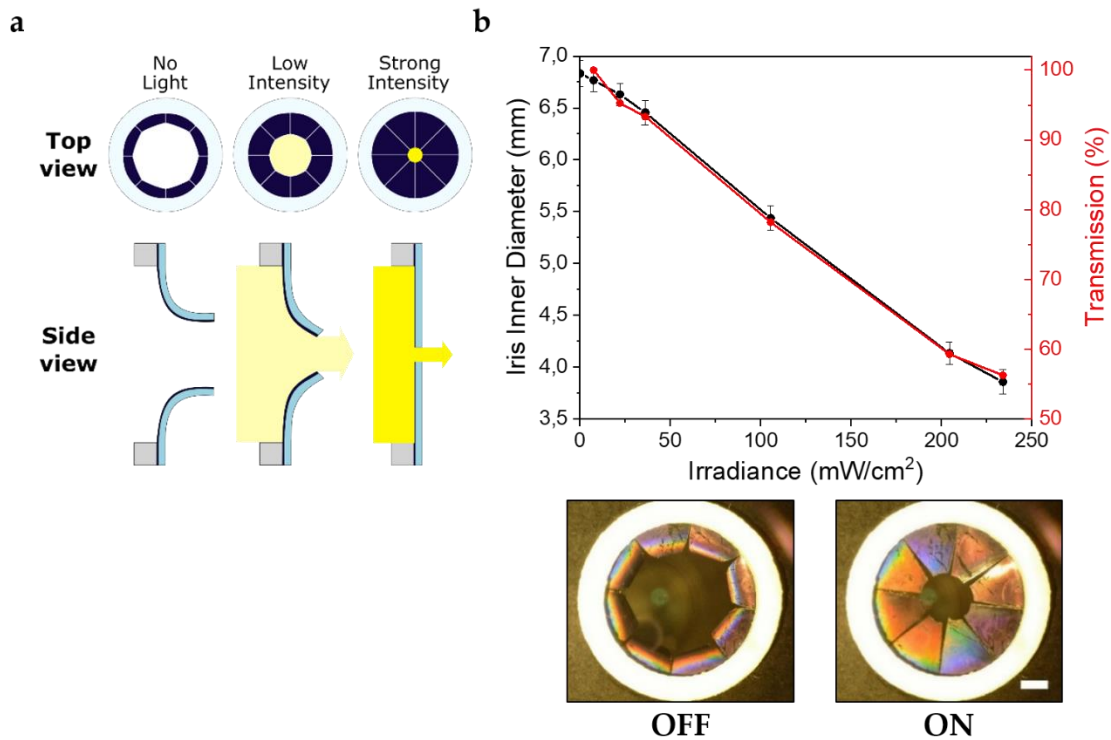
Figure 3-9. a) Schematic of the artificial iris working principle. b) Closure of the iris aperture upon white-LED irradiation with increasing irradiance (black circles) and related fraction of the transmitted light power (red circles), together with the actual pictures of the artificial iris with/without white-LED illumination (irradiance 234 mW·cm⁻²). Scale-bar = 2 mm.

To show the ultrabroadband self-regulation of the iris, its responsivity was analysed, i.e., the variation of the pupil diameter as a function of the incident intensity, for light sources with emission from the visible to the LWIR (Figure 3-10a,b), including the white-LED (Figure 3-9b), sunlight, an 808 nm laser (Figure 3-10a), and an infrared thermal emitter. Although the wavelength distribution of the white-LED and the natural sunlight are different, their responsivity was nearly equal due to the flat broadband absorption of the Fe/PDMS metamaterial that minimized any wavelength dependence. As observed in Figure 3-10b, the iris also responded with similar responsivity to the illumination with monochromatic near-infrared light from the 808 nm laser. Remarkably, the iris also exhibited self-regulation at the MWIR-LWIR range, which was demonstrated by its response to the weak emission from a material heated from room temperature to 120°C, in which the blackbody radiation wavelength peaks at 7500 nm (Figure 3-11a). To rule out any contribution from the temperature increase of the air surrounding the iris, two samples of very different emissivity (ε), PDMS (ε = 0.86) and aluminium (ε = 0.04), were heated at the same temperature (Figure 3-11b). The iris diameter was reduced a 9 % for the PDMS good-emitter, while it barely changed for the Al poor-emitter. Considering the low thermal irradiance at the iris (29,7 mW·cm⁻²), the responsivity to the thermal IR light was even higher than the other light sources, due to the increased absorption efficiency of the Fe/PDMS metamaterial in the MWIR-LWIR range. Additionally, the temperature increase at the iris upon direct sunlight irradiation was 14.3 °C (Figure 3-10c), which was enough to actuate

the optomechanical system, and reasonably low to be easily insulated and safe for biomedical applications.
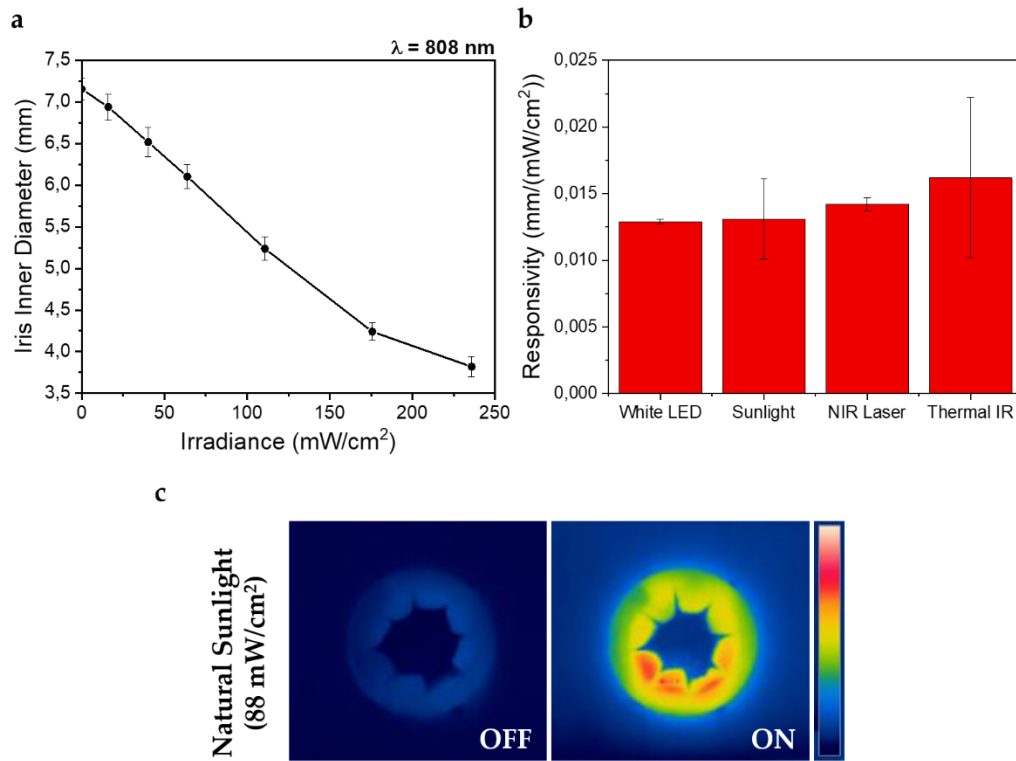
Figure 3-10. a) Optomechanical response of the iris as a function of light intensity at wavelength = 808 nm. b) Ultrabroadband iris responsivity to different light sources with emission from the visible to the LWIR. c) Thermograph of the artificial iris being actuated by natural sunlight. Temperature scale = 25-45ºC.
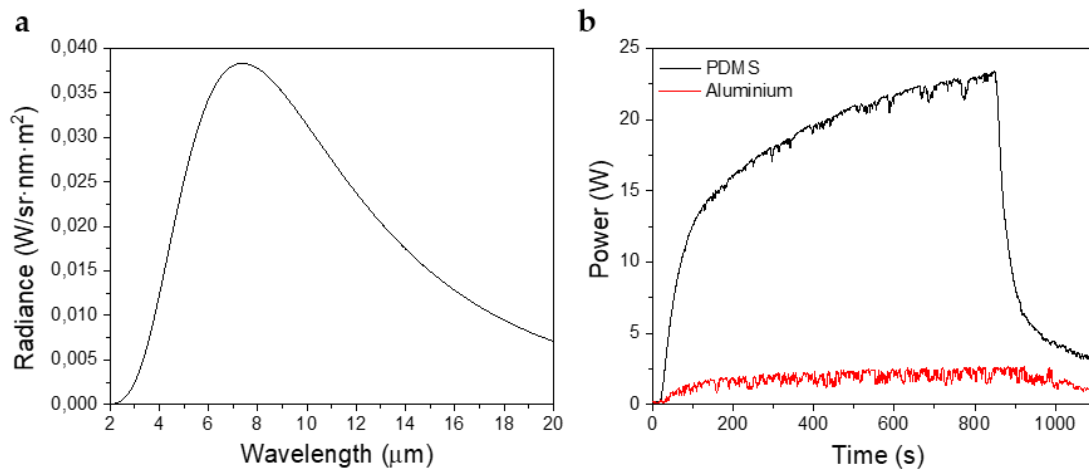
Figure 3-11. a) Blackbody radiation spectrum at T = 120ºC, $\varepsilon = 1$. b) Light emission power of PDMS and aluminium samples during heating (and cooling) from 25ºC to 120ºC.

Finally, the dynamic response of the biomimetic iris was tested during an on-off cycle using the white-LED (Figure 3-12a) and the 808 nm laser (Figure 3-12b). In both cases, the aperture abruptly changed during the initial 4 seconds, followed by a slower thermal stabilization

during 10 seconds. Once the light was switched off, the iris returned to the initial position. The transmitted power during the same on-off cycle showed similar dynamic response as the iris diameter. The reaction time was slightly slower than the human iris[58], but it could be matched by optimization of the metamaterial stiffness or geometry. Notably, compared to the previously reported self-regulating artificial iris based on LCE[30], our device presents several advantages, such as a faster and more homogeneous response to small light intensities and a much broader spectral response range. However, it could be of great interest to combine the control on the thermo-mechanical response of LCEs with the ultrabroadband absorber metamaterial presented in this thesis.
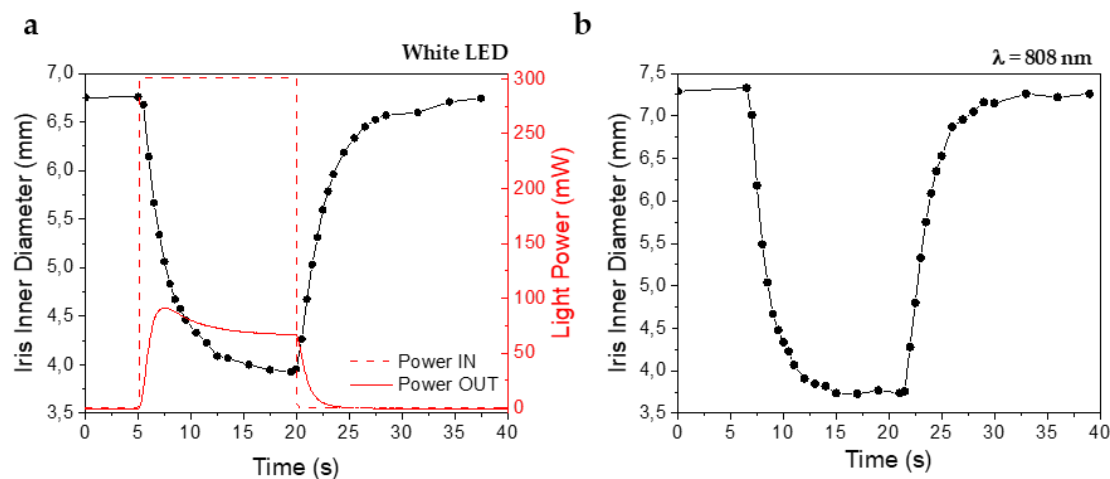
Figure 3-12. a) Dynamic response of the artificial iris to white LED (I = 234 mW·cm^{-2}) and b) NIR laser (λ = 808 nm, I = 236 mW·cm^{-2})

To show the versatility of the Fe/PDMS optomechanical metamaterial, a simple soft mechanic gripper[21] was also developed, consisting of two cantilevers facing each other (Figure 3-13a). In its relaxed state, the initial bending due to the residual stress configures the gripper in its closed state (step 1). When the gripper is irradiated (step 2), its arms open making it possible to encase the cargo (step 3). As the light irradiation stops, the gripper closes and clutches the cargo, which can be then transported to a different position (steps 4-7). To release the cargo, the gripper can be opened again by light irradiation (steps 8-9). It is worth highlighting the gripper loading capacity, as the cargo weight was remarkably higher (54 mg) than the actuator itself (1 mg). Moreover, the clutching force of the actuator, which depends on the initial stress, can be adjusted by tuning the actuators' length and by controlling residual stress in the fabrication process. On the other hand, the opening strength and velocity can be controlled by the incident light intensity.

Finally, the Fe/PDMS actuator was tested as a remote optically-triggered electrical switch. In this approach, the optically-controlled bending of the actuator is exploited to open/close an electrical circuit and turn off/on a LED (Figure 3-13b). Since the nanostructured-Fe/PDMS is not conductive, a thin layer of conductive silver paste was applied on the edge of the structure. Even though the actuator's performance was slightly altered due to its weight and stiffness increase, the photo-thermo-mechanical forces were sufficiently strong

to bend the free-standing structure and close the electrical circuit. However, in future demonstrations, the incorporation of a conductive pad could be optimized using more sophisticated micropatterning techniques such as inkjet-printing, thus opening the path to light-controlled electrical switches for energy efficiency systems.
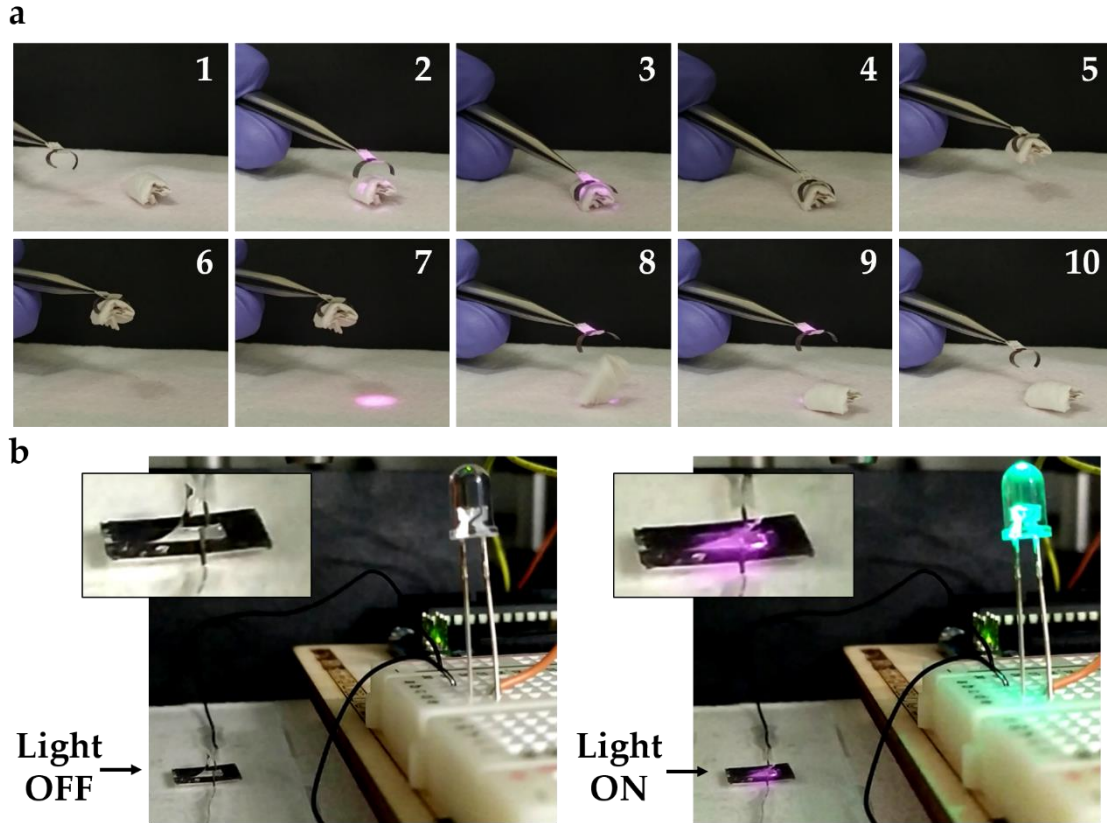
Figure 3-13. a) Pictures of the optically controlled mechanical gripper showing the opening, clutching, transport and release of the cargo. b) Pictures of the light-triggered electrical switch. The inset pictures show the optomechanical actuator that open/closes the electrical circuit and turns on the LED. The incident light (λ = 808 nm) irradiance in (a) and (b) is 242 mW·cm^{-2}.

3.3. CONCLUSIONS

In summary, a novel flexible ultrabroadband absorbing nanostructured-Fe/PDMS metamaterial is presented. The optical synergy between the highly damped plasmonic behaviour in the nanostructured-Fe layer and the efficient IR absorption in the PDMS enables achieving angle-independent and strong (average 84%) ultrabroadband absorption from the UV to LWIR (300 - 18000 nm), thus overcoming the limitations of typical plasmonic absorbers and multi-layered systems. The angle-independent optical absorption in a large wavelength range translates to an excellent photothermal conversion efficiency. This, combined with the large thermal expansion mismatch between Fe and PDMS, provides an outstanding optomechanical response in suspended structures made of this metamaterial. To exploit these unique features, a self-regulated biomimetic iris capable of responding to an ultrabroadband wavelength range is demonstrated, including natural sunlight and IR

thermal radiation. The iris reversibly changes its aperture size following the same dimensions of a natural pupil, and achieves fast, efficient, homogeneous and linear optomechanical regulation of the transmitted power. Furthermore, the versatile applicability of the metamaterial is shown by developing a light-controlled soft mechanical gripper and a light-triggered electrical switch. Overall, the exceptional photo-thermo-mechanical properties and the versatility and cost-effectiveness of this metamaterial bring new opportunities to develop different types optomechanical components, such as dynamic prosthetics, self-regulated and power free light protectors (at any wavelength from UV to LWIR) or light-controlled soft-robots. Furthermore, its ultrabroadband absorption could be exploited in other fields where light collection is crucial, as thermophotovoltaics or photodetection.

3.4.   REFERENCES

1. Liu, Q. *et al.* Inverse optical cavity design for ultrabroadband light absorption beyond the conventional limit in low-bandgap nonfullerene acceptor–based solar cells. *Adv. Energy Mater.* **9**, 1900463 (2019).

2. Wang, Y. *et al.* Metamaterial-plasmonic absorber structure for high efficiency amorphous silicon solar cells. *Nano Lett.* **12**, 440–445 (2012).

3. Yuan, H. *et al.* Polarization-sensitive broadband photodetector using a black phosphorus vertical p–n junction. *Nat. Nanotech.* **10**, 707–713 (2015).

4. Fang, H. *et al.* Self-powered ultrabroadband photodetector monolithically integrated on a PMN–PT ferroelectric single crystal. *ACS Appl. Mater. Interfaces* **8**, 32934–32939 (2016).

5. Kim, J. U., Lee, S., Ji Kang, S. & Kim, T. Materials and design of nanostructured broadband light absorbers for advanced light-to-heat conversion. *Nanoscale* **10**, 21555–21574 (2018).

6. Yu, P. *et al.* Broadband metamaterial absorbers. *Adv. Opt. Mater.* **7**, 1800995 (2019).

7. Hendrickson, J. R. *et al.* Coupling of epsilon-near-zero mode to gap plasmon mode for flat-top wideband perfect light absorption. *ACS Photonics* **5**, 776–781 (2018).

8. Cui, Y. *et al.* Ultrabroadband light absorption by a sawtooth anisotropic metamaterial slab. *Nano Lett.* **12**, 1443–1447 (2012).

9. Li, W. *et al.* Refractory plasmonics with titanium nitride: broadband metamaterial absorber. *Adv. Mater.* **26**, 7959–7965 (2014).

10. Li, M. *et al.* Plasmonic biomimetic nanocomposite with spontaneous subwavelength structuring as broadband absorbers. *ACS Energy Lett.* **3**, 1578–1583 (2018).

11. Lin, H. *et al.* A 90-nm-thick graphene metamaterial for strong and extremely broadband absorption of unpolarized light. *Nat. Photon.* **13**, 270–276 (2019).

12. Liu, Z. *et al.* Ultra-broadband tunable resonant light trapping in a two-dimensional randomly microstructured plasmonic-photonic absorber. *Sci. Rep.* **7**, 43803 (2017).

13. Zhang, H., Feng, L., Liang, Y. & Xu, T. An ultra-flexible plasmonic metamaterial film for efficient omnidirectional and broadband optical absorption. *Nanoscale* **11**, 437–443 (2019).

14. Yu, P. *et al.* Effects of plasmonic metal core-dielectric shell nanoparticles on the broadband light absorption enhancement in thin film solar cells. *Sci. Rep.* **7**, 7696 (2017).

15. Matsumori, K. & Fujimura, R. Broadband light absorption of an Al semishell-MIM nanostructure in the UV to near-infrared regions. *Opt. Lett.* **43**, 2981–2984 (2018).

16. Takatori, K., Okamoto, T. & Ishibashi, K. Surface-plasmon-induced ultra-broadband light absorber operating in the visible to infrared range. *Opt. Express* **26**, 1342–1350 (2018).

17. Mendes, M. J., Morawiec, S., Simone, F., Priolo, F. & Crupi, I. Colloidal plasmonic back reflectors for light trapping in solar cells. *Nanoscale* **6**, 4796–4805 (2014).

18. Liu, Z. *et al.* Automatically acquired broadband plasmonic-metamaterial black absorber during the metallic film-formation. *ACS Appl. Mater. Interfaces* **7**, 4962–4968 (2015).

19. Liu, D. *et al.* Black Gold: Plasmonic colloidosomes with broadband absorption self-assembled from monodispersed gold nanospheres by using a reverse emulsion system. *Angew. Chem. Int. Edit.* **54**, 9596–9600 (2015).

20. Sepúlveda, B., Angelomé, P. C., Lechuga, L. M. & Liz-Marzán, L. M. LSPR-based nanobiosensors. *Nano Today* **4**, 244–251 (2009).

21. Li, J. *et al.* Photothermal bimorph actuators with in-built cooler for light mills, frequency switches, and soft robots. *Adv. Funct. Mater.* **29**, 1808995 (2019).

22. Lim, H. *et al.* Construction of a photothermal Venus flytrap from conductive polymer bimorphs. *NPG Asia Mater.* **9**, e399 (2017).

23. Cai, G., Ciou, J.-H., Liu, Y., Jiang, Y. & Lee, P. S. Leaf-inspired multiresponsive MXene-based actuator for programmable smart devices. *Sci. Adv.* **5**, eaaw7956 (2019).

24. Pilz da Cunha, M. *et al.* An Untethered magnetic- and light-responsive rotary gripper: shedding light on photoresponsive liquid crystal actuators. *Adv. Opt. Mater.* **7**, 1801643 (2019).

25. Mirvakili, S. M. & Hunter, I. W. Artificial muscles: mechanisms, applications, and challenges. *Adv. Mater.* **30**, 1704407 (2018).

26. Wang, X.-Q. *et al.* In-built thermo-mechanical cooperative feedback mechanism for self-propelled multimodal locomotion and electricity generation. *Nat. Commun.* **9**, 3438 (2018).

27. Li, C., Liu, Y., Huang, X. & Jiang, H. Direct sun-driven artificial heliotropism for solar energy harvesting based on a photo-thermomechanical liquid-crystal elastomer nanocomposite. *Adv. Funct. Mater.* **22**, 5166–5174 (2012).

28. Yu, L. & Yu, H. Light-powered tumbler movement of graphene oxide/polymer nanocomposites. *ACS Appl. Mater. Interfaces* **7**, 3834–3839 (2015).

29. Leeladhar, Raturi, P. & Singh, J. P. Sunlight-driven eco-friendly smart curtain based on infrared responsive graphene oxide-polymer photoactuators. *Sci. Rep.* **8**, 3687 (2018).

30. Zeng, H., Wani, O. M., Wasylczyk, P., Kaczmarek, R. & Priimagi, A. Self-regulating iris based on light-actuated liquid crystal elastomer. *Adv. Mater.* **29**, 1701814 (2017).

31. Zhang, X. *et al.* Photoactuators and motors based on carbon nanotubes with selective chirality distributions. *Nat. Commun.* **5**, 2983 (2014).

32. Li, Z. *et al.* Simultaneous local heating/thermometry based on plasmonic magnetochromic nanoheaters. *Small* **14**, 1800868 (2018).

33. Li, Z. *et al.* Magnetically amplified photothermal therapies and multimodal imaging with magneto-plasmonic nanodomes. *Appl. Mater. Today* **12**, 430–440 (2018).

34. Stankova, N. E. *et al.* Optical properties of polydimethylsiloxane (PDMS) during nanosecond laser processing. *Appl. Surf. Sci.* **374**, 96–103 (2016).

35. Bae, K. *et al.* Flexible thin-film black gold membranes with ultrabroadband plasmonic nanofocusing for efficient solar vapour generation. *Nat. Commun.* **6**, 10103 (2015).

36. Hui, Y., Gomez-Diaz, J. S., Qian, Z., Alù, A. & Rinaldi, M. Plasmonic piezoelectric nanomechanical resonator for spectrally selective infrared sensing. *Nat. Commun.* **7**, 11249 (2016).

37. Aydin, K., Ferry, V. E., Briggs, R. M. & Atwater, H. A. Broadband polarization-independent resonant light absorption using ultrathin plasmonic super absorbers. *Nat. Commun.* **2**, 517 (2011).

38. Ji, T. *et al.* Plasmonic broadband absorber by stacking multiple metallic nanoparticle layers. *Appl. Phys. Lett.* **106**, 161107 (2015).

39. Zhu, P. & Jay Guo, L. High performance broadband absorber in the visible band by engineered dispersion and geometry of a metal-dielectric-metal stack. *Appl. Phys. Lett.* **101**, 241116 (2012).

40. Hedayati, M. K., Zillohu, A. U., Strunskus, T., Faupel, F. & Elbahri, M. Plasmonic tunable metamaterial absorber as ultraviolet protection film. *Appl. Phys. Lett.* **104**, 041103 (2014).

41. Guo, W., Liu, Y. & Han, T. Ultra-broadband infrared metasurface absorber. *Opt. Express* **24**, 20586–20592 (2016).

42. Lei, L., Li, S., Huang, H., Tao, K. & Xu, P. Ultra-broadband absorber from visible to near-infrared using plasmonic metamaterial. *Opt. Express* **26**, 5686–5693 (2018).

43. Tian, X. & Li, Z.-Y. Visible-near infrared ultra-broadband polarization-independent metamaterial perfect absorber involving phase-change materials. *Photon. Res.* **4**, 146–152 (2016).

44. Popov, E. *et al.* Total absorption of unpolarized light by crossed gratings. *Opt. Express* **16**, 6146–6155 (2008).

45. Mata, A., Fleischman, A. J. & Roy, S. Characterization of polydimethylsiloxane (PDMS) properties for biomedical micro/Nanosystems. *Biomed. Microdevices* **7**, 281–293 (2005).

46. Hu, Y. *et al.* A graphene-based bimorph structure for design of high performance photoactuators. *Adv. Mater.* **27**, 7867–7873 (2015).

47. Hu, Y. *et al.* Electrically and sunlight-driven actuator with versatile biomimetic motions based on rolled carbon nanotube bilayer composite. *Adv. Funct. Mater.* **27**, 1704388 (2017).

48. Chen, L. *et al.* Multi-responsive actuators based on a graphene oxide composite: intelligent robot and bioinspired applications. *Nanoscale* **9**, 9825–9833 (2017).

49. Weng, M. *et al.* Multiresponsive bidirectional bending actuators fabricated by a pencil-on-paper method. *Adv. Funct. Mater.* **26**, 7244–7253 (2016).

50. Li, L. *et al.* Dual-mechanism and multimotion soft actuators based on commercial plastic film. *ACS Appl. Mater. Interfaces* **10**, 15122–15128 (2018).

51. Ma, H. *et al.* Flexible, All-inorganic actuators based on vanadium dioxide and carbon nanotube bimorphs. *Nano Lett.* **17**, 421–428 (2017).

52. Zhou, P., Chen, L., Yao, L., Weng, M. & Zhang, W. Humidity- and light-driven actuators based on carbon nanotube-coated paper and polymer composite. *Nanoscale* **10**, 8422–8427 (2018).

53. Hua, D. *et al.* 3D printing of shape changing composites for constructing flexible paper-based photothermal bilayer actuators. *J. Mater. Chem. C* **6**, 2123–2131 (2018).

54. Meng, J. *et al.* A flexible metallic actuator using reduced graphene oxide as a multifunctional component. *Nanoscale* **9**, 12963–12968 (2017).

55. Koch, K. R., Heindl, L. M., Cursiefen, C. & Koch, H.-R. Artificial iris devices: benefits, limitations, and management of complications. *J. Cataract Refract. Surg.* **40**, 376–382 (2014).

56. Thainimit, S., Alexandre, L. A. & de Almeida, V. M. N. Iris surface deformation and normalization. in *2013 13th International Symposium on Communications and Information Technologies (ISCIT)* 501–506 (2013).

57. Gueymard, C. A. The sun's total and spectral irradiance for solar energy applications and solar radiation models. *Sol. Energy* **76**, 423–453 (2004).

58. Gradle, H. S. & Ackerman, W. The reaction time of the normal pupil: second communication. *JAMA* **99**, 1334–1336 (1932).

4. Untethered opto-magnetic soft actuator with integrated mechanochromic self-sensing

The development of untethered multi-stimuli responsive materials is a topic of considerable interest for smart soft robotics applications, especially those enabling remote actuation and versatile operation in inaccessible environments. In parallel, the incorporation of self-sensing mechanisms to quantify the external stimulation in real time are crucial for the development of automated systems. Here, an untethered sensing and actuation platform based on a soft opto-magnetic actuator with an integrated mechanochromic feedback system is presented. The device, based on the nanostructured-Fe/PDMS presented in Chapter 3, applied to a mechanical structure with a periodically corrugated backside, can be actuated both (i) optically in a broadband wavelength range within the infrared (IR) spectrum and (ii) magnetically by adjusting the magnetic field strength and direction. The mechanical status of the structure is easily visualized and quantified from the changes in structural coloration generated at its grooved back surface by measuring the Hue value in the pixels of the images taken by a conventional RGB camera or a smartphone camera. The optical and magnetic actuation self-sensing is demonstrated, having a detection limit of 1.8 mW·cm^{-2} and 0.34 mT, respectively. The easy operation and versatility of this system, such as the untethered single or simultaneous opto-magnetic actuation and the mechanochromic self-detection, paves the way to a new generation of wireless soft robotics and smart systems.

4.1. INTRODUCTION

Soft actuators and stimuli-responsive materials are attracting increasing attention in soft robotics, artificial muscles, wearables and biomimetic devices[1–3] due to their ability to deform and adapt to different environments with high resiliency. In these systems, the capacity of remote actuation by untethered stimuli, such as light or magnetic fields, can prevent the need of wiring and electrical contacts, thereby greatly reducing the complexity of the actuators and enabling its operation in hazardous environments or not accessible spaces. Both optical and magnetic actuators have been extensively studied, however, each of them faces its own challenges and limitations[4]. The optical actuation of soft-robots[5–7] is usually based on photo-thermo-mechanical effects, in which the absorbed light is converted into heat to generate the mechanical actuation. Hence, many efforts are currently devoted to develop efficient, broadband light absorbers that can be implemented into soft mechanical structures[8,9] (see Chapter 3 for more details). However, light-triggered actuation is limited by the slow cooling processes after actuation and to environments that are transparent to the actuating light. Soft magnetic actuators provide an interesting alternative to light-mediated actuation due to their ability to perform robust and programmable shape changes[10], and precise manipulation of the structures[11] over long distances or through opaque media, which are very attractive for biomedical applications[12,13]. However, scarce and expensive metallic elements or rather strong magnetic fields are usually needed to achieve strong magnetic actuation, thus often hindering their applicability. Therefore, the integration of multi-stimuli responsive materials presents exciting possibilities for the new generation of soft robotics. For example, light and magnetic field actuation can be combined to double the response strength, generate independent actions (such as bending and rotation)[14,15] or modulate one actuation using the other one as stimulus[16]. In addition, combining various stimuli overcomes the specific limitations in the applicability of each stimulus, hence, expanding the overall application range. However, despite the great potential of the synergetic combination of both actuation approaches[4], only few opto-magnetic actuators have been reported so far[14,15].

In addition to an efficient untethered actuation, self-sensing of the actuation strength is key to enable automatic and precisely controlled movements based on real-time feedback signals[17,18]. However, the inclusion of detection mechanisms in soft actuators remains a challenge, especially for small structures (i.e. less than a centimetre)[19]. Current actuation control involves either detecting the stimuli intensity at the actuated structure or directly quantifying its mechanical response. The direct detection of the stimuli, which implies the integration of external sensors in small, movable structures[20–22] can be technologically complex. Conversely, current methods to quantify the mechanical response involve either integrating wired electrical contacts and piezoelectric materials[3,17,23–25], using external bulky laser positioning systems with limited multiplexing capabilities, or analysing the shape changes via complex and inefficient imaging analysis, especially for small structures. To solve these technological issues, detection based on structural coloration presents several advantages, such as wireless and real-time sensing of the actuation strength[26,27]. Recently, several biomimetic, colour-changing materials have been developed, demonstrating

colorimetric response to various stimuli[28]. However, in order to include the colorimetric sensing mechanism into wirelessly controlled actuators, some aspects need to be considered. For example, the use of materials with sufficient light reflectance or transmittance (depending on the working configuration) is mandatory. Also, real-time colorimetric readout and analysis systems have not yet been integrated to soft actuators. These should be based on image processing rather than spectrometry to successfully integrate and simplify the self-sensing mechanism and to enable fast 2D movement quantification mapping[29–31].

In this chapter, a soft self-sensing mechanochromic actuator supporting dual wireless actuation with infrared (IR) light and magnetic fields is presented (Figure 4-1a). The actuator is based on a nanostructured iron (Fe) film coupled to a thin free-standing soft polydimethylsiloxane (PDMS) structure with a periodically corrugated back-side. The combination of materials allows single or dual optical/magnetic actuation (Figure 4-1b), while the periodically structured backside acts as a bendable diffraction grating, giving rise to structural coloration (Figure 4-1c). The optically/magnetically induced mechanical displacements in the free-standing structure generate intense structural colour changes (i.e. mechanochromic response) that are 2D-mapped and accurately quantified in real-time by the analysis of the Hue value in the pixels of the pictures taken by a conventional RGB camera or a smartphone camera.
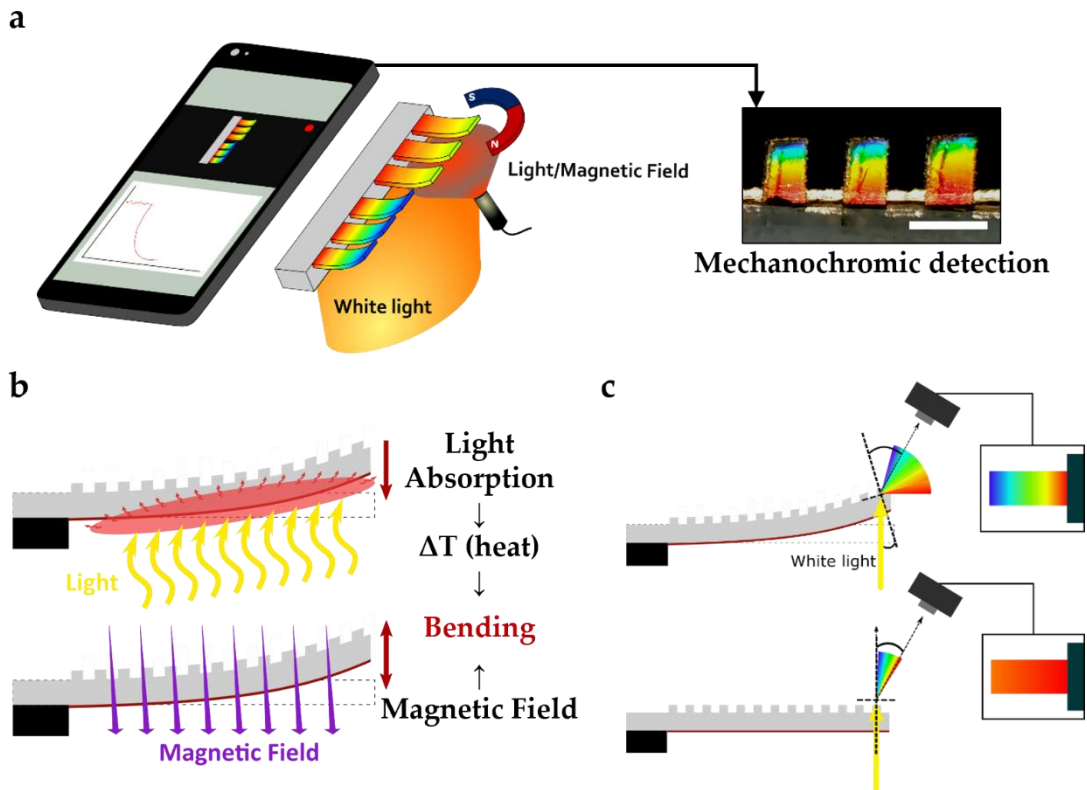

Figure 4-1. a) Schematic representation of the mechanochromic opto-magnetic soft actuator system. Inset picture: top-view image of the cantilever array (scale bar = 1 mm). b) Schematic of the two different actuation mechanisms (light and magnetic field gradients). c) Mechanochromic detection principle: changes of the cantilever angle produce a variation on the colour diffraction.

4.2. RESULTS AND DISCUSSION

4.2.1. Design and fabrication

The fabrication process of the opto-magnetic mechanochromic actuator shares some steps with the fabrication process presented in Chapter 3. It can be divided in five steps (Figure 4-2a): i) fabrication of the nanostructured iron layer composed of a hexagonal close-packed array of mechanically coupled iron "nanocaps" (diameter = 500 nm, thickness = 80 nm) that is prepared by combining colloidal self-assembly and electron beam Fe deposition[32,33] (Figure 4-2b; see Chapter 3); ii) preparation of the bendable photonic grating prepared by spin-coating PDMS (50 μm thickness) on a periodically corrugated silicone mould, obtained by casting a commercial diffraction grating (pitch 1600 nm) (Figure 4-2c); iii) mechanical coupling of the nanostructured Fe-layer to the flat surface of the PDMS by transfer printing; iv) definition of the suspended structures by laser writing (in this work, the dimensions of the structure are defined as length L = 1500 μm, width W = 600 μm and thickness t = 50 μm), and v) release from the grating mould (Figure 4-2d). Note that the fabricated free-standing structure presents an initial curvature caused by the residual mechanical stress between the metal and polymer layers which is responsible of the colour gradient observed before any external actuation (Figure 4-1a picture).
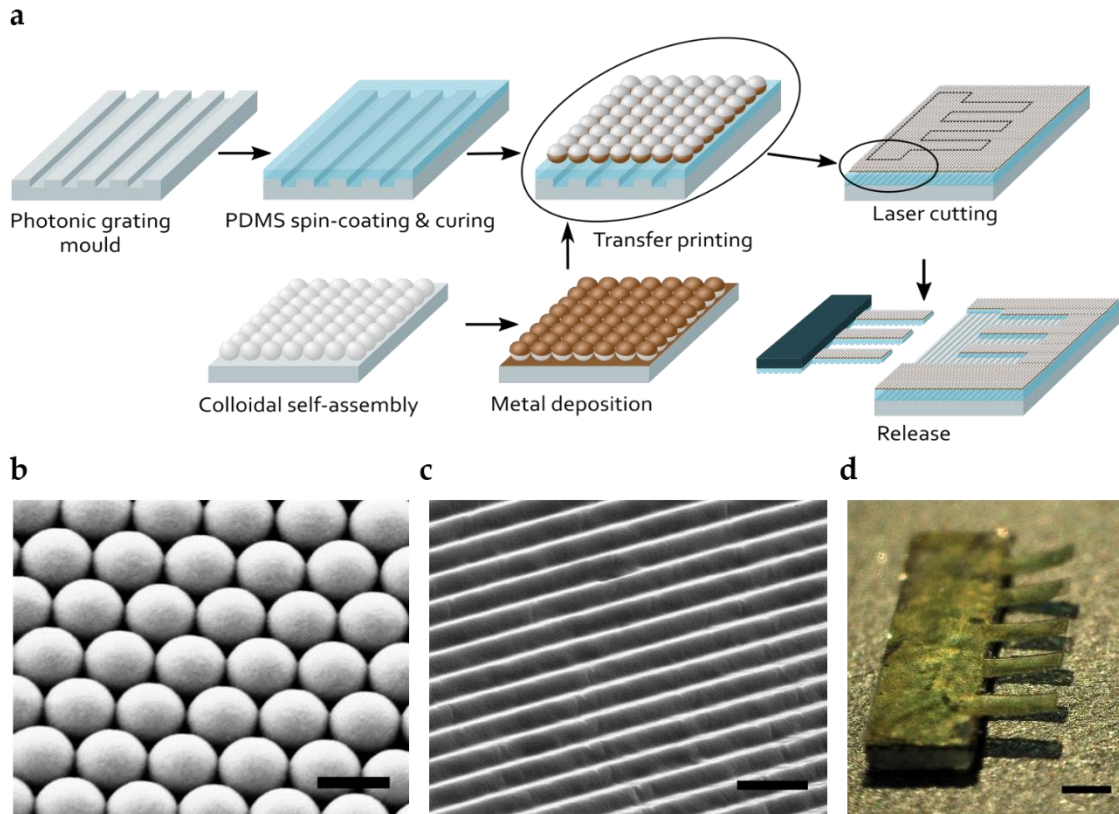
Figure 4-2. a) Schematic of the fabrication process. b) SEM image of the nanostructured iron (scale bar = 500 nm). c) SEM image of the PDMS photonic grating (scale bar = 2 μm). d) Photograph of the cantilever array (scale bar = 1 mm).

4.2.2. Mechanochromic detection

The periodically patterned PDMS surface diffracts white light, giving structural coloration to the free-standing actuator[31]. White light diffraction is described by Bragg's law: $m\lambda = d(sin(\theta_t) - sin(\theta_i))$, where m is the diffraction order, λ is the wavelength, d the grating pitch, and θ_t and θ_i are the transmitted and incident angles of the light relative to the surface normal (see Chapter 2). If the grating pitch and diffraction order are kept constant, the observed wavelength (i.e., colour) depends only on the incident and transmission angles with respect to the cantilever curvature. Therefore, any angular deflection of the structure is instantaneously converted into a structural colour change (i.e. mechanochromism). Therefore, the mechanical status of the free-standing structures is monitored in real-time by an RGB camera (analogous to any conventional smartphone camera) by using our open-source software (Figure 4-3) that obtains the colour shade, i.e., the Hue (H) value (from the Hue-Saturation-Lightness colour space[34]) in the pixels selected by the defined region of interest (ROI). Remarkably, this colorimetric detection approach provides 2D mechanochromic maps with high spatial resolution, which is not feasible in colorimetric systems based on spectral measurements[35–37]. The high spatial resolution enables direct visualization of strain gradients and the simultaneous analysis of individual free-standing structures for multiplexed actuation/detection systems.
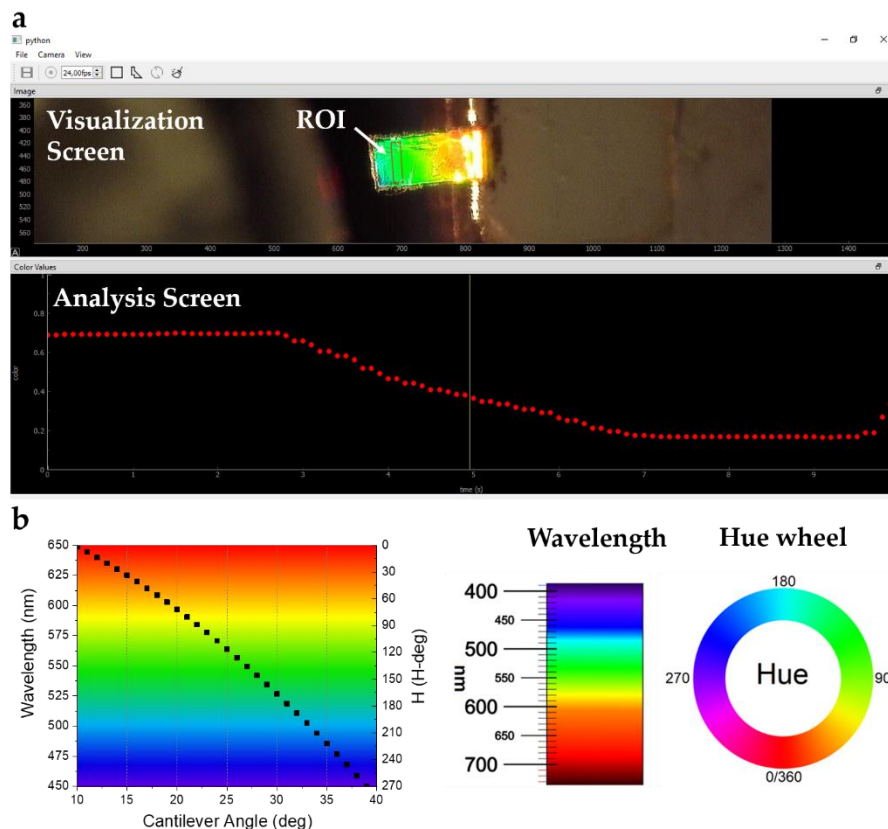
Figure 4-3. a) Screenshot of the interface of the colour analysis open-source app. b) Relationship between the cantilever angle and the displayed colour in wavelength and in the HSL colour space for incident and transmission angles $\theta_i = 0°$ and $\theta_t = 22°$, respectively.

4.2.3. Colorimetric analysis of optical actuation

Importantly, the selection of nanostructured iron layer on PDMS as constituting materials was motivated by the possibility to generate single and dual actuation based on their optical absorption and magnetic behaviour. The optical actuation of the structure is based on the photo-thermo-mechanical effects of a bimorph actuator, where the absorbed light by either the nanostructured iron or the PDMS layers, produces a temperature-induced mechanical surface stress that bends the structure[5]. The mechanical deflection is proportional to the temperature changes (ΔT) and the difference in thermal expansion coefficients (α) of the materials. Therefore, the high photothermal conversion efficiency combined with the large difference in the thermal expansion coefficient between the Fe and PDMS layers (i.e., α_{Fe}= 1.1·10^{-5} K^{-1}, α_{PDMS}= 3.1·10^{-4} K^{-1}) are crucial to maximize the photo-thermo-mechanical response of the actuators (see Chapter 2 and 3 for more details). The broadband absorption in the whole IR range enables light actuation outside the visible spectrum, and consequently, avoiding any crosstalk with the colorimetric detection system in the visible range. The broadband absorption range is achieved by the synergy between the damped plasmonic behaviour of the nanostructured-Fe layer, enabling strong absorption in the visible and near-infrared (NIR) and the PDMS strong absorption bands in the mid/long wave infrared (MWIR-LWIR) (see Chapter 3), which yields an average absorbance of 84% in the 0.4 μm to 18 μm range (minimum 75% @ 1250 nm – maximum 94% @ 530 nm). Importantly, the absorbed light is efficiently converted into thermal energy with minimal wavelength and incident angle dependence (due to its nanostructured morphology), as shown in Figure 4-4a (see Chapter 3 for more details on the material's photothermal efficiency). Namely, a linear dependence of the induced temperature increase with the light irradiance is observed, with similar heating rates at 808 nm and 1470 nm (0,21 K cm^2 mW^{-1} and 0,20 K cm^2 mW^{-1}, respectively), in accordance with the nearly flat broadband absorption. Moreover, the heating rate is virtually independent of the incident angle (0° or 45°) for both wavelengths.

The optomechanical actuation of the structures was characterized by taking advantage of the mechanochromic analysis strategy (Figure 4-1c). In Figure 4-4b, the colour change (i.e., the change in H, ΔH) at the cantilever free end (which is the region showing the largest deflection) is plotted as a function of the light intensity (I) for two NIR stimulation wavelengths (808 nm and 1470 nm). The light absorption caused a reduction of ΔH, which implies a reduction of the cantilever angle. Namely, the cantilever flattened its initial curvature upon the NIR actuation. The colour shift in Hue degrees (i.e., H-deg) provided a direct quantification of the mechanical actuation strength. Interestingly, the nanostructured-Fe/PDMS mechanochromic structure exhibited very notable colour changes upon laser irradiation, showing similar sensitivities ($S = dH/dI$) at 808 nm and 1470 nm (i.e., S_{Fe-808} = -0.62 H-deg·cm^2·mW^{-1}, $S_{Fe-1470}$ = -0.57 H-deg·cm^2·mW^{-1}), as expected from the photothermal characterization. Considering an experimental noise in the detection of the Hue changes of 0.35 H-deg, the minimum detectable NIR light irradiance is 1.8 mW·cm^{-2} (see Methods). It is important to highlight, even though the nanostructured-Fe is able to absorb a significant percentage of the white light used for illuminating the structures, the

incident irradiance (ca. 1 mW·cm^{-2}) is sufficiently low to avoid any observable effect on the actuation. Furthermore, by correlating the light-induced angular deflection (measured from the cantilever profile by image analysis) and the Hue change (i.e., 19.2 ± 0.5 H-deg/º according to Figure 4-5a), the minimum detectable deflection was determined to be 0.05° (see Methods). The opto-mechanical actuation was also correlated with the photothermal analysis to determine the relationship between colour shift and the induced temperature (Figure 4-5b). There is a nearly linear correlation between the colour change and the temperature, which is identical for both laser sources at 808 nm and 1470 nm. This analysis enables establishing a sensitivity of -3.0 H-deg·K^{-1} and a detection limit of 0.35 K, which can also be the base for innovative low-cost wireless temperature detectors.
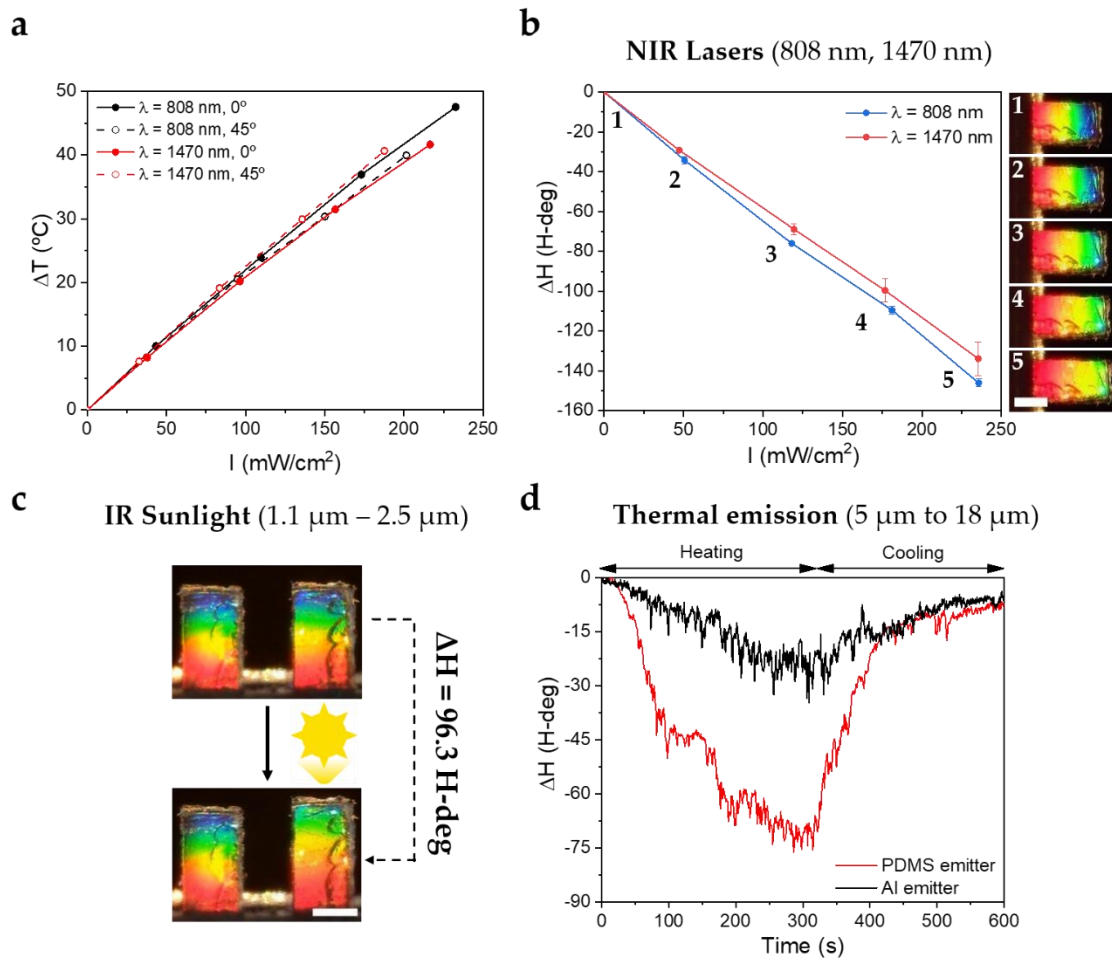
Figure 4-4. Optical actuation with colorimetric readout. a) Photo-thermal characterization of the nanostructured-Fe/PDMS for two different wavelengths (808 nm and 1470 nm) and two different angles of incidence (0º and 45º). b) Colorimetric response of the mechanochromic actuator to NIR light (λ = 808 nm and 1470 nm) with representative pictures showing the large colour changes. Scale bar = 0.5 mm. c) Colour shift generated by the sunlight filtered NIR-MWIR radiation focused on the right-side cantilever. Scale bar = 0.5 mm. d) Colour variation curve of the Fe/PDMS metamaterial actuated by the thermal IR emission radiated from PDMS or Al pieces (area 4 cm^2) heated at 120ºC.

Due to the broadband light absorption of the nanostructured-Fe/PDMS structure, the mechanical actuation can be also performed by natural light sources, such as the sunlight and even the weak infrared thermal emission from a heated body. The actuation strength of the NIR- MWIR spectral part of the sunlight is quantified by filtering out the visible and UV sunlight with a silicon lens. The use of the silicon lens has two purposes: (i) to block all wavelengths below 1.1 μm, and (ii) to focus the remaining low intensity radiation (from 1.1 μm to 2.5 μm[38]) into a single mechanochromic structure. The focused radiation yields a visually observable colour shift (96.3 H-deg) in comparison to the non-irradiated neighbouring structures (Figure 4-4c). Considering the previous angle and temperature calibration curves, an angular deflection of 5.2º, and a 32.5 K temperature increase is produced in the irradiated suspended structure by the absorbed NIR-MWIR sunlight (while the other structure remains unaltered). Additionally, the weak thermal emission in the MWIR- LWIR range from two emitters with very different emissivity (ε), PDMS (ε = 0.86) and aluminium (Al) (ε = 0.04), were used to demonstrate the capacity of actuation by a broad thermal emitter. The emitters were heated up to 120 °C, which corresponds to a peak wavelength of 7.5 μm, according to the blackbody radiation spectrum[39] (see Chapter 3). Figure 4-4d shows the large differences in the real-time colour shifts generated during the heating and cooling of both emitters (ca. 72 H-deg and 23 H-deg for the PDMS and Al emitters, respectively). Since the Al emissivity is very close to 0, and the measurements are not performed in vacuum, it can be assumed that the observed colour shift in this case arises only from the heated air, which should be similar for both emitters. Consequently, the contribution of the IR thermal emission from the PDMS emitter can be estimated by subtracting the Al signal, thus achieving a total MWIR-LWIR actuation signal of 49 H-deg.
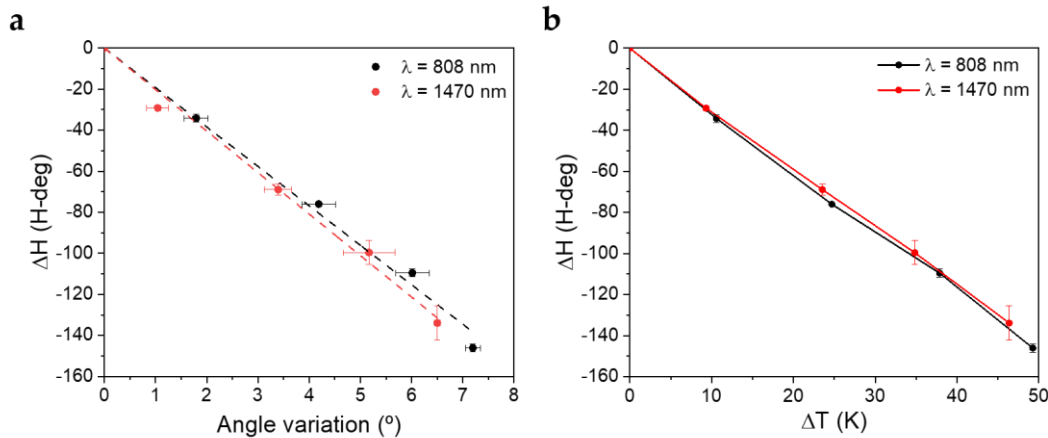
Figure 4-5. a) Colour change as a function of the cantilever angle variation. b) Colour change as a function of material temperature increase. Values extracted from photothermal characterization of Figure 4-4a.

4.2.4. Colorimetric analysis of magnetic actuation

In addition to the optical actuation, the magnetic character of the nanostructured-Fe layer enables the actuation using external magnetic fields. Interestingly, the semi-shells structure of the Fe layer confers it a magnetic response rather different from the soft-ferromagnetic

response expected for a polycrystalline flat Fe layer (i.e., a square in-plane loop with a small coercivity). The in-plane hysteresis loop evidences that the nanostructured-Fe exhibits in-plane ferromagnetic vortex configuration[40,41], where the magnetization of each Fe semi-shell curls around the structure (see schematic representation in Figure 4-6a), leading to a linear low-field susceptibility with nearly zero remanence and a negligible coercivity (Figure 4-6a). The out-of-plane hysteresis loop (Figure 4-6a) corresponds to a hard axis behaviour, indicating that the magnetization is in the film plane at low fields. This magnetic behaviour opens up versatile actuation capabilities based on the combination of magnetic torques and attractive/repulsive magnetophoretic forces by field gradients, depending on the configuration of the applied external field.

The magnetic actuation was characterized by analysing the mechanochromic response of the free-standing structure to the magnetic field generated by a spherical permanent magnet (FeNdB, 12 mm diameter; see schematic representation of the field lines in Figure 4-6b,c). The actuating magnetic field strength and direction is controlled by (i) moving the magnet with respect to the structure either parallel or perpendicular to the structures plane and (ii) changing the orientation of the magnet poles with respect to the free-standing structures (see Figure 4-6b,c). The induced magnetic actuation arises mainly from a complex combination of magnetic torques and magnetophoretic forces by the field gradient (see Chapter 2)[42,43], since the magnetostrictive contribution in Fe is expected to be much weaker. The relative contribution of each mechanism (torque and magnetophoretic) depends on the orientation of the magnetic field with respect to the nanostructured-Fe layer. Consequently, the response of the cantilever is different depending on the position and orientation of the magnet with respect to the cantilever (see Figure 4-6b,c). As can be seen in the figure, the free standing structures are very sensitive to the applied magnetic field except for one of the configurations. For example, when the magnet is approached from under the cantilever (Figure 4-6b) the magnetic sensitivity was determined to be -1.1 H-deg·mT^{-1} and 1.1 H-deg·mT^{-1} for the two orientations of the magnet, respectively. On the other hand, when the magnet is approached along the structures (Figure 4-6c), the sensitivity can be even larger, reaching -3.1 H-deg·mT^{-1} and a detection limit of 0.34 mT when the direction of the poles of the magnet is perpendicular to the plane of the cantilever. Finally, it is worth emphasizing that this strong and versatile magnetic actuation can be achieved with relatively low magnetic fields (in the order of mT), and only having a tiny fraction of ferromagnetic material in the structure (the nanostructured Fe layer constitutes barely 0.5% of the total mass of the actuator).
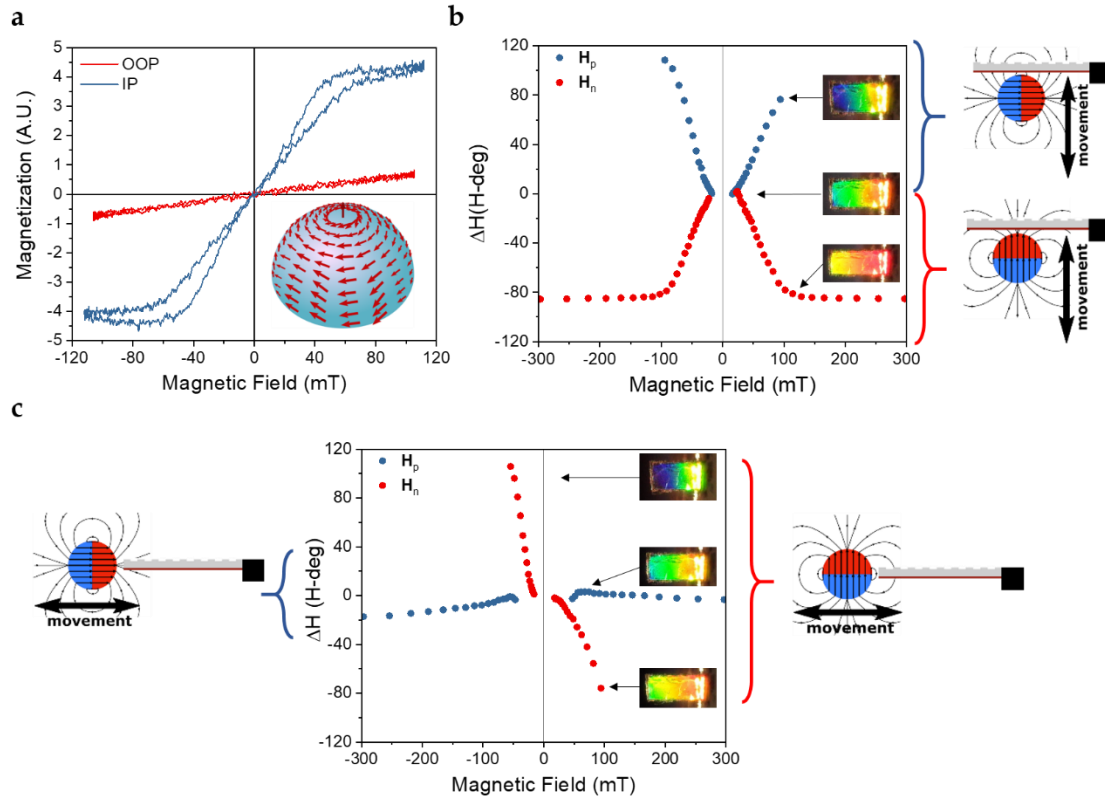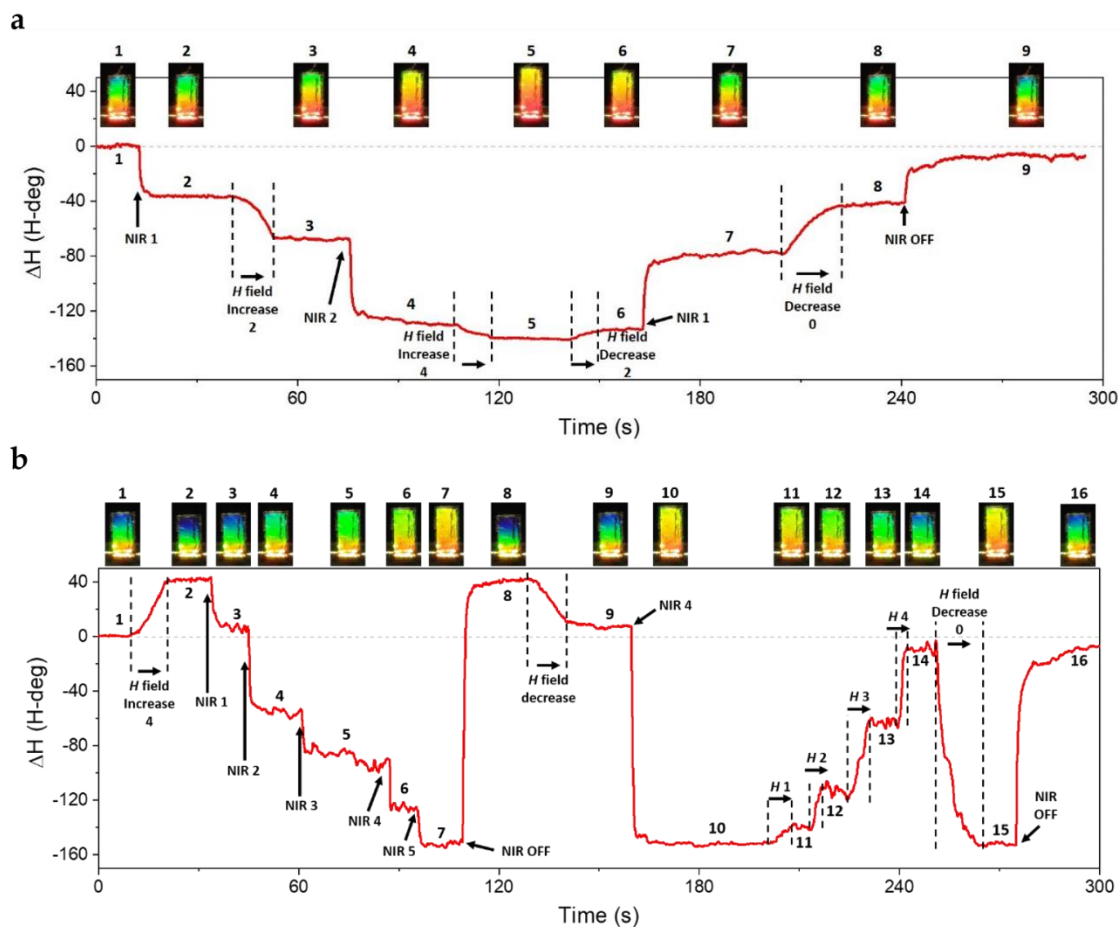
Figure 4-6. Magnetic actuation with colorimetric readout. a) Characterization of the in-plane (IP) and out-of-plane (OOP) magnetic response of the nanostructured-Fe/PDMS to an external magnetic field by Magneto-Optical Kerr Effect (MOKE). Shown in the inset is the schematic representation of the magnetic moments at zero field. b-c) Colorimetric detection of the magnetic actuation of a magnet moving in the direction b) normal to the cantilever plane and c) parallel to the cantilever, as shown schematically by the different cartoons. H_n and H_p represent the magnetic field orientation normal and parallel to the cantilever plane, respectively. The images in panels b) and c) correspond to the colorimetric response of the cantilever to diverse field conditions.

4.2.5. Combined opto-magnetic actuation

To demonstrate the full versatility of the structures, the optical and the magnetic actuation were combined (Figure 4-7). Since the magnetic actuation can drive the structure in both directions and the actuation mechanisms do not interfere between each other, two different approximations were explored: position the magnet to either (i) sum the optical and magnetic forces (Figure 4-7a) or (ii) to counteract the optical actuation by magnetic forces and vice versa (Figure 4-7b). In the first approach, the addition of photothermal and magnetic forces was shown in real time by the structure colour red-shifting. In the latter case, an initial magnetically-induced blue-shift was gradually overcompensated by increasing laser irradiation ($\lambda = 808$ nm), and vice versa. Therefore, both actuations can be used independently or combined. Also, they can counteract each other or sum up the actuation strength by only changing the orientation of the magnetic field with respect to the structure. Thereby, the possibility to combine both untethered actuation mechanisms together with the simplicity to adjust the magnetic response direction and the real-time self-

sensing of the actuation, shows great promise to further develop multifunctional wireless and smart soft actuators.

Figure 4-7. Real time colorimetric response monitoring of the actuator to simultaneous photothermal and magnetic actuation. The magnet is oriented with respect to the structure as in Figure 4-6c. The diverse pictures show representative images of the colorimetric response of the structure at each stage. Note that laser intensities "*NIR 1, 2, 3, 4* and *5*" correspond to 75, 150, 225, 300 and 375 mW·cm⁻², respectively, The magnetic field "*H field increase 1, 2, 3* and *4*" correspond to 35, 43, 55 and 71 mT, respectively.

4.2.6. Actuation dynamics

Other important factors to develop competitive externally controlled mechanical actuators are (i) their robustness and endurance, i.e., their capacity to return to the initial state after actuation repeated times and (ii) the dynamic actuation/detection range under time-varying actuation sources. Firstly, the dynamic response of the system during a single pulse of light and magnetic field was analysed (Figure 4-8a). In both cases, the colour abruptly changed during the initial second or actuation. However, while in the case of magnetic actuation the maximum deflection was almost instantaneous, in the case of light stimulation, the maximum deflection was only reached after 30 seconds due to the thermal swelling process. Similarly, the return to the original state was also much slower for the light stimulus due to the thermal cooling process of the material. In contrast, when the external magnetic field

was removed, the cantilever rapidly returned to its initial position. The periodic stimulation of the system with a square-pulsed laser (intensity 277 mW·cm^{-2}) revealed a substantial decay of the maximum colour change (i.e., maximum deflection) when increasing the frequency of the pulses due to the slow thermal process (Figure 4-8b). Despite the movement amplitude decay, the optical actuation and detection could be performed up to 10 Hz (Figure 4-8c). In parallel, the endurance and robustness of the nanostructured-Fe/PDMS mechanochromic structure was confirmed by the reversible optical actuation/detection for more than 200 on-off cycles at high light intensities (Figure 4-8d).
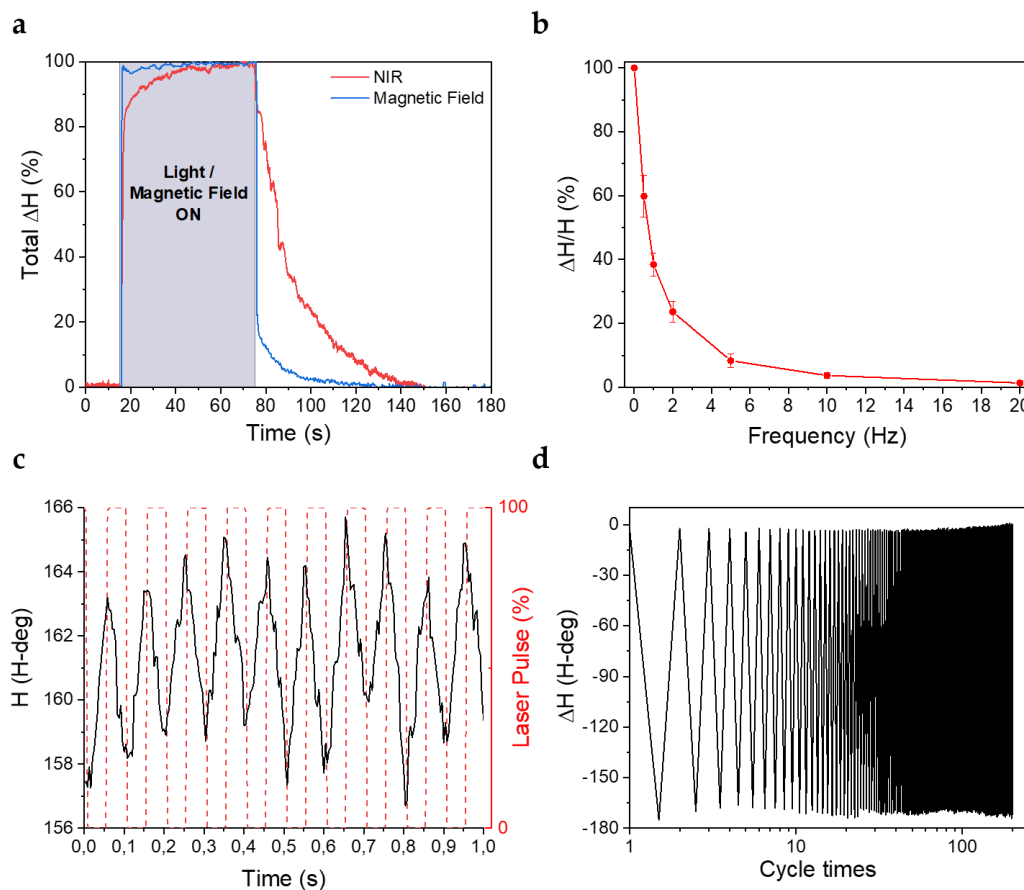
Figure 4-8. Demonstration of the opto-mechanical robustness and dynamic response of the nanostructured-Fe/PDMS metamaterial. a) Real-time detection of the colour response (normalized) in a complete on-off cycle of NIR light (I = 277 mW·cm^{-2}) and magnetic field ($\mu_o H$ = 76 mT). b) Colorimetric response induced by square-shaped laser radiation at increasing frequency. c) Real-time colorimetric response to a 10 Hz laser pulse. d) Long-term response under >200 on-off cycles.

4.3. CONCLUSIONS

In summary, an untethered dual mechanochromic soft actuator that is capable to independently respond to both light and magnetic stimuli (either individually or combined) is developed. In addition, the system allows for a real-time colorimetric readout of the actuation strength using a simple RGB (e.g., smartphone) camera. The combination of a nanostructured Fe-layer mechanically linked to a PDMS layer enables merging optical

and magnetic actuation due to the unique combination of intense and broadband optical absorption of the bilayer and the high magnetic moment and tailored magnetic configuration of the nanostructured iron layer. The Fe/PDMS metamaterial not only shows high sensitivity both using light (-0.62 H-deg·cm^2·mW^{-1}) and magnetic fields (-3.1 H-deg·mT^{-1}) but also a remarkable endurance. It is worth to emphasize that in contrast to other proposed procedures, this soft opto-magnetic actuator enables independent, dual opto-magnetic actuation mechanisms, in which the temperature-independent magnetic actuation can rapidly regulate or amplify the photothermal response with controlled strength and direction, only using a tiny amount of magnetic material, as well as low magnetic fields. The dual opto-magnetic responsivity of the system and its mechanochromic self-sensing capabilities provide new appealing pillars for the future development of wireless multifunctional smart systems for soft-robotics and soft actuator applications in diverse fields.

4.4. REFERENCES

1. Hines, L., Petersen, K., Lum, G. Z. & Sitti, M. Soft actuators for small-scale robotics. *Adv. Mater.* **29**, 1603483 (2017).

2. Amjadi, M. & Sitti, M. High-performance multiresponsive paper actuators. *ACS Nano* **10**, 10202–10210 (2016).

3. Amjadi, M. & Sitti, M. Self-sensing paper actuators based on graphite–carbon nanotube hybrid films. *Adv. Sci.* **5**, 1800239 (2018).

4. Sitti, M. & Wiersma, D. S. Pros and cons: magnetic versus optical microrobots. *Adv. Mater.* **32**, 1906766 (2020).

5. Lim, H. *et al.* Construction of a photothermal Venus flytrap from conductive polymer bimorphs. *NPG Asia Mater.* **9**, e399 (2017).

6. Zeng, H., Wani, O. M., Wasylczyk, P., Kaczmarek, R. & Priimagi, A. Self-regulating iris based on light-actuated liquid crystal elastomer. *Adv. Mater.* **29**, 1701814 (2017).

7. Yang, M. *et al.* Photoresponsive Actuators built from carbon-based soft materials. *Adv. Opt. Mater.* **7**, 1900069 (2019).

8. Zhang, X. *et al.* Photoactuators and motors based on carbon nanotubes with selective chirality distributions. *Nat. Commun.* **5**, 2983 (2014).

9. Wang, T., Torres, D., Fernández, F. E., Wang, C. & Sepúlveda, N. Maximizing the performance of photothermal actuators by combining smart materials with supplementary advantages. *Sci. Adv.* **3**, e1602697 (2017).

10. Ze, Q. *et al.* Magnetic shape memory polymers with integrated multifunctional shape manipulation. *Adv. Mater.* **32**, 1906657 (2020).

11. Huang, H.-W., Sakar, M. S., Petruska, A. J., Pané, S. & Nelson, B. J. Soft micromachines with programmable motility and morphology. *Nat. Commun.* **7**, 12263 (2016).

12. Hu, W., Lum, G. Z., Mastrangeli, M. & Sitti, M. Small-scale soft-bodied robot with multimodal locomotion. *Nature* **554**, 81–85 (2018).

13. Fusco, S. *et al.* An integrated microrobotic platform for on-demand, targeted therapeutic interventions. *Adv. Mater.* **26**, 952–957 (2014).

14. da Cunha, M. *et al.* An untethered magnetic- and light-responsive rotary gripper: shedding light on photoresponsive liquid crystal actuators. *Adv. Opt. Mater.* **7**, 1801643 (2019).

15. da Cunha, M. *et al.* On untethered, dual magneto- and photoresponsive liquid crystal bilayer actuators showing bending and rotating motion. *Adv. Opt. Mater.* **7**, 1801604 (2019).

16. Li, M. *et al.* Flexible magnetic composites for light-controlled actuation and interfaces. *Proc. Natl. Acad. Sci. U.S.A.* **115**, 8119–8124 (2018).

17. Chen, L. *et al.* Graphene-based actuator with integrated-sensing function. *Adv. Functi. Mater.* **29**, 1806057 (2019).

18. Wang, H., Totaro, M. & Beccai, L. Toward perceptive soft robots: progress and challenges. *Adv. Sci.* **5**, 1800541 (2018).

19. Sitti, M. Voyage of the microrobots. *Nature* **458**, 1121–1122 (2009).

20. Zhao, H., O'Brien, K., Li, S. & Shepherd, R. F. Optoelectronically innervated soft prosthetic hand via stretchable optical waveguides. *Sci. Robot.* **1**, (2016).

21. Robinson, S. S. *et al.* Integrated soft sensors and elastomeric actuators for tactile machines with kinesthetic sense. *Extreme Mech. Lett.* **5**, 47–53 (2015).

22. Yeo, J. C. *et al.* Flexible and stretchable strain sensing actuator for wearable soft robotic applications. *Adv. Mater. Technol.* **1**, 1600018 (2016).

23. Nakamura, A. & Kawakami, S. An actuator–sensor hybrid device made of carbon-based polymer composite for self-sensing systems. *AIP Adv.* **9**, 065311 (2019).

24. Zhu, S.-E. *et al.* Graphene-based bimorph microactuators. *Nano Lett.* **11**, 977–981 (2011).

25. Hui, Y., Gomez-Diaz, J. S., Qian, Z., Alù, A. & Rinaldi, M. Plasmonic piezoelectric nanomechanical resonator for spectrally selective infrared sensing. *Nat. Commun.* **7**, 11249 (2016).

26. Qin, M., Sun, M., Hua, M. & He, X. Bioinspired structural color sensors based on responsive soft materials. *Curr. Opin. Solid State Mater. Sci.* **23**, 13–27 (2019).

27. Shang, L., Zhang, W., Xu, K. & Zhao, Y. Bio-inspired intelligent structural color materials. *Mater. Horiz.* **6**, 945–958 (2019).

28. Zhao, Q., Wang, Y., Cui, H. & Du, X. Bio-inspired sensing and actuating materials. *J. Mater. Chem. C* **7**, 6493–6511 (2019).

29. Zhu, Y., Xu, M., Jin, H., Yang, J. & Dong, E. Chromatic surface microstructures on bionic soft robots for non-contact deformation measurement. in *2017 IEEE International Conference on Robotics and Automation (ICRA)* 6737–6742 (2017).

30. Suzumori, K., Mihara, M. & Wakimoto, S. Beautiful flexible microactuator changing its structural color with variable pitch grating. in *2011 IEEE International Conference on Robotics and Automation* 2771–2776 (2011).

31. Escudero, P., Yeste, J., Pascual-Izarra, C., Villa, R. & Alvarez, M. Color tunable pressure sensors based on polymer nanostructured membranes for optofluidic applications. *Sci. Rep.* **9**, 3259 (2019).

32. Li, Z. *et al.* Simultaneous local heating/thermometry based on plasmonic magnetochromic nanoheaters. *Small* **14**, 1800868 (2018).

33. Li, Z. *et al.* Magnetically amplified photothermal therapies and multimodal imaging with magneto-plasmonic nanodomes. *Appl. Mater. Today* **12**, 430–440 (2018).

34. Cheng, H. D., Jiang, X. H., Sun, Y. & Wang, J. Color image segmentation: advances and prospects. *Pattern Recognit.* **34**, 2259–2281 (2001).

35. Pris, A. D. *et al.* Towards high-speed imaging of infrared photons with bio-inspired nanoarchitectures. *Nat. Photon.* **6**, 195–200 (2012).

36. Zhang, F. *et al.* Infrared detection based on localized modification of Morpho butterfly wings. *Adv. Mater.* **27**, 1077–1082 (2015).

37. Lu, T. *et al.* Near-infrared trigged stimulus-responsive photonic crystals with hierarchical structures. *ACS Appl. Mater. Interfaces* **9**, 34279–34285 (2017).

38. Gueymard, C. A. The sun's total and spectral irradiance for solar energy applications and solar radiation models. *Sol. Energ.* **76**, 423–453 (2004).

39. Baranov, D. G. *et al.* Nanophotonic engineering of far-field thermal emitters. *Nat. Mater.* **18**, 920–930 (2019).

40. Streubel, R. *et al.* Magnetic vortices on closely packed spherically curved surfaces. *Phys. Rev. B* **85**, 174429 (2012).

41. Streubel, R. *et al.* Magnetism in curved geometries. *J. Phys. D: Appl. Phys.* **49**, 363001 (2016).

42. Adhikari, R., Sarkar, A. & Das, A. K. A versatile cantilever beam magnetometer for ex situ characterization of magnetic materials. *Rev. Sci. Instrum.* **83**, 013903 (2012).

43. Zheng, P. Magnetic MEMS and its applications. (Florida State University, 2004).

5. Stretchable Plasmonic-Enhanced Fabry-Perot Cavities Based on Self-Swallowed Arrays of Au Semi-shells in Elastomer Films

Stretchable photonics is a field in rapid development facing many different challenges. One of them is the efficient integration of optical elements into stretchable matrixes. In this line, the inclusion of plasmonic nanoparticles and photonic structures in elastomeric arrays are an interesting option to include optically-responsive elements into deformable materials. In this work, the fabrication of the first stretchable plasmonic-enhanced Fabry-Perot cavity is demonstrated. The material is composed by an array of gold (Au) semi-shells embedded into a wrinkled elastomer matrix. The mechanical tensions during the fabrication process produce the spontaneous swallowing of the semi-shells inside the matrix, as well as the generation of surface wrinkles. Thanks to this particular geometry and composition, the material presents multiple Fabry-Perot resonances which are amplified by the intrinsic plasmonic resonances of the semi-shells and tuned by the surface wrinkles. The optical response to applied strain is numerically and experimentally determined, demonstrating a competitive sensitivity in both wavelength and intensity variations, and showing large robustness and long-term reliability. Finally, the photothermal capabilities of the Au semi-shells were explored to incorporate additional value to the material for temperature or light sensing applications. This work takes a step forward to the generation of novel stretchable optical materials and its applications in flexible photonics, such as wireless strain sensing.

5.1. INTRODUCTION

During the last decade, the development of flexible and stretchable devices has enormously expanded. Flexible electronics is already a mature field with significant applications as wearable devices[1] or in-situ health diagnosis[2,3]. In this line, the integration of optical structures into foldable or stretchable devices can drastically expand the range of potential applications. For example, the development of foldable photonic systems (i.e. optical structures with high robustness to bending and twisting) has been encouraged by the demand of flexible displays[4–6]. However, the development of stretchable photonic systems has been hampered by the difficulty to achieve robust and controlled integration of the optical elements into soft, elastic matrixes. Two different approaches can be distinguished in the field of stretchable photonics. On the one hand, optical structures that operate in harsh mechanical conditions conserving their optical features (such as stretchable LEDs[7] and optical waveguides[8,9]) are interesting for flexible electronics and displays. On the other hand, devices whose optical properties can be reversibly tuned by the application of a mechanical strain are appealing for applications in sensing, imaging and communications. In this context, stretchable optical fibres have shown the capacity to withstand large deformations and to provide reversible and sensitive light transmission changes under mechanical deformations[10]. However, they are limited by the need of optical interconnections and do not allow direct visualization of the strain distribution on a surface. On the other hand, photonic and plasmonic micro/nanostructures are interesting alternatives since they can also provide spectral mechanical responses (i.e. mechanochromism). Mechanochromic materials are usually based on photonic gratings[11,12] or plasmonic nanoparticle arrays[13–16] (see Chapter 1 and 4). Their colour change induced by mechanical deformation allows both optomechanical tuneability and 2D mapping of the strain in the material. Photonic gratings can be very sensitive, but they usually require highly reflective substrates to work in the reflection mode and show high angular dependence, which complicates their incorporation into certain functional devices. In contrast, plasmonic-based stretchable materials generally present angle-independence and high optical signal. However, their mechanical spectral tuneability and sensitivity is lower and sometimes lack of a wide linear detection range. To overcome some of these limitations, materials that present a combined photonic and plasmonic response to mechanical stimulation are currently being investigated to obtain the benefits of both types[17,18]. Nevertheless, there is a need to develop new stretchable optical devices with larger mechanical tuneability, versatility and sensitivity, as well as to simplify their fabrication and improve the robust integration.

Here, the first stretchable and plasmonic-enhanced Fabry-Perot material is presented. It is composed of an array of plasmonic semi-shells integrated into an elastomeric film by an innovative self-swallowing process. The mechanisms that are responsible for the spontaneous swallowing of Au semi-shells into the elastomer matrix and the wrinkle formation are first analysed, demonstrating that the process can be controlled by the polymer curing temperature. Then, the opto-mechanical response of the self-embedded arrays of semi-shells is characterized, providing theoretical and experimental

demonstrations of the plasmonic and Fabry-Perot optical modes, together with the influence of the wrinkled PDMS surface. Finally, the sensitivity of the material to the applied strain is analysed, together with the demonstration of its robustness and versatile usage.

5.2. RESULTS AND DISCUSSION

5.2.1. Fabrication

The fabrication process is schematically shown in Figure 5-1a and described as follows. Firstly, an array of Au semi-shells is fabricated by colloidal self-assembly of polystyrene nanospheres on a silicon substrate, followed by Reactive Ion Etching (RIE) to slightly reduce and tune the particle size, and Au evaporation by highly directional electron beam vapour deposition. Then, the liquid PDMS mixed at a 10:1 ratio with the cross-linker, is poured on the semi-shell array, and it is cured in an oven under controlled temperature. After releasing the cured PDMS layer from the substrate, two remarkable and unexpected morphologic effects are observed: i) the arrays of Au semi-shells were swallowed by the polymer matrix (this was revealed by the cross-section analysis of the cured PDMS films) and ii) the spontaneous formation of large wrinkles at the same surface. For a curing temperature of 100°C, the penetration depth was approximately 1 μm for all the semi-shells. The embedded semi-shells closely followed the wrinkles pattern, which exhibited an amplitude (A) and wavelength (Λ) of 1 μm and 16 μm, respectively (Figure 5-1b,c).

To comprehensively explain these phenomena, Figure 5-2a illustrates the dynamics during the curing process. The most probable cause for the self-swallowing of the Au semi-shells arrays and the spontaneous wrinkle formation is the stress generated by the differential curing rate in the PDMS matrix, which is locally accelerated by the Au interfaces acting as polymerization catalysts. This was motivated by the fact that PDMS polymerization is based on a hydrosilylation reaction, which is catalysed by transition metal complexes[19]. Typical commercial curing agents include platinum complexes, but other transition metals (*e.g.*, gold) can also behave as a catalyst and promote local cross-linking reactions. Therefore, the accelerated curing rate of the elastomer in contact to the Au interfaces produced a mechanical stress that is sufficiently strong to overcome the weak Van der Waals forces between the Au semi-shells and the substrate, thereby swallowing the Au semi-shells inside the polymeric matrix. This enhanced curing reaction also generated a stiffer skin polymer layer, which was the responsible of forming the wrinkled pattern.
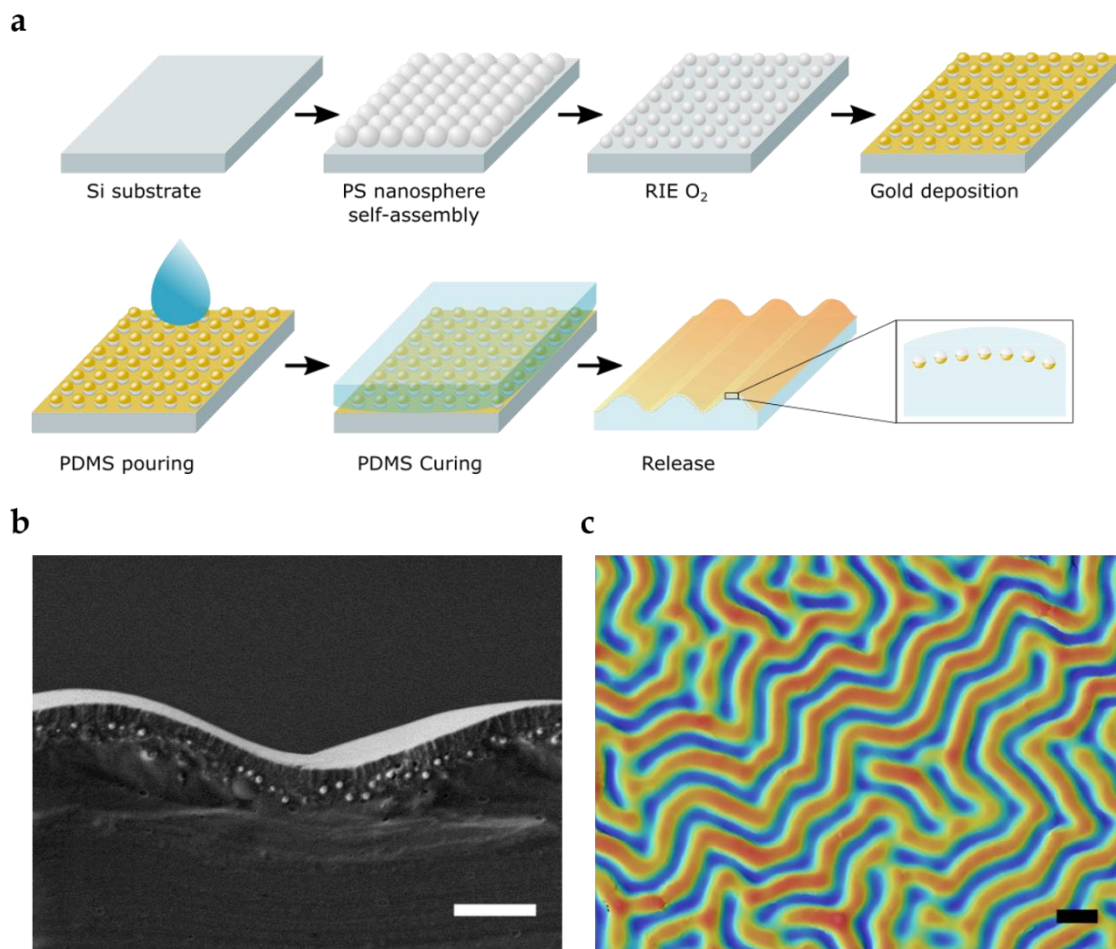
Figure 5-1. a) Schematic of the fabrication process. b) Cross-section SEM image of the wrinkled-PDMS with swallowed Au-semi-shells. Scale = 2 µm. c) Confocal microscopy image of the wrinkled PDMS surface. Scale = 20 µm.
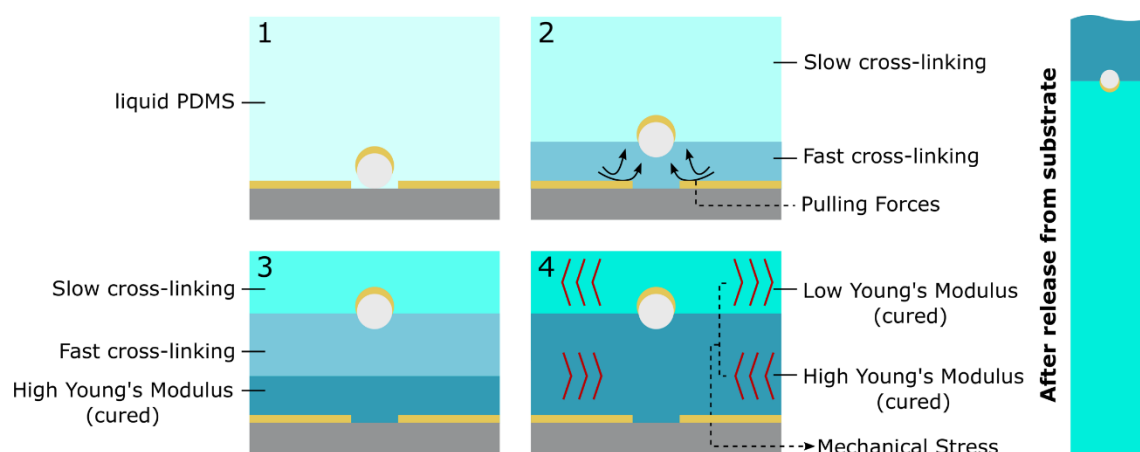
Figure 5-2. a) Schematic of the self-swallowing process of the Au semi-shells due to the differential curing rate and generation of mechanical stress in the material.

To demonstrate this hypothesis, two control tests were carried out. Firstly, the PDMS was substituted by a photocurable silicone. Since the polymerization reaction was only driven

by the ultraviolet light in this case, the Au semi-shells stayed at the polymer surface and the wrinkles were not formed (Figure 5-3a). In addition, in an analogous experiment the Au coating was substituted by Al, which is not a catalyst for the cross-linking reaction. In these conditions the PDMS was thermally cured at a homogeneous rate without generating local mechanical stress. As a result, the Al semi-shells also remained at the polymer surface (Figure 5-3b) and the wrinkles were not formed.

a

Au semi-shells + Photocurable Silicone

b

Aluminium semi-shells + PDMS

c

Au semi-shells + PDMS. Curing T = 25ºC
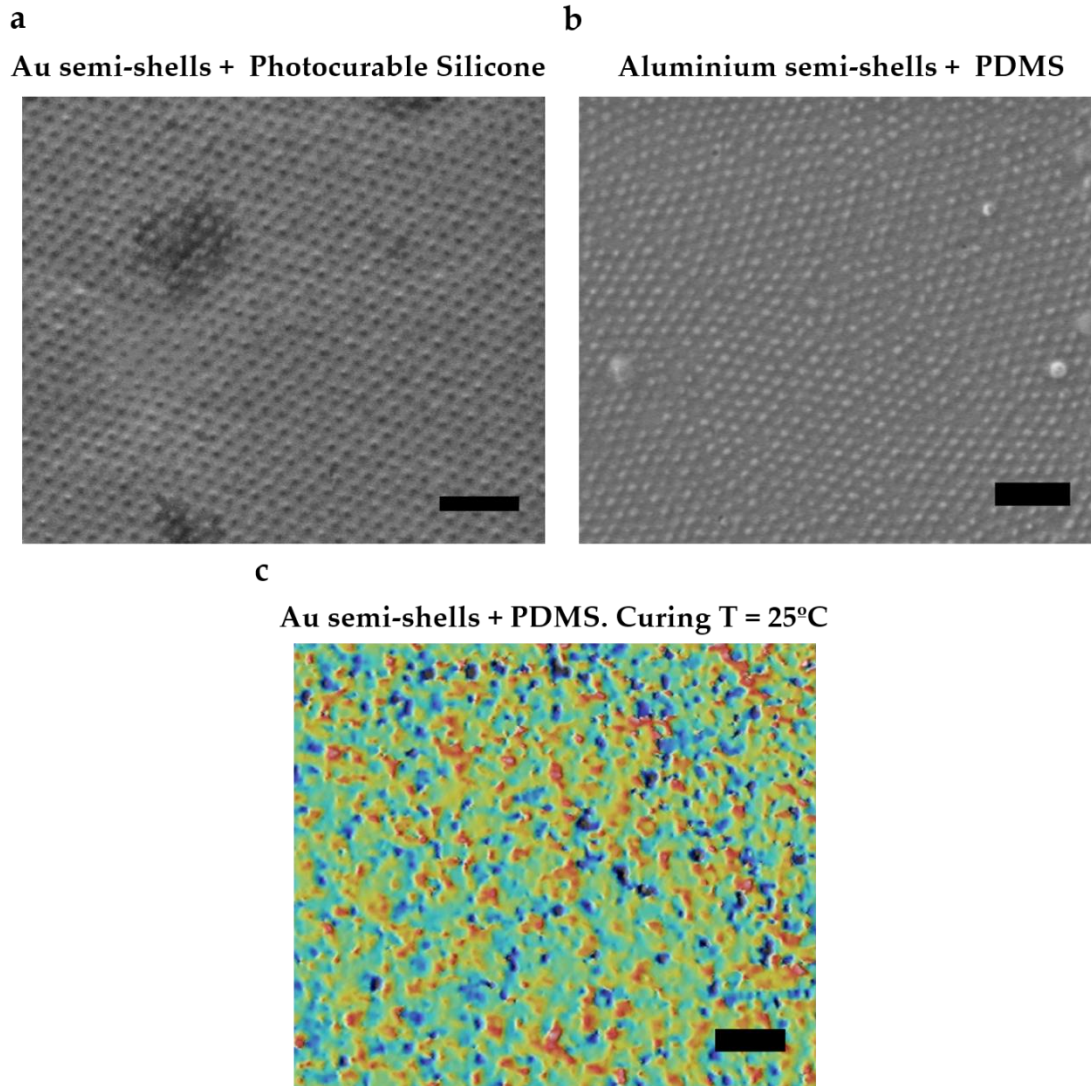
Figure 5-3. a) Top-view SEM image of half-embedded Au semi-shells on photocurable silicone. Scale = 1 μm. b) Top-view SEM image of half-embedded Al semi-shells on PDMS. Scale = 1 μm. c) Confocal microscopy image of PDMS cured at room temperature on an Au semi-shells array. Scale = 20 μm. Colour scale range (blue to red) = 1.74 μm.

The wrinkles formation triggered by the local stiffening of the top PDMS layer is consistent with the linear buckling theory. If a hard skin layer in contact to a soft semi-infinite substrate is considered, the surface wrinkles are created when the residual strain overcomes a certain threshold value[20], ε_c, given by:

$$\varepsilon_c = \frac{1}{4}\left(\frac{3E_S}{E_L}\right)^{\frac{2}{3}} \tag{5-1}$$

where E_L and E_S are the Young's modulus of skin layer and the substrate, respectively. If this condition is fulfilled, the wrinkles' amplitude (A) and wavelength (Λ) are governed by the following equations:

$$A = h_L\sqrt{\frac{\varepsilon - \varepsilon_c}{\varepsilon_c}} \tag{5-2}$$

$$\Lambda = 2\pi h_L\left(\frac{E_L}{3E_S}\right)^{\frac{1}{3}} \tag{5-3}$$

where h_L is the thickness of the skin layer and ε the generated strain. Therefore, the wrinkle dimensions depend on the Young's Modulus mismatch and the thickness of the hard skin layer. In the case of the Au enhanced cross-linking, the differential curing rates inside the PDMS provoked an increased Young's Modulus in the thin layer in contact to the Au interfaces, which generated the stress responsible of the wrinkles formation.

Remarkably, both the semi-shells swallowing depth and the associated wrinkles dimensions (A, Λ) can be accurately controlled and tuned with the curing rate. In order to isolate the temperature dependence from other factors affecting the curing rate, the area of the sample and the PDMS volume were kept constant. As can be observed in Figure 5-4a, both semi-shell penetration depth and wrinkle wavelength were sharply reduced as the curing temperature increased up to 140°C, after which the reduction was much slower. The lower depth can be explained by the very rapid viscosity increase generated by the cross-linker in the whole PDMS matrix, which hampered the Au semi-shells penetration inside the polymer. Therefore, lower curing temperatures enable a longer penetration time before the polymer matrix is fully cross-linked and stops the process. However, heating is needed to trigger the catalytic effect of Au, as curing at room temperature lead unwrinkled surfaces with the semi-shells next to the surface (Figure 5-3c).

Interestingly, these effects can be spatially controlled by exploiting the high photothermal efficiency of Au semi-shells[21,22] to generate the local heat necessary to activate the polymerization reaction by the cross-linker and the Au interfaces. To prove it, an infrared light beam (diameter 2 mm, wavelength 1064 nm, intensity 6 W/cm^2) was used to irradiate the Au semi-shell array covered by liquid PDMS. The photo-induced heat was sufficient to crosslink the PDMS, and to generate a clear increase of the wrinkle wavelength as the temperature decreases (Figure 5-4b), which confirmed the dependence of the wrinkle morphology on the curing rate. The temperature gradient generated by the infrared light is shown in Figures 5-4c,d.
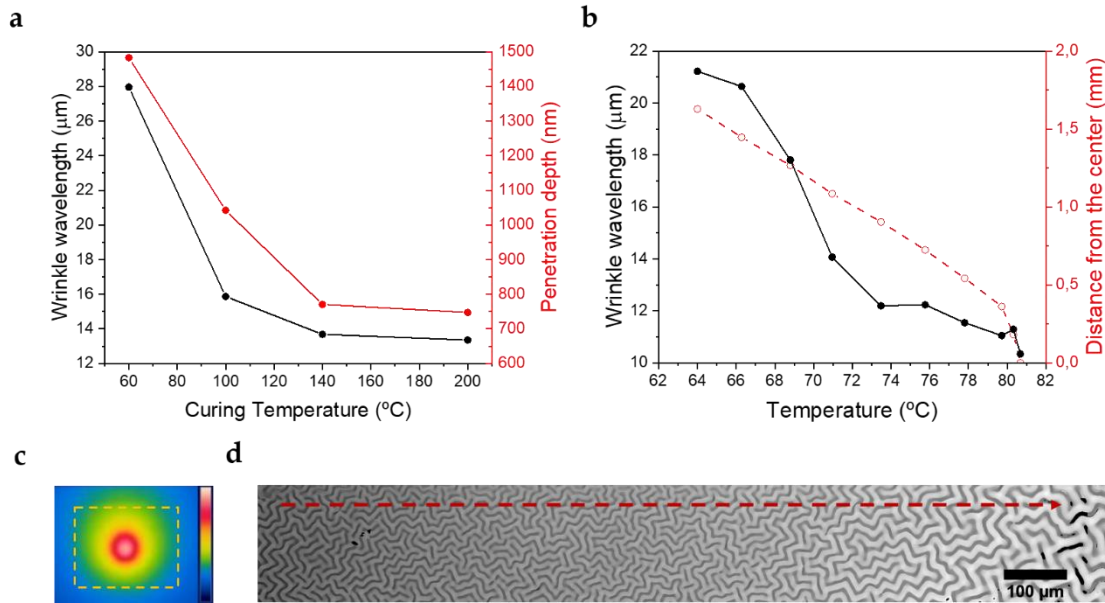
Figure 5-4 | a) Schematic of the self-swallowing process of the Au semi-shells due to the differential curing rate and generation of mechanical stress in the material. b) Dependence of the semi-shells penetration depth and wrinkle wavelength on the curing temperature. c) Gradient photothermal curing: temperature and wrinkle wavelength as a function to the distance to the laser spot. d) Thermographic image of the laser irradiation (colour bar range from 20°C to 75°C), where the yellow rectangle represents the sample. e) Confocal microscopy image of the photothermally cured sample. The discontinuous red arrow shows the temperature gradient (from high to low temperature).

5.2.2. Optomechanical characterization

The new capacity to integrate arrays of plasmonic nanoparticles at controlled depths inside a transparent elastomer matrix opens the path to the development of novel opto-mechanically active stretchable devices. This remarkable ability can be observed in the reflection spectra of the semi-shell arrays inside the PDMS cured at different temperatures and under increasing strains in Figure 5-5a,b,c. To do so, a fibre-couple halogen lamp coupled to a bifurcated optical fibre-bundle was used, transmitting the incident light to the sample and collecting the reflected light, which was spectroscopically analysed.

In the case of 140°C curing temperature, the semi-shells penetration was *ca.* 700 nm and the reflection spectra presented three clear peaks, whose peaks positions and intensities experienced intense blue-shifts and intensity increases, respectively, as the film was stretched. (Figure 5-5a). The curing at 100°C with a penetration depth of 1000 nm (Figure 5-5b) gave rise to four narrower reflection peaks that also showed blue-shifts under an increasing strain, although the intensity increase was slightly lower. Finally, the sample cured at 60°C showing semi-shells penetration of 1500 nm (Figure 5-5c) exhibited five reflection peaks that clearly blue-shifted, but whose amplitude remained low even at high strain. This opto-mechanical behaviour is in stark contrast with the spectral response of the

semi-shell array that were directly transferred to the surface of cured PDMS (Figure 5-5d). This sample showed a broad reflection peak from 650 nm to 1100 nm, whose peak position and intensity barely changed by the stretching.

To understand the nature of these multiple peaks, both the penetration depth of the Au semi-shell arrays and the wrinkled pattern should be considered. The semi-shell array behaves as a plasmonic enhanced broadband highly reflective layer inside the PDMS matrix, thereby creating a Fabry-Perot (FP) cavity. In the FP cavity, the incoming light suffers multiple reflections leading to constructive and destructive interferences depending on its wavelength and the cavity length. Therefore, the reflected light presents peaks at the wavelengths that fulfil the cavity resonance conditions. However, the observed resonances were not equally intense in the experiment, being the peaks located at shorter wavelengths weaker. This is due to the coupling of the FP modes with the localized plasmon resonances (LSPR) of the Au semi-shells. As Figure 5-5d shows, the reflectance of the Au semi-shells arrays on the surface is maximized in the 650 nm to 1100 nm range and substantially decay for lower wavelengths, thus reducing the efficiency of the FP cavity. This reflectance decrease is consistent with the Finite Difference Time Domain (FDTD) simulations of the Au arrays of semi-shells with diameters spanning from 140 nm to 170 nm, i.e. in the same range of the observed experimental diameters ($d_{avg} = 160 \pm 12$ nm) (Figure 5-6). As a result, the plasmonic-enhanced FP cavity effects were mainly observed in the 650 nm to 1100 nm range.
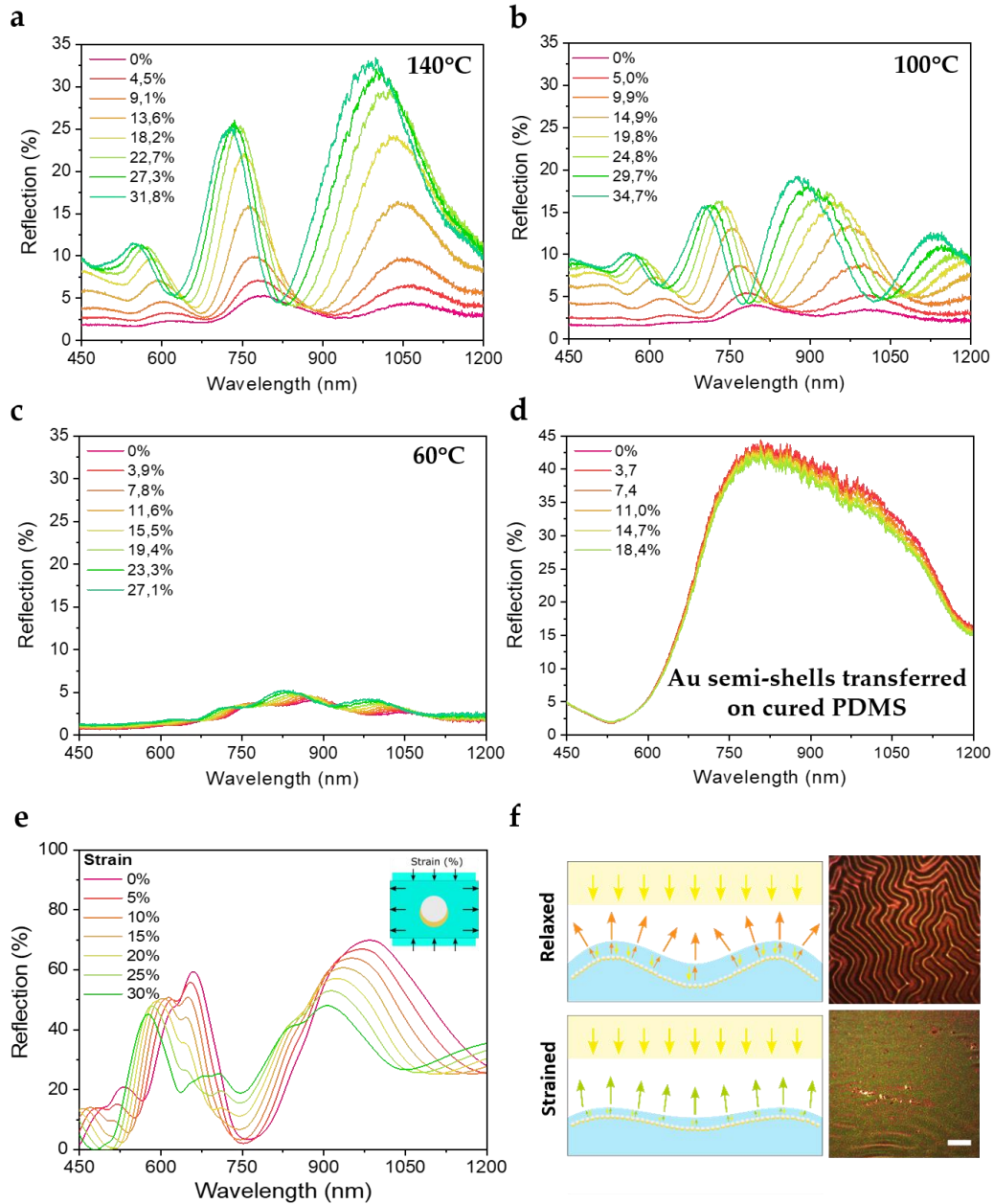
Figure 5-5. a) Optomechanical response in the reflection spectra as a function of the generated strain of the swallowed arrays of Au semi-shells inside the PDMS cured at 140°C, b) 100°C and c) 60°C. d) Experimental reflection spectra as a function of the strain the array of Au semi-shells transferred on the cured PDMS surface. e) FDTD simulations of the opto-mechanical response of the Au- semi-shells /FP cavity in the reflection spectra for increasing mechanical strain parallel to the sample surface. f) Schematic of the light reflection in the wrinkled FP-cavity before and after applying mechanical strain, together with the optical microscopy images of the wrinkled surface at 0% and 30% strain. Scale bar = 20 μm.
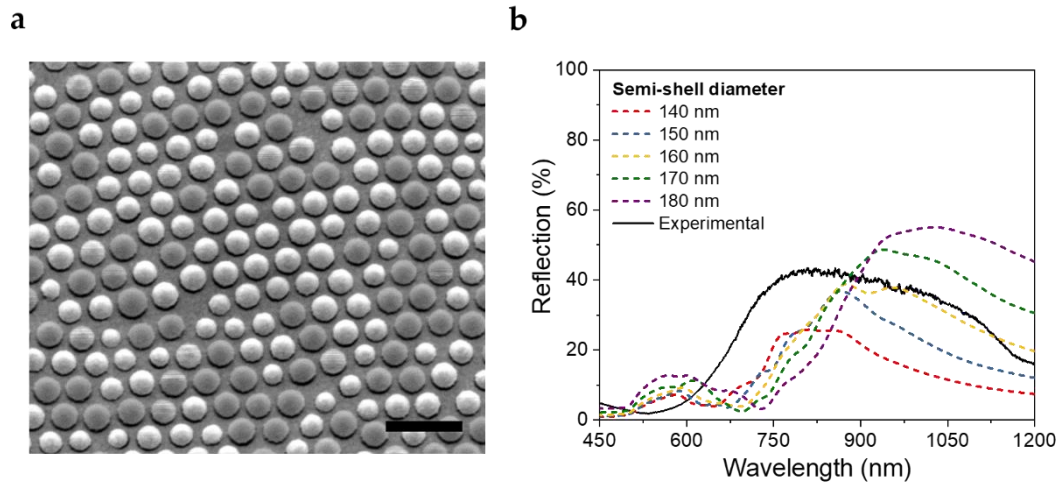
Figure 5-6. a) SEM top-view image of a Au semi-shell array on silicon. Scale = 500 nm. b) FDTD simulations and experimental measure of Au semi-shell arrays transferred to a PDMS substrate.

The FP cavity also explains the blue-shift of the multiple resonant peaks exhibited in Figure 5-5a,b,c induced by the film stretching. The strain parallel to the film yields a compression in the perpendicular directions that can be estimated by the Poisson ration of the material. As a result, the applied stress produces a reduction in the polymer cavity, thereby causing the blue-shift of the resonant peaks. This behaviour is consistent with the FDTD simulations of the nanoplasmonic-FP cavity mimicking the mechanical strain (Figure 5-5e). A semi-shell array of 150 nm of diameter and penetration depth of 700 nm was selected to model the sample cured at 140°C (Figure 5-5a). The induced strains were simulated in the direction parallel to the film ranging from 0 to 30% by increasing the pitch of the semi-shell arrays in that direction, taking into account the expected shortening in the perpendicular directions, given by the Poisson ratio of the PDMS[23]. The simulations showed the multiple peaks arising from the FP-cavity/LSPR coupling together with the blue-shift for increasing strain, achieving a 78 nm shift at 30% strain for the peak initially located at 1050 nm, which agrees with the experimental results (76 nm blue-shift).

To experimentally corroborate that the blue-shift was due to the variation of the FP cavity thickness and not to plasmonic near-field interaction between semi-shells, the opto-mechanical response was experimentally analysed by using polarized light parallel and perpendicular to the stretching direction (Figure 5-7). In the case of a near-field interaction between semi-shells, a blue-shift would be expected due to the separation of semi-shells in the stretching direction, and red-shift in the perpendicular direction resulting from the compression. However, similar blue-shifts in both polarization directions were observed, thereby confirming the FP cavity shrinking effect. The negligible near-field interaction between the Au semi-shells was also responsible of the extremely weak opto-mechanical response of the Au semi-shells arrays transferred to the flat surface of the cured PDMS (Figure 5-5d).
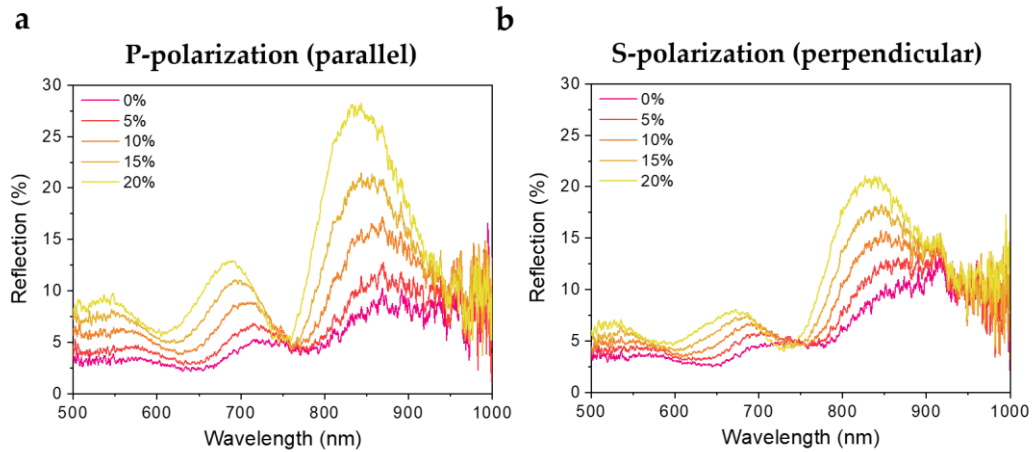
Figure 5-7. Optomechanical response of the swallowed arrays of Au semi-shells inside the PDMS to increasing strain. Incident light is polarized in parallel (a) and perpendicular (b) to the stretching direction.

Although the spectral shifts were accurately modelled, the FDTD simulations did not predict the large intensity increase experimentally generated in the strained samples, which can be attributed to the wrinkled surface (Figure 5-5f). The surface corrugation generated the reflection and refraction of the incident light at higher angles following the Snell law, thus causing an important decrease in the transmitted and reflected light in the normal direction in which the light was captured by the optical fibre. As the film stretching reduced the wrinkles amplitude and wavelength, the light reflection and refraction angles shifted towards the incident direction, thus increasing intensity captured by the optical fibre. In addition, an optical microscope was used to observe the changes in the wrinkle pattern at different strains and to correlate the images with the spectral measurements (Figure 5-5f). For increasing strain, the wrinkled patterns flattened and the colour shifted from dark red to a combination between red and green. This was consistent with the detected blue-shift of the reflection peaks in spectral measurements.

Interestingly, the spontaneous wrinkle generation effect was also observed on PDMS films cured on flat Au films without Au semi-shells (Figure 5-8). Analogously, the gold surface is responsible to accelerate the cross-linking at the PDMS surface, thereby generating a stiffer layer that could be observed experimentally (Figure 5-8a) and consequently, the formation of surface wrinkles (Figure 5-8b). To demonstrate the easiness of this surface patterning procedure, PDMS was cured on a substrate coated by gold on only half of the surface. As a results, a PDMS sample displaying surface wrinkles only on the part cured on gold was obtained (Figure 5-8c). This also confirmed the importance of the Au interface to induce the hardening of the PDMS skin layer. Furthermore, this sample, only composed by PDMS, also shows an increase in the reflection and transmission in response to strain as a result of the wrinkles flattening (Figure 5-9).

a

b

c
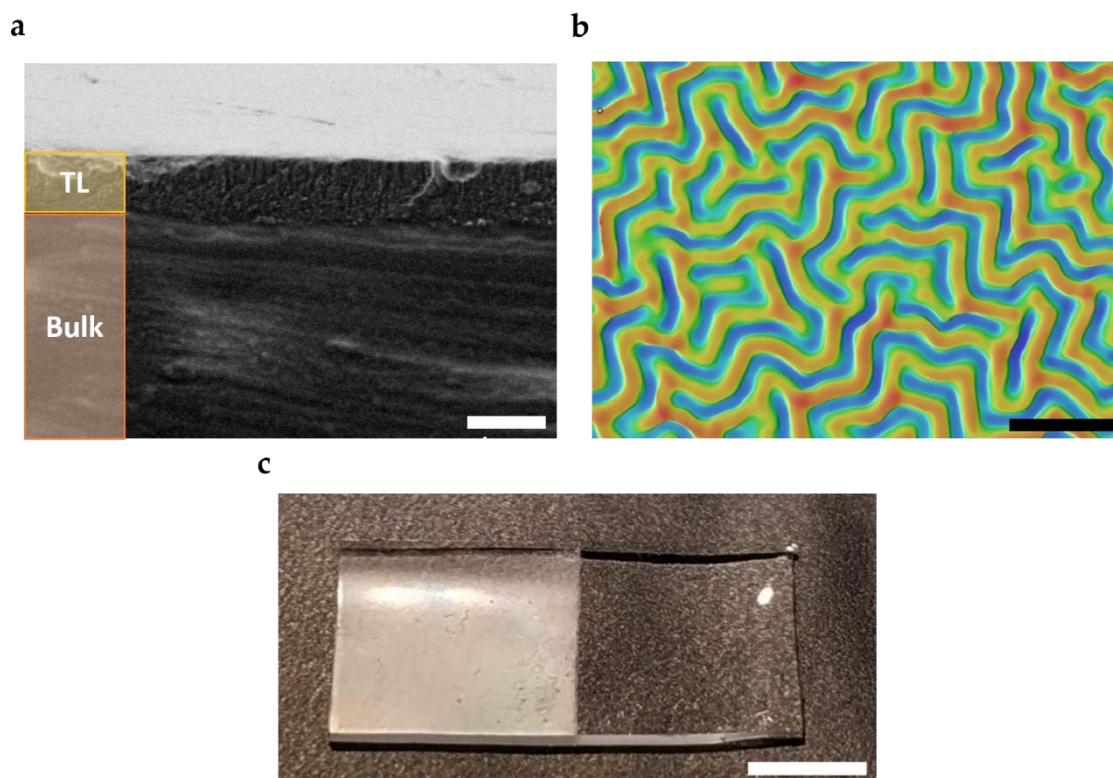
Figure 5-8. a) SEM cross-section image of wrinkled PDMS cured on a flat gold surface. Scale = 1 µm. b) Confocal microscopy image of wrinkled PDMS without semi-shells. Scale = 50 µm. c) Picture of a PDMS sample cured on a silicon sample with half of the surface with gold coating. The surface wrinkles appear only on the left side, which are visible due to the light scattering. Scale = 5 mm.
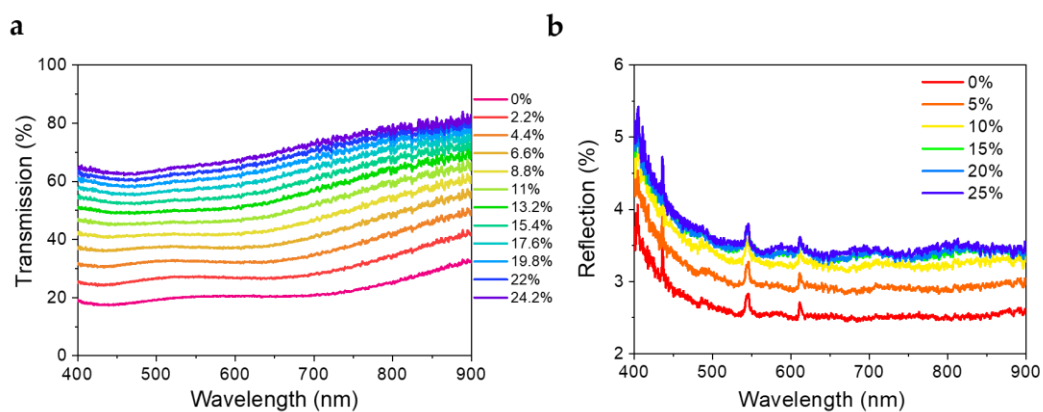

Figure 5-9. Transmission (a) and reflection (b) spectra to increasing strains for a surface-wrinkled PDMS without Au semi-shells.

5.2.3. Application to strain sensing

To demonstrate the use of this new material as an optical strain sensor, the optomechanical response of the sample cured at 140ºC is analysed (Figure 5-10). In order to work in the linear range and be able to measure in both compression and stretching directions, a pre-strain of 13.6% was set as the origin point. The material shows a wavelength shifting sensitivity of -2.31, -2.04 and -2.47 nm·%s^{-1} for each of the three peaks, respectively (Figure 5-10a). The three resonances present similar sensitivities in terms of wavelength shifting since the phenomenon is purely photonic. By contrast, the peaks close to the plasmonic resonance display a much bigger sensitivity differences in terms of reflection intensity due to the amplification of the light reflection, being 0.45, 1.07 and 1.30 %$_R$·%s^{-1} (Figure 5-10b). The wavelength strain sensitivity of this material is competitive with the plasmonic strain sensors reported to date, which range between 0.7 and 3.5 nm·%s^{-1}. However, not many materials are reported to detect strain in both wavelength and reflectivity. In this material, the strain measurements can be also carried out by exploiting the intensity increase in the 650-1100 nm wavelength range or even combining both responses. Furthermore, the multiple resonances along the visible and infrared spectrum allows the detection at the most convenient wavelength in each particular scenario. Then, the robustness of the material was demonstrated by testing it to over 100 stretching-compression cycles. Its response did not show many significant variations neither in wavelength shift (Figure 5-10c) or in reflectivity change (Figure 5-10d), thereby demonstrating its long-term reliability as strain sensing material.

Finally, the optomechanical properties of the material were further explored by taking advantage of the photothermal capabilities of Au semi-shells. As previously described, the photogenerated heat by the Au semi-shells is capable to increase the temperature of the sample very efficiently. Therefore, the photo-induced mechanical strain to the material due to the high thermal expansion of PDMS was analysed by heating the material by an infrared laser (λ = 1064 nm) (Figure 5-10e). A red-shifting and a decrease in intensity of the resonances were observed for increasing temperatures. This behaviour was attributed to the thermal expansion of PDMS, which widens the Fabry-Perot cavity and swell the surface wrinkles. The demonstration that the photogenerated heat can be also used for actuation and detected by the material optical response opens the path for new strategies in temperature and light detection or even in combination with mechanical structures for new classes of soft robotics.
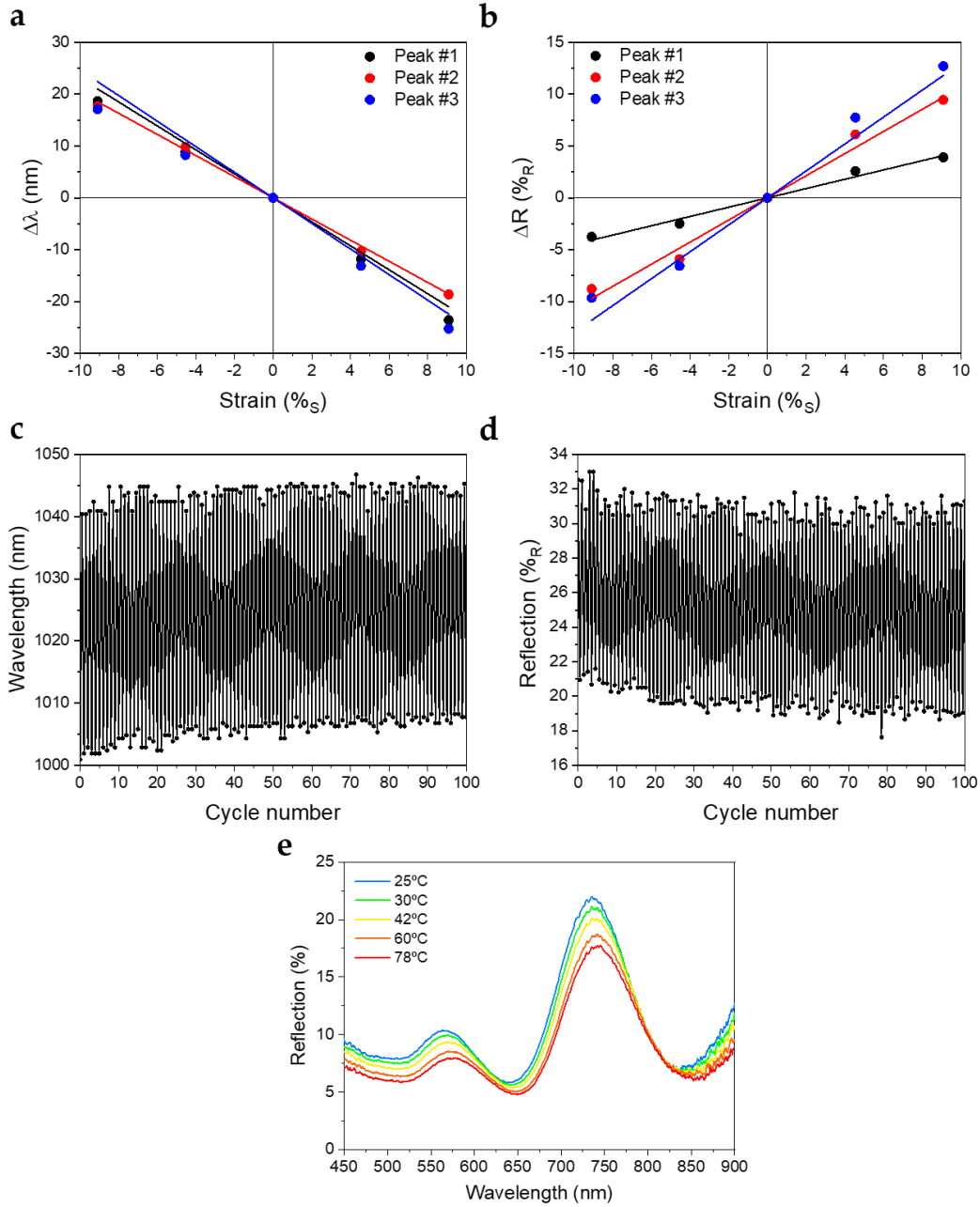
Figure 5-10. a-b) Resonance wavelength shift (a) and reflectivity variations (b) of the three different resonances for stretching and compression of the Au-semi-shells/wrinkled PDMS cured at 140ºC. c-d) Wavelength and reflection values for the most intense resonance of the material for 100 cycles of stretching and compression. e) Visible spectrum of the material after being heated with an infrared laser ($\lambda = 1064$ nm) at different intensities.

5.3. CONCLUSIONS

In this work, a stretchable optomechanical material composed by an Au semi-shell array embedded into a wrinkled PDMS matrix was developed. The self-swallowing of the Au semi-shells and the wrinkling of the PDMS surface was demonstrated to be caused by a differential curing rate between the bulk PDMS and the surface, which can be controlled through the curing temperature. Also, the photothermal capabilities were explored to perform the polymer cross-linking using an infrared light source. Then, the opto-mechanical response of the material was characterized: the reflection spectrum is composed by multiple Fabry-Perot resonances that are amplified by the coupling with the plasmonic modes of the semi-shells. These resonances blue-shift and present an enormous increase in reflectivity upon mechanical strain due to the shrinking of the FP cavity and the flattening of the surface wrinkles, respectively. Finally, the response of the material was determined by measuring the wavelength shift and the reflectivity increase, demonstrating a competitive sensitivity and a versatile measuring methodology, together with large robustness of the material. Also, additional usages in actuation or light detection were proposed by taking advantage of the photothermal capabilities of semi-shells. Overall, this study demonstrates a novel class of plasmomechanical materials and sets the foundations for their application to flexible photonic systems, such as wireless strain sensors adaptable to environments of difficult access and curved surfaces.

5.4. REFERENCES

1. Kim, D.-H. *et al.* Epidermal electronics. *Science* **333**, 838–843 (2011).

2. Imani, S. *et al.* A wearable chemical–electrophysiological hybrid biosensing system for real-time health and fitness monitoring. *Nat. Commun.* **7**, 11650 (2016).

3. Lee, H. *et al.* A graphene-based electrochemical device with thermoresponsive microneedles for diabetes monitoring and therapy. *Nat. Nanotechnol.* **11**, 566–572 (2016).

4. Sekitani, T. *et al.* Stretchable active-matrix organic light-emitting diode display using printable elastic conductors. *Nat. Mater.* **8**, 494–499 (2009).

5. Kim, S. *et al.* Low-power flexible organic light-Emitting diode display device. *Adv. Mater.* **23**, 3511–3516 (2011).

6. Yokota, T. *et al.* Ultraflexible organic photonic skin. *Sci. Adv.* **2**, e1501856 (2016).

7. Vosgueritchian, M., Tok, J. B.-H. & Bao, Z. Light-emitting electronic skin. *Nat. Photon.* **7**, 769–771 (2013).

8. Li, L. *et al.* Monolithically integrated stretchable photonics. *Light Sci. Appl.* **7**, 17138–17138 (2018).

9. Zhao, H., O'Brien, K., Li, S. & Shepherd, R. F. Optoelectronically innervated soft prosthetic hand via stretchable optical waveguides. *Sci. Robot.* **1**, (2016).

10. Leber, A., Cholst, B., Sandt, J., Vogel, N. & Kolle, M. Stretchable thermoplastic elastomer optical fibers for sensing of extreme deformations. *Adv. Funct. Mater.* **29**, 1802629 (2019).

11. Howell, I. R., Li, C., Colella, N. S., Ito, K. & Watkins, J. J. Strain-tunable one dimensional photonic crystals based on zirconium dioxide/slide-ring elastomer nanocomposites for mechanochromic sensing. *ACS Appl. Mater. Interfaces* **7**, 3641–3646 (2015).

12. Kamita, G. *et al.* Biocompatible and sustainable optical strain sensors for large-area applications. *Adv. Opt. Mater.* **4**, 1950–1954 (2016).

13. Han, X., Liu, Y. & Yin, Y. Colorimetric stress memory sensor based on disassembly of gold nanoparticle chains. *Nano Lett.* **14**, 2466–2470 (2014).

14. Maurer, T. *et al.* The beginnings of plasmomechanics: towards plasmonic strain sensors. *Front. Mater. Sci.* **9**, 170–177 (2015).

15. Zhu, X., Shi, L., Liu, X., Zi, J. & Wang, Z. A mechanically tunable plasmonic structure composed of a monolayer array of metal-capped colloidal spheres on an elastomeric substrate. *Nano Res.* **3**, 807–812 (2010).

16. Lütolf, F., Casari, D. & Gallinet, B. Low-cost and large-area strain sensors based on plasmonic fano resonances. *Adv. Opt. Mater.* **4**, 715–721 (2016).

17. Abhilash, T., Balasubrahmaniyam, M., Patra, A. & Kasiviswanathan, S. Plasmon resonance mediated enhancement in Fabry-Pérot cavity modes. *Appl. Phys. Lett.* **104**, 241112 (2014).

18. Yoo, D., Johnson, T. W., Cherukulappurath, S., Norris, D. J. & Oh, S.-H. Template-stripped tunable plasmonic devices on stretchable and rollable substrates. *ACS Nano* **9**, 10647–10654 (2015).

19. Stark, F. O., Falender, J. R. & Wright, A. P. 9.3 - Silicones. in *Comprehensive Organometallic Chemistry*, 305–363 (Pergamon, 1982).

20. Chen, C.-M. & Yang, S. Wrinkling instabilities in polymer films and their applications. *Polym. Int.* **61**, 1041–1047 (2012).

21. Li, Z. *et al.* Magnetically amplified photothermal therapies and multimodal imaging with magneto-plasmonic nanodomes. *Appl. Mater. Today* **12**, 430–440 (2018).

22. Li, Z. *et al.* Simultaneous local heating/thermometry based on plasmonic magnetochromic nanoheaters. *Small* **14**, 1800868 (2018).

23. H. Pritchard, R., Lava, P., Debruyne, D. & M. Terentjev, E. Precise determination of the Poisson ratio in soft materials with 2D digital image correlation. *Soft Matter* **9**, 6037–6045 (2013).

6. Conclusions and Future Work

In this thesis, different challenges in the study, development and application of soft plasmomechanical metamaterials have been tackled. In particular, the use of metal nanostructures in combination with soft polymers has been demonstrated to be especially appealing to develop diverse sensing and actuation platforms. The tunable optical features of plasmonic materials, such as their enhanced absorption or selective resonances, together with the special mechanical properties of elastomers have been used and combined to achieve the necessary optomechanical (and even magnetomechanical) response for each particular application. Hereunder, the specific conclusions of this thesis are detailed.

6.1. CONCLUSIONS

- The damped plasmonic behaviour of nanostructured Fe (Fe semi-shells) have been explored, demonstrating broadband absorption from UV to NIR. The proposed Fe nanomaterial can be transferred to flexible/elastic substrates such as PDMS. This combination of materials achieves an unprecedented ultrabroadband and angle-independent absorption (average 84% from 0.3 to 18 μm) due to the enhanced light transmission of Fe and the strong absorption bands of PDMS in the MWIR-LWIR.

- The broadband and angle-independent light absorption of the material, together with the mismatch of the mechanical properties between the nanostructured-Fe and PDMS is exploited to build light-responsive soft actuators. Specifically, a prototype for a self-regulating iris is developed, which automatically regulates the light transmitted through the device by opening/closing its aperture as a function of the incident intensity. The device can be operated by different light sources within the UV, visible and IR part of the spectrum. Furthermore, a light-controlled mechanical gripper and a light-triggered electrical switch are also demonstrated. These results open the path to different applications in power free light regulation, such as ophthalmologic devices, light protectors or optomechanical components in soft-robotics.

- The magnetic properties of the nanostructured-Fe have been studied and exploited to add magneto-mechanical response to the developed actuators. The combination of light and magnetic actuation has been demonstrated, enabling multi-functionality, as well as regulation of optical actuation with magnetic fields (or vice-versa). Furthermore, the dynamic response of the structure as well as their endurance have been demonstrated.

- A self-sensing strategy for soft actuators has been designed and incorporated. This is based on the mechanochromic response of photonic gratings in movable structures, together with the implementation of an automated analysis software based on the real-time measurements of the Hue pixel values on the images captured with a conventional camera. The mechanical status of the structure and therefore, any actuation (arising from light or magnetic fields, for example) can be detected wirelessly, in real-time and 2D-mapped. This technology can be employed for the real-time wireless detection of mechanical strain in deformable materials and combined with actuators to develop automated soft robotic systems.

- A new stretchable material based on Au semi-shells that are self-embedded into a wrinkled elastomeric matrix at controlled depths has been developed. Its fabrication process shows an innovative procedure based on the mechanical tensions during the polymer crosslinking that is catalysed by the Au surface of the nanostructures. The curing temperature has been demonstrated to be critical during the process and thereby allowing to tune the morphological and the optomechanical response of the material.

- Due to its peculiar morphology, the Au-semi-shell/wrinkled-PDMS material shows an unconventional optomechanical behaviour that combines the coupling between the plasmonic resonances of Au semi-shells and Fabry-Perot cavities together with the

scattering effects of surface wrinkling. Its reflection spectrum responds to mechanical strain in both wavelength and intensity, with similar sensitivity to other reported materials with more complex fabrication processes. It also shows strong robustness and stretchability that makes it suitable for wireless strain sensing in environments of difficult access and/or curved surfaces.

6.2. FUTURE PERSPECTIVES

Even though considering the latest advances in this topic (including this thesis), the field of soft plasmomechanical metamaterials is not yet mature, and therefore there is still a long way to go towards the implementation of these materials into different functional applications. Here, the upcoming perspectives regarding the specific work done in this thesis are detailed.

- The self-regulating artificial iris will be optimized to match the specific requirements needed for the implementation into functional prosthetic ophthalmological devices. In particular, the optomechanical response will be set adequate according to the specific needs by tuning the material morphology. Also, the initial curvature of the actuators due to the fabrication pre-strain will be studied and controlled to be able to achieve closed/open movement in both directions.

- Taking advantage of the magneto-mechanic properties demonstrated in this thesis, more complex designs for multifunctional actuators can be developed. In particular, different key tasks in soft robotics need to be tested, such as crawling or propulsion, among others. Furthermore, the responsivity of the material to other stimuli (such as organic solvents) will be studied in order to incorporate extra functionalities and applications.

- In this line, fully automated untethered soft robotic systems will be developed by implementing the mechanochromic self-detection as input signal into the control system of light or magnetic sources (such as lasers or electromagnets), thereby creating a closed feedback loop of sensing and actuation.

- The application of nanostructured-Fe/PDMS actuators to new energy harvesting systems will be considered: the movement arising from the broadband absorption of natural light sources (e.g. sunlight, thermal IR) could be converted into electric current by the addition of piezoelectric materials at the actuator, thereby generating renewable energy. In this line, the light-triggered electrical switch demonstrated in this work sets a foundation for the development of energy saving systems.

- The implementation of the Au-semi-shells/PDMS metamaterial into functional devices, such as strain sensing in buildings, vehicles or textiles will be studied. Also, its application as mechanically tunable light filters for smart windows and reversible optics will be considered.

- Finally, there is still room for more basic experimental work regarding the combination of metal nanostructures and soft polymers. Other metals, different dimensions and

geometries, together with polymers with different mechanical properties can open the path to new possibilities and applications.

APPENDIX A: Experimental Techniques

1. FABRICATION

1.1. Polymer substrates

This thesis is based on the use of soft polymers, specially focusing on PDMS. The selection of PDMS is motivated by its reduced Young's Modulus, high elasticity and low cost. *Sylgard 184* was selected due to its commercial availability and to be widely reported the literature.

Preparation

PDMS preparation consists on mixing the base polymer with the curing agent, which contains the polymer chains together with a platinum-based catalyst that promotes the crosslinking reaction between both components. If not specified, the mixing ratio is 10:1. However, variation of the ratios can alter its physicochemical properties, such as its viscosity and Young's modulus. The resultant mixture is degassed in a vacuum chamber until no observable bubbles are left in the mixture and then poured on the desired substrate.

Substrates

The substrates that are used in this work for curing the PDMS vary depending on the application. In chapter 3, the PDMS thin films are fabricated on a 5 mm thick PDMS substrate (that is fabricated using a standard 10 mm diameter Petri dish as a mould). In chapter 4, the periodically-corrugated PDMS films are produced by spin-coating on a PDMS replica of the photonic grating master mould, thereby achieving the exact replication of its surface corrugation. In both chapters, the PDMS substrates were previously coated by a silane compound *(Tridecafluoro-1,1,2,2-tetrahydrooctyl)trichlorosilane (97%, ABCR)* to create a monolayer that avoids permanent bonding between the polymers and therefore easies the release of the PDMS thin films. The silanization was performed by applying an oxygen plasma (100W, 1 minute) to the substrate, followed by placing the substrate and 1 mL of silane in a vacuum chamber, pumping for 30 minutes, and leaving it in vacuum for 90 minutes. In chapter 5, the PDMS is poured on the (gold/gold-semi-shell)-coated silicon wafer chips.

Spin-coating

To achieve a thickness control of PDMS thin films, spin-coating was selected as a standard technique to produce polymer thin films. Following the fabrication parameters that are described in the literature, the 50 μm thin films were produced by spin-coating the PDMS mixture at 1000 rpm for 90 seconds. Thinner films can be achieved by either increasing the spin rate or the total time of spin-coating.

Curing

The cross-linking reaction of PDMS is spontaneous at room temperature. However, the curing time at room temperature is about 3 days, while it is enormously diminished by heating the mixture. In chapters 3 and 4, the PDMS thick substrates were cured in an oven at 80ºC for 1 hour, while the PDMS thin films were cured in an oven at 80ºC for at least 20 minutes. In chapter 5, the curing using an oven is done at temperatures between 60ºC and 200ºC, and the curing using photothermia is demonstrated by using a NIR laser diode with emission wavelength at 808 nm (B1-808-1500-15A, Sheaumann), achieving temperatures up to 90ºC approximately.

1.2.   Plasmonic nanostructures

This thesis exploits the versatile physical properties of metallic semi-shells. Its fabrication is inexpensive and tuneable depending on the specific needs for each application. The process consists in the following steps:

Self-assembly of polystyrene nanospheres

The metallic semi-shells are based on the use of polystyrene nanospheres (*Life Technologies*) as a mould to achieve the hemispherical shape. To fabricate this template, the polystyrene nanospheres are deposited on a silicon substrate by colloidal self-assembly which works as follows: the commercial latex nanosphere solution (*Life Technologies*) is diluted at ratio 1:1 with ethanol (*Sigma Aldrich*, 96%). In this thesis, the nanospheres diameter can range between 200 nm and 500 nm depending on the application. Then, a monolayer of spheres is formed at the air/water interface that is on an immersed silicon wafer, leading to a spontaneously organized hexagonal close-packed 2D structure. The procedure to deposit the nanospheres at the interface consists on sliding the nanospheres solution on a hydrophilic ramp, leading to a low contact angle between the water surface and the ramp, allowing the nanospheres to remain at the air/water interface. Once the monolayer is fully formed, the water is drained depositing the nanospheres layer on the silicon substrate. The resultant sample is dried at ambient air.

Reactive Ion Etching

In order to separate the close-packed arrangement of spheres isotropically, Reactive Ion Etching (*Oxford Instruments*) was used. In short, it creates a physico-chemical etching by plasma generation that is element-selective depending on the applied gas, and its power and gas flow can be tuned in order to achieve the desired etching rate. To etch the polystyrene nanospheres, an oxygen etching at power 100W, gas pressure of 80 mTorr and gas flow of 30 sccm, with an etching time of 30 seconds. Using these conditions, we are able to uniformly shrink the nanosphere size from 200 nm to 160 nm.

Metal physical vapour deposition

The last step to fabricate the metallic semi-shells is to deposit the metal layer on top of the polystyrene nanospheres template. To do so, Electron Beam Physical Vapour Deposition

(UNIVEX 450, Leybold and *ATC-Orion; AJA International)* was used. The metal films were deposited at rates between 0.10 and 0.15 nm/s. This technique creates a very directional deposition of the material of the substrate. Due to the spherical shape of the substrate, the metallic semi-shells present thickness asymmetry through the plane perpendicular to the evaporation direction.

1.3. Rapid prototyping

The structures that are presented in Chapter 3 and 4 were fabricated by rapid prototyping.

Design

A vector graphics editor (*Inkscape*) was used to design the structures that are fabricated in this thesis.

Laser writing

A laser cutter (*Epilog Mini 24, Epilog Laser*) was used to define and cut the self-suspended structures into the desired geometry and dimensions (cutting conditions: power 4%; velocity 10%). The resultant free-standing structures were then released from the substrate by using a 0.5 mm thick poly(methyl methacrylate) with double-sided pressure-sensitive adhesive as a base support.

2. CHARACTERIZATION

2.1. Morphological

The morphology of the samples was characterized in each step of the fabrication processes in order to ensure the quality and reproducibility of the procedure. Depending on the dimensions of the material, three different approaches were chosen: electron microscopy, confocal microscopy and optical microscopy.

Scanning Electron Microscopy

Morphological characterization of micro/nanostructures was performed by Scanning Electron Microscopy (*Quanta FEG650, FEI (ThermoFisher)* ; *Auriga (Zeiss))*. Experimental conditions vary depending on the dimensions and the electrical conductivity of the material and the substrate. As a guideline, samples with good electrical conductivity such as self-assembly of polystyrene nanospheres on silicon substrate, gold or iron semi-shells on silicon substrate, were performed at 10kV in high vacuum conditions. In contrast, sample with poor electrical conductivity, such as PDMS films, were performed at 1 kV in high vacuum. Alternatively, they can be also observed at 10 kV at low vacuum.

Confocal Microscopy

Confocal microscopy (*Sensofar*) was used to determine thicknesses and microscopic profiles of the samples. Measurements were taken using 10x, 20x and 50x objectives, depending on the resolution that was needed in each case. To measure the thickness of spin-coated PDMS,

the profilometric tool was used. To fully characterize the wrinkled-PDMS or the Au-semi-shells/wrinkled-PDMS, both the profilometric and 2D contour visualization were used to measure the wavelength and amplitude of the wrinkles. The same microscopy was also used in imaging mode as a conventional optical microscope for surface observation.

2.2. Spectrometry

The optical properties of the materials that are developed in this work are carefully examined due to its importance to the final optomechanical performance. The optical transmission and reflection spectra were determined from the UV to the LWIR using the following techniques:

UV-Visible-NIR spectrometry

The UV-Visible-NIR transmission spectrometry was carried out using a fibre-coupled halogen light source (HL2000, Ocean Optics), with an optical fibre (*Ø = 400 µm, NA = 0.5; M45L01, Thorlabs*) and an aspheric lens (*Thorlabs*) to collimate the light. The optical spectra were recorded by two spectrometers for the UV-visible (*Flame, Ocean Optics®*) and near-infrared (*NIRQuest, Ocean Optics*) ranges. The UV-Visible-NIR reflection spectrometry was carried out using a bifurcated optical fibre bundle (*M25L01, Thorlabs*), a silver mirror as a reference (*PF10-03-P01, Thorlabs*) and the same light source and spectrometers as for transmission. In chapter 5, the optical characterization of samples upon increasing strain was performed by clamping each side of the sample to a PMMA holder, which is attached to a micro-positioner perpendicular to the light beam.

Infrared spectrometry

The spectrometric characterization of samples at the MWIR and LWIR regions was carried out by a Fourier Transform Infrared Spectrometer (FTIR) (*Bruker Vertex80*), using a gold film as a reference for reflection and a KBr (FT-IR grade, *Sigma Aldrich*) sample substrate as a reference for transmission.

2.3. Magnetometry

The in-plane and out-of-plane hysteresis loops were carried out using a Durham Magneto Optics Ltd magneto-optic Kerr effect (MOKE) apparatus (NanoMOKE2).

2.4. Photothermia

Temperature monitoring of the samples at the photothermal characterization was carried out using a non-contact infrared thermometer (*MLX90614, Melexis*) and a computer with Labview data acquisition software. To avoid any problems related to the different thermal emissivity of different metals (such as Fe and Au), the measurements were taken at the polymer (PDMS) side, which totally blocks the thermal emission from the nanostructured metal layers. The photothermal characterization was carried out using different light sources, depending on the experiment: a white light LED (*MWWHLP1, Thorlabs*), a NIR laser diode with emission wavelength at 808 nm (*B1-808-1500-15A, Sheaumann*) and another

laser with emission at 1470 nm (*QSM-1470-3, QPhotonics*) were used. A germanium filter (*WG90530-G, Thorlabs*) was used to block the interferences at the infrared thermometer coming from the infrared light sources. The light intensity was calibrated using an optical power meter (*S310C, S401C, PM100D, Thorlabs*). An infrared thermal camera (*FLIR*) was also used for the photothermal characterization, which is analogous to the previous temperature monitoring but giving the visualization and 2D mapping of temperature in the samples.

2.5. Visual (opto/magneto)-mechanical responses

Visualization of the mechanical responses of the materials to external stimuli such as light, temperature or magnetic fields was performed using a conventional USB camera (*DinoLite*) and *DinoCapture* as an image capture software. *ImageJ* was used for image analysis. In Chapter 3 and 4, the analysis of the curvature angle was defined as the angle at the end of the cantilever.

The light sources used for actuation were the same as for the photothermal characterization. Calibration of the incident light was measured using the optical power meter (*S310C, S401C, PM100D, Thorlabs*). Calibration of the magnetic field strength of a magnet (*Superparamagnete*) was carried out using a commercial gaussmeter (*Magnet-Physik*).

In Chapter 3, the analysis of transmitted power through the artificial iris was performed by using the optical power meter (*S310C, PM100D, Thorlabs*) after the prototype. The actuation using thermal infrared light was carried out by heating a 2x2 cm PDMS square using a Single-Stage TEC Element (*TECF1S, Thorlabs*) and the same PDMS piece covered by aluminium foil. In Chapter 4, the laser pulses were modulated using a signal modulator.

The colorimetric analysis was performed with "colorevo" [https://gitlab.com/c-p/colorevo], a purpose-built software for monitoring the evolution of the average Hue in one or more pre-defined regions of interest (ROI) of the captured video. This software is written in Python and its source code is freely available under the General Public License [https://www.gnu.org/licenses/gpl.html].

Rectangular ROIs of approximately 10x40 pixels were defined near the tip of the cantilever, where the colour variation is larger. The ROI covered the whole width of the cantilever but is limited along the cantilever length to select a narrow colour band, while still consisting of enough pixels to adequately cancel out the noise contribution from the camera CCD sensor and electronics.

3. SIMULATIONS

In Chapter 3 and 5, FDTD calculations of the optical response were performed using *Lumerical*, having a mesh of 2 nm in the region containing the metal structures. The FDTD calculation volume is a cube 296 of 1 μm edge. To perform the calculations of near-field interaction in semi-shell arrays, periodical contour was applied. In Chapter 3/Figure 3-2b, a 900x900 nm^2 detector plane was placed 100 nm before/after the semi-shell structure.

APPENDIX B: Physicochemical properties of PDMS

Property	Value
Mass density	0.97 kg·m^{-3}
Young's modulus	0.5-3 MPa
Poisson ratio	0.5
Tensile strength	6.7 MPa
Specific heat	1.46 kJ kg^{-1} K^{-1}
Thermal conductivity	0.15 W m^{-1} K^{-1}
Thermal Expansion Coefficient	3.4·10^{-4} K^{-1}
Dielectric constant	2.3-2.8
Index of refraction	1.4
Electrical conductivity	4x10^{13} Ω m
Magnetic permeability	0.6x10^6 cm^3 g^{-1}
Hydrophobicity	Highly hydrophobic, contact angle 90-120°
Colour	Colourless
Viscosity (mixed)	3500 cP
Heat Cure Time at 100°C	35 min
Heat Cure Time at 150°C	10 min
Wet etching method	Tetrabutylammonium fluoride (C$_{16}$H$_{36}$FN) + n-methyl-2-pyrrolidinone (C$_5$H$_9$NO) 3:1
Plasma etching method	CF$_4$ + O$_2$
Adhesion to silicon dioxide	Excellent
Biocompatibility	Non-irritating to skin, no adverse effect on rabbits and mice, only mild inflammatory reaction when implanted

APPENDIX C: List of Publications, Patents and Industrial Contracts

The research work accomplished in this thesis resulted in three manuscripts that are or will be submitted to international peer-reviewed scientific journals:

- "Ultrabroadband light absorbing Fe/polymer flexible metamaterial for soft opto-mechanical devices". **P. Güell-Grau**, F. Pi, R. Villa, J. Nogués, M. Alvarez, B. Sepulveda. Submitted to *Nature Photonics* in 2020.

- "Untethered mechanochromic self-sensing opto-magnetic soft actuator". **P. Güell-Grau**, P. Escudero, J.F. López-Barbera, C. Pascual-Izarra, R. Villa, J. Nogués, B. Sepulveda, M. Alvarez. To be submitted.

- "Stretchable plasmonic-enhanced Fabry-Perot cavities based on self-swallowed arrays of Au nanoparticles in elastomer films". **P. Güell-Grau**, F. Pi, R. Villa, J. Nogués, B. Sepulveda, M. Alvarez. To be submitted.

Additionally, the collaborations during this Ph.D. dissertation resulted in other publications:

- "Magnetically amplified photothermal therapies and multimodal imaging with magneto-plasmonic nanodomes". Z. Li, A. Aranda-Ramos, **P. Güell-Grau**, J.L. Tajada, L. Pou-Macayo, S. Lope-Piedrafita, F. Pi, A.G. Roca, M.D. Baró, J. Sort, C. Nogués, J. Nogués, B. Sepulveda. *Appl. Mater. Today* **12**, 430-440 (2018). [Impact Factor: 8.3 ; Citations: 8]

- "Self-Assembly of Mechanoplasmonic Bacterial Cellulose–Metal Nanoparticle Composites". O. Eskilson, S.B. Lindström, B. Sepulveda, M.M. Shahjamali, **P. Güell-Grau**, P. Sivlér, M. Skog, C. Aronsson, E.M. Björk, N. Nyberg, H. Khalaf, T. Bengtsson, J. James, M.B. Ericson, E. Martinsson, R. Selegård, D. Aili. *Adv. Funct. Mater.*, **30**, 2004766 (2020). [Impact Factor: 16.8]

- "Nanomechanical imaging sensor for detection of reversible conformational changes of molecular switches". F. Escudero, F. Pujol, **P. Güell-Grau**, C. Pascual-Izarra, R. Villa, M. Alvarez. To be submitted.

Along with these publications, the research results from this thesis led to the submission of two patents (Spanish and European):

- "Material que absorbe radiación electromagnética de longitudes de onda de entre 300 nm y 18 micras y aplicaciones". B. Sepúlveda, M. Alvarez, **P. Güell**, J. Nogués, Z. Li. Spanish Patent, **P201931100**, 11/12/2019.

- "A stretchable opto-mechanical material composed by a metallic and or dielectric nanostructure array embedded into a wrinkled elastomer". M. Alvarez, R. Villa, **P. Güell**, B. Sepúlveda, J. Nogués. **EP20382913.0**, 20/10/2020.

Moreover, the work and results in this thesis led to the signing of two industrial contracts:

- An industrial R&D contract was signed with the company *ArtLens* for a value of 28.000€ to develop a device based on the Spanish patent **P201931100**.

- An industrial R&D contract was signed with the company *IENAI SPACE* for a value of 20.000€ arising from the fabrication methods optimized in this thesis.

Also, the results of this thesis have been presented in several national and international congresses:

- "Plasmonic metamaterials for opto-mechanical sensing". **P. Güell-Grau**, R. Villa, B. Sepúlveda, M. Álvarez. *3rd Scientific Meeting of BNC-b Students*, 7-8/11/2017. Poster presentation.

- "Plasmonic nanomechanical infrared sensor with colorimetric readout". **P. Güell-Grau**, P. Escudero, R. Villa, B. Sepúlveda, M. Álvarez. *MNE2018*, 24-27/09/2018. Poster presentation. <u>Best Poster Award in Physical & Chemical Applications</u>.

- "Wavelength-tunable near-infrared sensor with colorimetric readout". **P. Güell-Grau**, P. Escudero, R. Villa, B. Sepúlveda, M. Álvarez. *MicroTAS2018*, 11-15/11/2018. Poster presentation.

- "Plasmonic mechanochromic metamaterial: development of wireless photodetectors". **P. Güell-Grau**, P. Escudero, F. Pi, R. Villa, J. Nogués, B. Sepúlveda, M. Álvarez. *4th Scientific Meeting of BNC-b Students,* 6-7/07/2019. Oral presentation.